



DIPLOMARBEIT

Molekulardynamische Simulationen der druckabhängigen Viskosität von Alkanen

Ausgeführt am Institut für Angewandte Physik der Technischen Universität Wien

unter Anleitung von PrivDoz. Dr. András Vernes

sowie unter Mitwirkung von Dipl. Ing. Alexander Grafl und Dr. Nicole Dörr

durch

Ing. Thomas Kurzmann, BSc.

Hopfenleiten 382, A-3920 Groß Gerungs

Wien, 08.09.2014

(Unterschrift Verfasser)

(Unterschrift Betreuung)



TECHNISCHE
UNIVERSITÄT
WIEN
Vienna University of Technology



MASTER'S THESIS

Pressure-dependent viscosity of selected alkanes by molecular dynamics simulation

Carried out at the Institute of Applied Physics at Vienna University of Technology

under supervision by PrivDoz. Dr. András Vernes
and advisory of Dipl. Ing. Alexander Grafl and Dr. Nicole Dörr

by

Ing. Thomas Kurzmann, BSc.
Hopfenleiten 382, A-3920 Groß Gerungs

Vienna, 08.09.2014

(Signature of Author)

(Signature of Advisor)

Erklärung zur Verfassung der Arbeit

Ing. Thomas Kurzmann, BSc.
Hopfenleiten 382, A-3920 Groß Gerungs

Hiermit erkläre ich, dass ich diese Arbeit selbständig verfasst habe, dass ich die verwendeten Quellen und Hilfsmittel vollständig angegeben habe und dass ich die Stellen der Arbeit - einschließlich Tabellen, Karten und Abbildungen -, die anderen Werken oder dem Internet im Wortlaut oder dem Sinn nach entnommen sind, auf jeden Fall unter Angabe der Quelle als Entlehnung kenntlich gemacht habe.

(Ort, Datum)

(Unterschrift Verfasser)

Acknowledgments

I would like to express my gratitude to my supervisor PrivDoz. Dr. András Vernes for introducing me to correct scientific working practices as well as for useful discussions and help throughout the whole course of my master's thesis.

Besides my advisor, I would like to thank the rest of my thesis committee: Dipl.-Ing. Alexander Grafl and Dr. Nicole Dörr for valuable advice and support for my research at *AC²T research GmbH*.

Furthermore, I would like to thank *AC²T research GmbH* under the leadership of Dr. Andreas Pauschitz who provided me with the facilities for my master's thesis. Funding for this work was provided by the Austrian COMET program project K2 XTribology, No. 824187.

Also, I would like to thank Dr. Stefan Eder for introducing me to the company's computing infrastructure as well as for helping me with basics questions about the *LAMMPS* molecular dynamics simulator.

Last but not least, I want to thank my family and close friends for their unconditional support throughout my degree.

Abstract

The Green-Kubo method for calculating viscosities at zero-shear rate of liquid alkanes by means of molecular dynamics (MD) has been applied. Within this thesis, the common study of simulating viscosities close to ambient pressure has been extended to pressures relevant for studies of elasto-hydrodynamic lubrication (0.1 to 1000 MPa). Furthermore, attempts have been made to elucidate the influence of the chemical structure on the high-pressure rheology of *n*-octane, 2,2,4-trimethylpentane, *n*-hexadecane and (6S)-2,2,4,4,6,8,8-heptamethylnonane.

The molecular dynamics simulations for this work were carried out using a modified version of the all-atom optimized potentials for liquid simulations (OPLS-aa) force field, a particle-particle mesh (PPPM) long-range electrostatic solver, a reversible reference system propagator algorithm (rRESPA) for time integration and a Nosé-Hoover chain thermostat.

The equilibration of investigated MD systems has been traced by using the Hellinger metric for the time-dependent density distribution function for the one third of the sum of the off-diagonal pressure tensor components.

In order to elucidate the influence of the chemical structure, rotational relaxation times were calculated by autocorrelating normalized intramolecular positions and fitting them to an exponentially decaying model. In addition, the partial contributions to the overall pressure tensor used for calculating the viscosity were examined separately to provide further information about the structural influence.

It was found that MD results obtained for normal alkanes are in good agreement with experimental measurements, while viscosities of branched alkanes are systematically overestimated. Furthermore, the pressure dependence of the calculated zero-shear viscosities is well described by Roelands' pressure viscosity relation. Analysis of different contributions to the pressure tensor showed that in contrast to the normal alkanes, the pressure tensor contribution due to bonds dominates over the angle contributions in branched alkanes. Finally, it was also found that when the Green-Kubo method is applied to systems with long relaxation times, significant computational efforts are necessary to obtain statistically reliable results.

Contents

Acknowledgments	iii
Abstract	v
Contents	vii
List of Figures	ix
List of Tables	xi
1 Introduction	1
2 Basic Framework	3
2.1 Green-Kubo Formalism	3
2.2 Molecular Dynamics (MD)	6
2.3 MD Simulation of Zero-shear Viscosity	8
2.4 Pressure Dependence of Viscosity	8
3 Computational Details	11
3.1 Selection of Molecules, State Points and System Size	11
3.2 Force Field, Long-range Corrections and Cutoff Distances	13
3.3 Time Integration	15
3.4 Thermostatting	17
4 Results and Discussion	21
4.1 Detection of Equilibrium	21
4.2 Zero-shear and Bulk Viscosities	27
4.3 Rotational Correlation Time	39
5 Summary and Conclusion	45
6 Outlook	47
Appendix A LAMMPS Script	49
Appendix B Hellinger Metric and Departure from Equilibrium	53
Appendix C Convergence of Zero-shear and Bulk Viscosities	63
Bibliography	89

List of Figures

3.1	Structures of the simulated molecules	12
3.2	Effect of constrained H-bond length on the C-C-C-C dihedral energy	14
3.3	All-atom radial distribution functions at 100 kPa	15
3.4	All-atom radial distribution functions at 1 GPa	16
3.5	Illustration of the distance stepped rRESPA algorithm	17
3.6	Effect of undercoupling a Nosé-Hoover thermostat	18
4.1	<i>n</i> -Hexadecane equilibration box snapshots	23
4.2	Illustration for the time-parameters t_{eq} , t_{run} and the block index m	24
4.3	The influence of t_{eq} on the Hellinger metric	25
4.4	Pressure dependence of shear and bulk viscosity	29
4.5	Large-block limit for <i>n</i> -octane at 100 kPa	32
4.6	Contributions to zero-shear viscosity in case of <i>i</i> -octane	33
4.7	Comparison of viscosities with experimental data	35
4.8	Calculated pressure-viscosity relations	36
4.9	Viscosities from different pressure tensor contributions	37
4.10	Vectors to calculate the rotational correlation time	39
4.11	Rotational correlation times for all systems as a function of pressure (A)	41
4.12	Rotational correlation times for all systems as a function of pressure (B)	42
4.13	Viscosity versus rotational correlation time	43
4.14	Rotational autocorrelation functions of <i>n</i> -hexadecane at 100 kPa	43
4.15	3D renderings of simulated molecules	44
B.1	Hellinger metric of all systems at 100 kPa	53
B.2	Hellinger metric of all systems at 250 MPa	54
B.3	Hellinger metric of all systems at 500 MPa	55
B.4	Hellinger metric of all systems at 750 MPa	56
B.5	Hellinger metric of all systems at 1 GPa	57
B.6	Convergence of $\langle p^{off} \rangle$ for all systems at 100 kPa	58
B.7	Convergence of $\langle p^{off} \rangle$ for all systems at 250 MPa	59
B.8	Convergence of $\langle p^{off} \rangle$ for all systems at 500 MPa	60
B.9	Convergence of $\langle p^{off} \rangle$ for all systems at 750 MPa	61
B.10	Convergence of $\langle p^{off} \rangle$ for all systems at 1 GPa	62
C.1	Zero-shear viscosity of <i>n</i> -octane at 250 MPa	64
C.2	Zero-shear viscosity of <i>n</i> -octane at 500 MPa	65
C.3	Zero-shear viscosity of <i>n</i> -octane at 750 MPa	66
C.4	Zero-shear viscosity of <i>n</i> -octane at 1 GPa	67
C.5	Zero-shear viscosity of <i>i</i> -octane at 100 kPa	68

C.6	Zero-shear viscosity of <i>i</i> -octane at 250 MPa	69
C.7	Zero-shear viscosity of <i>i</i> -octane at 500 MPa	70
C.8	Zero-shear viscosity of <i>i</i> -octane at 750 MPa	71
C.9	Zero-shear viscosity of <i>i</i> -octane at 1 GPa	72
C.10	Zero-shear viscosity of <i>n</i> -hexadecane at 100 kPa	73
C.11	Zero-shear viscosity of <i>n</i> -hexadecane at 250 MPa	74
C.12	Zero-shear viscosity of <i>n</i> -hexadecane at 500 MPa	75
C.13	Zero-shear viscosity of <i>n</i> -hexadecane at 750 MPa	76
C.14	Zero-shear viscosity of <i>n</i> -hexadecane at 1 GPa	77
C.15	Zero-shear viscosity of <i>i</i> -hexadecane at 100 kPa	78
C.16	Zero-shear viscosity of <i>i</i> -hexadecane at 250 MPa	79
C.17	Zero-shear viscosity of <i>i</i> -hexadecane at 500 MPa	80
C.18	Zero-shear viscosity of <i>i</i> -hexadecane at 750 MPa	81
C.19	Zero-shear viscosity of <i>i</i> -hexadecane at 1 GPa	82
C.20	Bulk viscosity at 100 kPa	83
C.21	Bulk viscosity at 250 MPa	84
C.22	Bulk viscosity at 500 MPa	85
C.23	Bulk viscosity at 750 MPa	86
C.24	Bulk viscosity at 1 GPa	87

List of Tables

3.1	Computational efficiency of various time integration algorithms	16
3.2	The thermostat coupling parameter and the rotational correlation time	18
4.1	Parameters used for equilibrium detection.	25
4.2	Detected equilibria	26
4.3	Computational parameters.	27
4.4	Calculated pressure-dependent zero-shear viscosities	30
4.5	Calculated pressure-dependent zero-shear viscosities (continued)	31
4.6	Comparison with experimental data	34
4.7	Calculated rotational correlation times	40

Introduction

The aim of this work is to use equilibrium molecular dynamics coupled with the Green-Kubo relations for the simulation of the pressure dependence of viscosity at zero-shear rate for *n*-octane, *i*-octane, *n*-hexadecane and *i*-hexadecane, respectively. This work should provide a basis for future investigations regarding the influence of the specific chemical structure on high-pressure rheological properties of liquids.

High-pressure rheology is of great interest for the correct description of dynamical processes where fluids are exposed to high hydrostatic pressure (typically in excess of 100 MPa). An example for an important technological field, where the pressure in fluids extends to the GPa range, is the elastohydrodynamic lubrication. This field focuses on the description of lubricated, highly loaded tribological contacts (lubricated surfaces, with a normal force applied, in a sliding motion with respect to each other). The insights gained in this field can ultimately be utilized to optimize friction in a broad range of devices including car transmissions, heavy industrial machinery and so on. Benefits resulting from optimizations of tribological systems can reduce energy consumption of machinery due to lower frictional losses as well as increased product lifetime and reliability.

In order to accurately model and predict properties like the coefficient of friction in such systems, detailed knowledge about the rheology of fluids at extreme conditions encountered within tribo-contacts is required [1]. However, the experimentally challenging nature of high-pressure measurements make it difficult and expensive to obtain all the required properties of lubricants under controlled laboratory conditions. In order to circumvent these difficulties and to be subject to fewer technical restriction in the accessible parameter space (chemistry of the lubricant, pressure p , temperature T , shear rate $\dot{\gamma}$ and others), computer simulations can be employed. For instance, one important class of modern synthetic lubricants, namely polyalphaolefines, typically consists of mixtures of branched alkanes with an ambient pressure viscosity specifically tailored to their application, see Ref. [2]. Since the number of possible isomers of branched alkanes increases strongly with the chain length, e.g., alkanes containing only 16 carbon atoms can be arranged in more than 10000 theoretically possible structures, it would be of great interest to predict the high-pressure rheology simply on the basis of the molecular structure. If this could be achieved, lubricant formulations could be optimized towards providing high-pressure properties needed for a specific application.

This work provides a basis for investigations that focus on understanding the relationship between the chemical nature of a molecule and its calculated high-pressure rheological properties such as its viscosity at zero-shear rate and at constant temperature or its bulk viscosity. The employed method of equilibrium molecular dynamics coupled with the Green-Kubo formalism,

derived from the linear response theory, inherently allows for a precise numerical control of the simulations for a large range of the relevant characteristic quantities, such as pressure, temperature and chemical structure. Furthermore, it offers the advantage of being able to study liquids at an atomic level and hence has the potential to provide information about the role of every single atom in a molecule when examining the (atomic and molecular) mechanisms leading to the macroscopic viscosity, for example.

Basic Framework

2.1 Green-Kubo Formalism

The following, partially heuristic, derivation of the Green-Kubo relations is based on Refs. [3–5]. The Green-Kubo relations for transport coefficients (e.g., shear and bulk viscosity) are derived from the linear response theory. This theory is founded on the assumption that the Hamiltonian of the system \mathcal{H}' can be written as

$$\mathcal{H}' = \mathcal{H}(\mathbf{p}, \mathbf{q}) - \underbrace{A(\mathbf{p}, \mathbf{q})X(t)}_{\mathcal{H}_{ext}(t)} \quad , \quad (2.1)$$

where $\mathcal{H}_{ext}(t)$ is a time-dependent perturbation distorting the equilibrium of the system described by $\mathcal{H}(\mathbf{p}, \mathbf{q})$. This $\mathcal{H}_{ext}(t)$ is assumed to be proportional to the quantity $A(\mathbf{p}, \mathbf{q})$, i.e., the displacement related to the force $X(t)$ that induces a time dependent change $\delta\bar{B}(\mathbf{p}, \mathbf{q}, t)$ of the physical quantity $B(\mathbf{p}, \mathbf{q})$. Knowing that the effect of the external perturbation on the distribution function $f(\mathbf{p}, \mathbf{q}, t)$ of the system is given by the Liouville equation,

$$\frac{\partial f(\mathbf{p}, \mathbf{q}, t)}{\partial t} = (\mathcal{H}, f(\mathbf{p}, \mathbf{q}, t)) + (\mathcal{H}_{ext}, f(\mathbf{p}, \mathbf{q}, t)) \quad , \quad (2.2)$$

where (a, b) denotes the Poisson bracket,

$$(a, b) = \sum_{(\mathbf{p}, \mathbf{q})} \left(\frac{\partial a}{\partial \mathbf{q}} \frac{\partial}{\partial \mathbf{p}} - \frac{\partial a}{\partial \mathbf{p}} \frac{\partial}{\partial \mathbf{q}} \right) b \quad . \quad (2.3)$$

Eq. (2.2) yields the formal solution

$$f(t) = e^{(t-t_0)(\mathcal{H}, \cdot)} f(t_0) + \int_{t_0}^t dt' e^{(t-t')(\mathcal{H}, \cdot)} (\mathcal{H}_{ext}(t'), f(t')) \quad , \quad (2.4)$$

where for sake of simplicity, the variables (\mathbf{p}, \mathbf{q}) are omitted and the exponential function of the Poisson bracket is expressed by means of the Taylor series expansion

$$e^{\lambda(\mathcal{H}, \cdot)} = \sum_{n=0}^{\infty} \frac{\lambda^n}{n!} (\mathcal{H}, \cdot)^n \quad . \quad (2.5)$$

It can be shown, that Eq. (2.4) is a formal solution of Eq. (2.2) by differentiating both sides with respect to time t . By substituting equation (2.4) into itself and taking the linear approximation

as well as assuming a canonical ensemble, such that the system was in equilibrium at the infinite past, $f(t_0 \rightarrow -\infty) = f_{eq}$, one obtains,

$$f(t) = f_{eq} + \int_{-\infty}^t dt' e^{(t-t')(\mathcal{H}, \cdot)} (\mathcal{H}_{ext}(t'), f_{eq}) \quad , \quad (2.6)$$

with

$$f_{eq} = e^{-\beta\mathcal{H}} \left[\iint d\mathbf{p}d\mathbf{q} e^{-\beta\mathcal{H}} \right]^{-1}, \quad \beta = \frac{1}{k_B T} \quad , \quad (2.7)$$

where k_B is Boltzmann's constant and T the temperature. With the definition of the phase space expectation value of a physical quantity a ,

$$\langle a \rangle := \iint d\mathbf{p}d\mathbf{q} a(\mathbf{p}, \mathbf{q}) f(\mathbf{p}, \mathbf{q}) \quad (2.8)$$

the time dependent fluctuations $\delta\bar{B}(t)$ of the quantity B are given by

$$\begin{aligned} \delta\bar{B}(t) &= \langle B(t) \rangle - \langle B \rangle \\ &= \iint d\mathbf{p}d\mathbf{q} f(t)B - \iint d\mathbf{p}d\mathbf{q} f_{eq} B \quad . \end{aligned} \quad (2.9)$$

Introducing Eq. (2.6) into Eq. (2.9) and using the definition of \mathcal{H}_{ext} from Eq (2.1) as well as $\Delta A = A - \langle A \rangle$ and $\Delta B = B - \langle B \rangle$, results

$$\begin{aligned} \delta\bar{B}(t) &= \iint d\mathbf{p}d\mathbf{q} \int_{-\infty}^t dt' e^{(t-t')(\mathcal{H}, \cdot)} (\mathcal{H}_{ext}, f_{eq}) B \\ &= \int_{-\infty}^t dt' \iint d\mathbf{p}d\mathbf{q} e^{(t-t')(\mathcal{H}, \cdot)} (f_{eq}, \Delta A) \Delta B X(t') \quad . \end{aligned} \quad (2.10)$$

Based on the properties of the exponential function and f_{eq} , after partial integration, Eq. (2.10) can be written as

$$\begin{aligned} \delta\bar{B}(t) &= \int_{-\infty}^t dt' \iint d\mathbf{p}d\mathbf{q} (f_{eq}, \Delta A) e^{-(t-t')(\mathcal{H}, \cdot)} \Delta B X(t') \\ &= \int_{-\infty}^t dt' \underbrace{\iint d\mathbf{p}d\mathbf{q} f_{eq}(\Delta A, \Delta B(\mathbf{p}_{t'}, \mathbf{q}_{t'}))}_{\Phi_{BA}(t')} X(t') \quad , \end{aligned} \quad (2.11)$$

according to Ref. [5] with

$$e^{-(t-t')(\mathcal{H}, \cdot)} \Delta B(\mathbf{p}, \mathbf{q}) = \Delta B(\mathbf{p}_{t'}, \mathbf{q}_{t'}) \quad . \quad (2.12)$$

When assuming the force $X(t) = e^{i\omega t}$ to be periodic in time, the response to such a periodic perturbation can also be considered to be periodic. One can thus introduce a frequency dependent, complex admittance in the form of

$$\chi_{BA}(\omega) = \int_0^\infty \Phi_{BA}(t) e^{i\omega t} dt \quad . \quad (2.13)$$

Here, the so-called response function $\Phi_{BA}(t)$ is according to Eq. (2.11), given by

$$\Phi_{BA}(t) = \langle\langle \Delta A, \Delta B(t) \rangle\rangle = \beta \langle \Delta \dot{A}; \Delta B(t) \rangle \quad , \quad (2.14)$$

where $\langle a; b \rangle$ denotes the canonical correlation which in classical mechanics is simply the product of two factors at a time lag τ and is independent of the time origin t , namely

$$\begin{aligned} \langle a; b(\tau) \rangle &= \iint d\mathbf{p}d\mathbf{q} f_{eq} a(\mathbf{p}, \mathbf{q}, t) b(\mathbf{p}, \mathbf{q}, t + \tau) \\ &= \iint d\mathbf{p}d\mathbf{q} f_{eq} a(\mathbf{p}_t, \mathbf{q}_t) b(\mathbf{p}_{t+\tau}, \mathbf{q}_{t+\tau}) \quad . \end{aligned} \quad (2.15)$$

If now one considers B to correspond to the viscous stress σ_{xy} resulting from the strain γ_{xy} ,

$$\sigma_{xy} = \eta_{xy} \frac{d\gamma_{xy}}{dt}, \quad \langle \sigma_{xy} \rangle = 0 \quad , \quad (2.16)$$

the zero-shear $\dot{\gamma} = 0$ viscosity η in the xy plane is immediately given by Eqs. (2.13) and (2.14) as in Ref. [6]

$$\eta_{xy} = \lim_{\omega \rightarrow 0} \frac{\beta}{V} \int dt e^{i\omega t} \iint d\mathbf{p}d\mathbf{q} f_{eq} \sigma_{xy}(0) \sigma_{xy}(t) \quad . \quad (2.17)$$

Furthermore, by applying the same formalism to the full stress tensor, the relation for bulk viscosity η^B can be obtained,

$$\begin{aligned} \eta^B &= \lim_{\omega \rightarrow 0} \frac{\beta}{V} \int dt e^{i\omega t} \frac{1}{9} \sum_{\mu, \nu} \iint d\mathbf{p}d\mathbf{q} f_{eq} \sigma'_{\mu\mu}(0) \sigma'_{\nu\nu}(t) \quad , \\ \sigma'_{\mu\mu}(t) &= \sigma_{\mu\mu}(t) - \left(\bar{p} + \frac{\partial \bar{p}}{\partial E} (E - \langle E \rangle) \right) \quad , \end{aligned} \quad (2.18)$$

where the summation over μ and ν runs over the Cartesian coordinates x, y and z . Additionally, using the ergodic hypothesis

$$\langle a \rangle = \langle a \rangle_T := \lim_{T \rightarrow \infty} \frac{1}{T} \int_0^T a(t) dt \quad , \quad (2.19)$$

the integration over the phase space in Eqs. (2.17) and (2.18) can be replaced by a time integration. The trajectories calculated by molecular dynamics in the canonical ensemble can then be directly used to calculate the transport coefficients [7]. Indeed, by applying Eq. (2.19) to Eq. (2.17) or Eq. (2.18) expressions for the zero-shear and bulk viscosity are obtained which can easily be discretized and hence approximated by using MD,

$$\begin{aligned} \eta &= \lim_{\tau_{run} \rightarrow \infty} \lim_{\tau_c \rightarrow \infty} \frac{\beta}{V \tau_{run}} \frac{1}{6} \sum_{\mu \neq \nu} \int_0^{\tau_{run}} dt \int_0^{\tau_c} dt' \sigma_{\mu\nu}(t) \sigma_{\mu\nu}(t+t') \quad , \\ \eta^B &= \lim_{\tau_{run} \rightarrow \infty} \lim_{\tau_c \rightarrow \infty} \frac{\beta}{V \tau_{run}} \frac{1}{9} \sum_{\mu, \nu} \int_0^{\tau_{run}} dt \frac{1}{9} \int_0^{\tau_c} dt' \sigma'_{\mu\mu}(t) \sigma'_{\nu\nu}(t+t') \quad , \end{aligned} \quad (2.20)$$

where τ_{run} represents the total length of the simulated time and τ_c is the correlation time such that $\tau_{run} \gg \tau_c$.

2.2 Molecular Dynamics (MD)

In classical Hamiltonian mechanics, the time evolution of a mechanical system, described by the canonical coordinates (\mathbf{p}, \mathbf{q}) , is given by the Hamilton equations of motion

$$\begin{cases} \frac{d\mathbf{p}}{dt} = -\frac{\partial\mathcal{H}}{\partial\mathbf{q}} \\ \frac{d\mathbf{q}}{dt} = +\frac{\partial\mathcal{H}}{\partial\mathbf{p}} \end{cases}, \quad (2.21)$$

with

$$\mathcal{H}(\mathbf{p}, \mathbf{q}) = \sum_{i=1}^N \frac{p_i^2}{2m_i} + V(\mathbf{q}) \quad , \quad (2.22)$$

and

$$\begin{aligned} V(\mathbf{q}) = & \sum_{i=1}^N \left\{ \frac{1}{2} \sum_j^{bond} K_{ij}^{bond} (q_i - q_j)^2 + \frac{1}{3} \sum_j^{angle} K_j^{angle} (\phi_j - \phi_{0,j})^2 \right. \\ & + \frac{1}{8} \sum_j^{dih} \sum_{n=1}^4 K_{j,n}^{dih} [1 + \cos(n\theta_j)] + \sum_j^{vdW} 4\epsilon_j \left[\left(\frac{\sigma_j}{|q_i - q_j|} \right)^{12} - \left(\frac{\sigma_j}{|q_i - q_j|} \right)^6 \right] \\ & \left. + \sum_j^{coul} \frac{c_i c_j}{4\pi\epsilon_0 |q_i - q_j|} + E_i^{long} \right\} + E^{tail} \quad , \quad (2.23) \end{aligned}$$

where the summation over i runs over all N atoms in the system, the summations over j run over all bond, angle, dihedral, van der Waals (vdW) and Coulomb (coul) interactions that atom i is a part of. The summations over j is carried out in a way, that force cutoff distances and molecular structure are taken into account. E_i^{long} is the contribution of the long range solver for the electrostatic interactions and E^{tail} is a correction for the vdW cutoff. The constants K_{ij}^{bond} , K_j^{angle} , $\phi_{0,j}$, $K_{j,n}^{dih}$, ϵ_j , σ_j and the charges c_i are parameters of the force field chosen.

Since the potential energy function $V(\mathbf{q})$ is not explicitly time dependent, Eq. (2.22) describes a system where the total energy is conserved. If no atoms are lost or added and the volume of the system is kept constant during the simulation, the simulated ensemble corresponds to the microcanonical (NVE) ensemble. Eq. (2.23) is a representation of the potential energy as it is implemented in *Large-scale Atomic/Molecular Massively Parallel Simulator (LAMMPS)*, provided by Sandia National Laboratories^a [8], for simulations with the *Optimized Potential for Liquids Simulations (OPLS)* force field using harmonic bond and angle potentials (refer to page 11 for details on force field).

However, if simulations at constant temperature are to be carried out, the sum of potential and kinetic energy must be allowed to fluctuate. Nosé, Hoover and Martyna et al. [9, 10] came up with a modified Hamilton function

$$\mathcal{H}'(\mathbf{p}, \mathbf{q}, \boldsymbol{\eta}, \mathbf{p}_\eta) = \sum_{i=1}^N \frac{p_i^2}{2m_i} + V(\mathbf{q}) + \sum_{i=1}^M \frac{p_{\eta_i}^2}{2Q_i} + NkT\eta_1 + \sum_{i=2}^M kT\eta_i \quad , \quad (2.24)$$

^alammps.sandia.gov/index.html

that reproduces the canonical (NVT) ensemble. In Eq. (2.24) the thermostat coordinates $(\boldsymbol{\eta}, \mathbf{p}_\eta)$ of a total of M virtual thermostat “particles” with the formal masses of Q_i are introduced. This enables the simulated system to exchange energy with the coupled, fictitious heat reservoir in order to kept the average temperature in the target system constant. The equations of motion for this thermostated system

$$\left\{ \begin{array}{l} \dot{q}_i = \frac{p_i}{m_i} \quad , \\ \dot{p}_i = -\frac{\partial V(\mathbf{q})}{\partial q_i} - p_i \frac{p_{\eta_1}}{Q_1} \quad , \\ \dot{\eta}_i = \frac{p_{\eta_i}}{Q_i} \quad , \\ \dot{p}_{\eta_1} = \left[\sum_{i=1}^N \frac{p_i^2}{m_i} - NkT \right] - p_{\eta_1} \frac{p_{\eta_2}}{Q_2} \quad , \\ \dot{p}_{\eta_j} = \left[\frac{p_{\eta_{j-1}}^2}{Q_{j-1}} - kT \right] - p_{\eta_j} \frac{p_{\eta_{j+1}}}{Q_{j+1}} \quad , \\ \dot{p}_{\eta_M} = \left[\frac{p_{\eta_{M-1}}^2}{Q_{M-1}} - kT \right] \quad , \end{array} \right. \quad (2.25)$$

now including both, atomic (p_i, q_i) , $i = 1 \dots N$ and thermostat degrees of freedom (p_{η_j}, η_j) , $j = 1 \dots M$ [10].

In order to time integrate the equations of motion, the *reversible reference system propagator algorithm* (rRESPA), formulated by Tuckerman et al., was used for this work. Details about its derivation as well as an example for its implementation can be can be found in Ref. [11].

Pressure tensor

The elements of the pressure tensor

$$\sigma_{\mu\nu} = \frac{1}{V} \sum_{i=1}^N \left(\underbrace{m_i v_{i\mu} v_{i\nu}}_{kin.} + \underbrace{r_{i\mu} F_{i\nu}}_{virial} \right) \quad \mu, \nu = x, y, z \quad , \quad (2.26)$$

used within this work are computed as given by *LAMMPS*. In Eq. (2.26) V is the volume of the MD system, the sum over i runs over all N atoms, m_i is the mass of atom i , the indices μ and ν run over the x, y and z components of the vectors in a right-handed Cartesian coordinate system and $\mathbf{v}_i, \mathbf{r}_i$ and \mathbf{F}_i represent the velocity and position of atom i and force vector on this Atom. The force vector \mathbf{F}_i is a superposition of all forces acting on atom i , namely

$$\mathbf{F}_i = \mathbf{f}_i^{bond} + \mathbf{f}_i^{angle} + \mathbf{f}_i^{dih} + \underbrace{\mathbf{f}_i^{vdW} + \mathbf{f}_i^{Coul} + \mathbf{f}_i^{kspace}}_{\mathbf{f}_i^{long}} \quad , \quad (2.27)$$

according to the selected force field where \mathbf{f}_i^{bond} , \mathbf{f}_i^{angle} , \mathbf{f}_i^{dih} , \mathbf{f}_i^{vdW} , \mathbf{f}_i^{Coul} and \mathbf{f}_i^{kspace} are the resulting forces from bond, angle, dihedral, pairwise van der Waals and Coulomb interactions as well as the contributions resulting from the long range electrostatic solver operating in k-space. For further reference, the contributions from \mathbf{f}_i^{vdW} , \mathbf{f}_i^{Coul} and \mathbf{f}_i^{kspace} will be summed to yield \mathbf{f}_i^{long} which will be referred to as the long range forces on atom i .

2.3 MD Simulation of Zero-shear Viscosity

In general, the existing MD methods to determine the viscosity of fluids can be divided into two main approaches,

- Equilibrium Molecular Dynamics (EMD) and
- Non-Equilibrium Molecular Dynamics (NEMD) simulations.

The EMD method implies that, in contrast to the NEMD method, no shear force is applied to the system, hence the average shear rate of the liquid is zero. This needs to be kept in mind when the results of MD simulations are compared amongst each other and to experimental values. The NEMD method however, allows for studying the shear rate dependency of the viscosity (although at comparatively high shear rates, which only recently became accessible in experiments, see Ref. [12]). Several publications exist that compare both methods to show that the results from NEMD methods, extrapolated to zero-shear rate, correspond to the results obtained by EMD e.g. Refs. [13–16]. The general consensus found in these publications is, that both methods are similarly efficient to calculate the shear viscosity at zero-shear rate, while the NEMD methods provide the advantage of obtaining additional information on the rheology of liquids at high shear rates. The EMD approach, however, inherently does not rely on the need to extrapolate the viscosity to zero-shear rate.

The comprehensive paper published by Jones and Mandadapu, see Ref. [17], provides important details on the calculation of transport coefficients by the Green-Kubo method and includes algorithms to estimate the errors involved in the viscosity calculation. Many of the algorithms proposed in this paper were adopted for this thesis.

Only one publication was found that deals explicitly with the pressure dependence of viscosity being calculated by MD. McCabe et al., see Ref. [18], simulated the rheological properties of 9-octylheptadecane at pressures up to 1 GPa and shear rates in the range of $10^7 - 10^{11} \text{ s}^{-1}$. Their MD setup did not include explicit hydrogen atoms bonded to the carbon atoms of the alkane but instead, a united-atom model was used which approximates CH_3 and CH_2 groups with simple spheres. They found, that while the viscosity is underpredicted when compared to the experimental values, the relative increase with pressure agrees well with the measurements. Furthermore, they showed that as the shear rate increases beyond the inverse of the rotational correlation time of the molecules, shear thinning is observed. In addition to their results, a comprehensive list of publications in the field of MD simulations of tribologically relevant liquids is provided. These papers however, focus on the strain rate dependence of viscosity and use, in contrast to this thesis, united-atom models for simulations.

Cui et al. [13] carried out EMD simulations of *n*-hexadecane and applied the Green-Kubo formalism to calculate the zero-shear viscosity of the liquid. In addition to the simulation results of *n*-hexadecane, which is also simulated in this work, their publication provides valuable information concerning the choice of the maximum significant correlation time.

Dysthe et al. [19] provide information on the influence of the selection of timestep size, potential cutoff distance and holonomic constraints on the calculated viscosity. Furthermore, they calculate several different relaxation times and conformational properties as well as propose methods to estimate the error in the calculated viscosities.

2.4 Pressure Dependence of Viscosity

The investigations on the effect of static pressure on the shear viscosity of fluids date back for more than a century. Among the first scientists carrying out viscosity measurements at pressures

significantly greater than atmospheric was Barus in the 1890s [20]. His research concentrated on the viscosity of “marine glue” in a pressure range of 0 to 200 MPa and temperatures from 8.5 to 30.5 °C. Based on his observations, he originally proposed a linear relationship between pressure p and shear viscosity $\eta(p, \dot{\gamma} \rightarrow 0) = \eta_0(p)$ where $\dot{\gamma}$ denotes the shear rate.

$$\eta(p) = \eta(p_0) [1 + \alpha(p - p_0)] \quad , \quad (2.28)$$

with p_0 set to 1 atm and α being a fitting parameter. For simplicity, the subscript 0 in $\eta_0(p)$ will be omitted since the shear rate dependency of viscosity is not part of this work. Thus, unless otherwise noted, $\eta(p)$ refers to the low shear rate limit $\eta(p, \dot{\gamma} \rightarrow 0)$ within this thesis. Considering the increasing errors of his measurements at high pressures due to slip, he stated, that an exponential pressure-viscosity relation (2.29),

$$\ln \eta(p) = a' + b'(p - p_0) \quad , \quad (2.29)$$

with a' and b' representing fitting parameters, might be applicable. Nowadays, an equivalent equation is used as a first approximation to the dependence of viscosity at zero-shear rate on pressure:

$$\eta(p) = \eta(p_0)e^{\alpha(p-p_0)} \quad , \quad (2.30)$$

where α is commonly referred to as “pressure-viscosity coefficient”. It is easily seen, that Eq. (2.28) is the linear part of the of a Taylor series expansion of Eq. (2.30). However, it is important to note that the definition of α in equation (2.30) varies in literature. Bair et al. [21] listed a few common definitions:

$$\alpha(p) = \frac{1}{\eta} \frac{d\eta}{dp} \quad , \quad (2.31)$$

$$\alpha_0 = \left[\frac{d \ln(\eta)}{dp} \right]_{p=0} \quad , \quad (2.32)$$

$$\alpha_B(p) = \frac{\ln(\eta(p)/\eta(p=0))}{p} \quad , \quad (2.33)$$

$$\alpha = \left[\int_0^\infty \frac{\eta(p=0)dp}{\eta(p)} \right]^{-1} \quad . \quad (2.34)$$

As the measurement techniques and the theoretical understanding of liquids advanced and the accessible pressure range increased in the middle of the 20th century, it was shown that the viscosity of liquids generally increases in a more complicated manner than suggested by Eq. (2.30) proposed by Barus in 1893 [22, 23]. In 1966, Roelands provided a comprehensive review of the field in his doctoral thesis [24]. In the following a brief summary of the empirical pressure-viscosity relations referenced by Roelands is given, namely

$$\left\{ \begin{array}{l} \ln \frac{\eta(p)}{\eta(p=0)} = \frac{K}{p^{-1} + c} \quad , \\ \ln \frac{\eta(p)}{\eta(p=0)} = K' p^{c'} \quad , \\ \ln \frac{\eta(p)}{\eta_{p=0}} = K'' \log \left(1 + \frac{p}{c''} \right) \quad , \end{array} \right. \quad (2.35)$$

where K , K' , K'' , c , c' and c'' represent parameters that are characteristic for a given liquid. He further states, that these equations are applicable within a pressure range of up to at least 300 to 500 MPa with one set of parameters. Additionally to the aforementioned relations, which were already documented in literature before 1966, Roelands proposed an empirical pressure-viscosity relation:

$$\log_{10} [\eta(p)] + 1.200 = [\log_{10} (\eta_{p=0}) + 1.200] \left(1 + \frac{p}{2.000}\right)^z, \quad (2.36)$$

where η denotes the dynamic viscosity in cP at pressure p given in kgf/cm². Roelands claimed that this relation describes $\eta(p)$ over a “very wide ranges of temperature and pressure” - with only a single parameter z , the so called pressure-viscosity-index in addition to the viscosity of the liquid at ambient pressure $\eta(p = 0)$). The parameter z was said to be characteristic for a given liquid as well as independent of pressure and only weakly dependent on temperature. In newer literature, Eq. (2.36) is given in a slightly different form [25]:

$$\eta(p) = \eta(p = 0) \exp \left\{ \left[\log_{10} (\eta(p = 0)) + 9.67 \right] \left[-1 + \left(1 + \frac{p}{p_0}\right)^z \right] \right\}, \quad (2.37)$$

which is equivalent to Eq. (2.36), except for the constant 9.67 and $p_0 = 1.96 \times 10^8$ Pa. The choices of the constants in Eqs. (2.36) and (2.37) are purely empirical. Note that it was recently shown, that Roelands ignored some experimental evidence within his thesis [26].

Nevertheless, Roelands provided a link between his empirical relation and statistical mechanics. By starting from the Cohen-Turnbull free-volume model [27] and assuming a Weibull distribution of free volume in a liquid, he showed that

$$\ln \frac{\eta(p)}{\eta_{p=0}} = \left[\frac{v_f^*}{v_f} \Gamma \left(1 + \frac{1}{n}\right) \right]^n, \quad (2.38)$$

where $\Gamma()$ is the gamma function, v_f^* denotes the “required free volume”, v_f is the free volume and n stands for the shape parameter of the Weibull distribution which assumed to be independent of pressure and temperature. By considering that the ratio v_f^*/v_f changes with pressure in the following way,

$$\frac{v_f^*}{v_f} = \left. \left(\frac{v_f^*}{v_f} \right) \right|_{p_0} \left(1 + \frac{p}{p_0}\right)^w, \quad (2.39)$$

where p_0' is a negative constant, if the gamma function is close to unity, follows a form similar to Eq. (2.36),

$$\ln \frac{\eta(p)}{\eta_{p=0}} = \left(\ln \frac{\eta_0}{\eta_e} \right) \left(1 + \frac{p}{P_0}\right)^{wn}, \quad (2.40)$$

where the product of w and n correspond to the pressure-viscosity-index z . The remaining drawback of this pressure-viscosity relation is, however, that it fails to describe the experimentally well-established change of the curvature of $\eta(p)$ at high pressures and low temperatures when approaching the glass transition point. In order to address this problem, newer literature refers to different approaches within free volume theory. Bair et al. (Ref. [21]) for instance reference the Doolittle equation in Ref. [28] or in Ref. [29], the authors are applying an equation proposed by Yasutomi et al. in Ref. [30].

Computational Details

Time integration of the equations of motion for the MD simulations given in Eq. (2.25) was performed by the *LAMMPS* MD simulator. The version used, “01 FEB 2014”, was built including only the “rigid” and the default packages. The calculations were carried out in parallel on an “*IBM System x iDataPlex dx360 M4*” equipped with 44 nodes, each providing 64 GB of RAM and two 8-core *Intel “Sandy Bridge”* CPUs. The final simulations of each of the 20 MD systems considered in this work were run on 8 cores for a duration of approximately 1.5 months.

Additional programs used for post-processing the MD data e.g., for plotting the graphs presented here, were written in the *Python* programming language. Time critical code, such as that used for auto- and cross-correlation, was implemented in *Fortran 95* coupled with *OpenMP* for multithreading capabilities.

The software written for this thesis covers the following topics:

- creation of *LAMMPS*-readable molecular structure files from “.mol2” files (this involves correct finding and naming of all angles, dihedrals and improper interactions from the given bond information);
- graphical assessment of the generated MD trajectories (variably smoothing and plotting of output);
- various calculations with time series of inter- and intramolecular vectors, angles and other parameters read from the very large output files e.g., for calculation of rotational correlation times from arbitrary intramolecular vectors, assessment of the structural dynamics of molecules;
- Green-Kubo-based viscosity calculations from the pressure tensor simulation output;
- various programs to plot and evaluate different types of datasets.

3.1 Selection of Molecules, State Points and System Size

The target simulated pressure range was chosen to be between 100 kPa and 1 GPa, hence spanning several orders of magnitude. The selection of substances and temperatures at which the MD simulations are to be carried out, is not trivial since it needs to be assured, that the substances stay in the liquid phase over the full pressure range. To find a suitable simulation temperature for the substances of interest, a literature survey of the solid/liquid and liquid/gas equilibria

was performed. By limiting the classes of chemically pure substances to alkanes, the following substances and temperatures were chosen for this work:

- *n*-Octane at 348.15 K,
- 2,2,4-trimethylpentane (*i*-octane) at 348.15 K,
- *n*-hexadecane at 473.15 K and
- (6*S*)-2,2,4,4,6,8,8-heptamethylnonane (*i*-hexadecane) at 473.15 K.

The structural formulas of these molecules are given in Fig. 3.1.

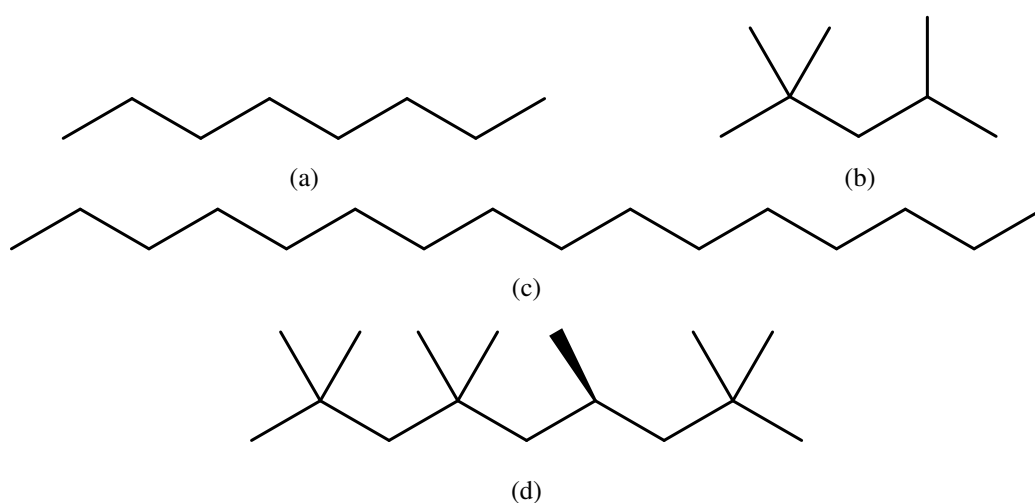


Figure 3.1: Structures of an (a) *n*-octane, (b) *i*-octane, (c) *n*-hexadecane and (d) *i*-hexadecane molecule.

The choice of the temperature for the octane MD systems was well below the boiling points of *n*- and *i*-octane at a pressure of 100 kPa, which are 399 K and 372 K respectively. The temperature determining quantity in the high pressure region is the liquid to solid phase transition. This transition was only assessed for the normal alkanes. Due to the lower molecular symmetry, the *i*-alkanes are expected to have lower melting temperatures when compared to the respective *n*-alkanes and hence should not limit the choice of the simulation temperature. Due to the lack of solid/liquid phase equilibrium data at close to 1 GPa for both octane isomers, an estimation was based on the phase equilibrium data for *n*-nonane available in Ref. [31] for pressures up to 0.9 GPa. A linear extrapolation of the published nonane data suggests a potentially overestimated melting point of 353 K at a pressure of 1 GPa. Since the octanes have a lower molecular mass than nonane, the melting point is also expected to be lower at the given pressure and thus the selection of 348.15 K seems justified.

The boiling points of *n*- and *i*-hexadecane at 100 kPa, 560 K and 513 K, are well above the selected 473.15 K for the hexadecane MD systems. The solid/liquid phase transition temperature for *n*-hexadecane at 1 GPa was extrapolated by using experimental data published in Ref. [32] by means of fitting a power law to the dataset. This yielded an estimated melting point of 440 K for *n*-hexadecane at 1 GPa and justifies the selection of 473.15 K for these MD systems.

To explore the pressure dependence of viscosity, pressures of 0.1, 250, 500, 750 and 1000 MPa were selected in the range of 100 kPa to 1 GPa for each of these molecules.

The selection of the system size, in this case the number of molecules in the MD simulations is governed by two main considerations:

1. Available computational resources and desired trajectory length.
2. Reduction of finite size effects due to small system size.

Since the available computational resources are usually fixed by external factors, a trade off between trajectory length and system size must be found. On one hand, Yeh et al. claim in Ref. [33] that the calculation of shear viscosity exhibits only weak dependence on the size of the simulated systems. However, they do not rule out effects due to long-time tails of the shear stress autocorrelation functions. Levashov et al. in Ref. [34], on the other hand, point out that thermally excited shear waves that contribute to viscosity show large spatial correlation and display complex phenomena when periodic boundary conditions are applied.

Since the rigorous determination of the effects of differently sized systems on the viscosity was beyond the scope of this thesis, the MD systems included 1024 molecules for the octane systems and 512 molecules for the hexadecane systems. These values compare well to other studies in this field, e.g. see Refs. [35–37].

3.2 Force Field, Long-range Corrections and Cutoff Distances

The selection of a force field that fits the purpose of this work is crucial for obtaining MD results close to reality. One of the commonly used force field for simulating organic liquids and especially alkanes is the “*Optimized Potentials for Liquid Simulations*” (OPLS) developed by Jorgensen et al. [38, 39]. Several different sets of parameters for OPLS have been applied in literature [19, 40, 41]: all atom models, united atom models as well as modified versions. Siu et al. [41], refined the original OPLS all atom (OPLS-AA) parameters for simulations of alkanes with more than 6 carbon atoms. They achieved a better agreement of the simulated viscosities, densities and conformational properties with experimental values when compared to the original OPLS-AA parameter set. For this work, a slightly modified implementation of the reassigned OPLS-AA parameters (termed L-OPLS) was used and extended to iso-alkanes. The adoptions made are:

- hydrogen bond lengths were not restrained to the equilibrium value (no SHAKE or LINCS algorithm was used);
- the pairwise interaction and the charge for hydrogen atoms bound to tertiary carbon atoms was chosen to be the same as for hydrogens bound to secondary carbon atoms and the charge of the respective tertiary carbon atom was chosen to achieve neutrality.

The restraining of the hydrogen atoms was omitted in order to reduce the complexity of the Hamilton function and to allow for possible changes in the equilibrium bond length at high pressures and hence to get a possibly more accurate pressure dependence of density and viscosity. However, leaving the hydrogen atoms to freely oscillate, increases the computational costs. This is due to the H-bond stretching being the fastest dynamical process in the system, requiring an integration timestep of only 0.5 fs to ensure the energy conservation. Another effect of not restraining the hydrogen bond lengths is that the dihedral energy landscape of the carbon backbone in alkanes is slightly altered (see Fig. 3.2). In order to obtain the angle dependence of the dihedral energy as calculated by ab-initio methods in Ref. [41], a refit of the dihedral potential parameters with free hydrogen atoms would be necessary. Since the difference is small, the original potential parameters with the given modifications were used.

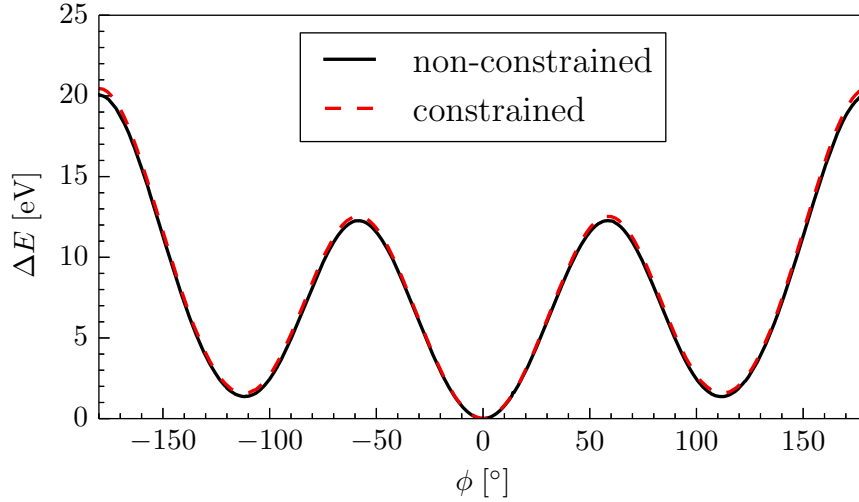


Figure 3.2: The energy of the $C_2 - C_3 - C_4 - C_5$ dihedral in n -hexane as a function of the dihedral angle relative to the trans position for (non-) constrained hydrogen bond lengths.

The properties of iso-alkanes were not treated by Siu et al. and thus no parameters were given for hydrogen atoms bound to tertiary carbon atoms. Therefore, the original OPLS-AA non-bonded parameter for these hydrogen atoms was used.

In order to be able to work with periodic boundary conditions and to keep computational costs at a minimum, cutoff distances for pairwise force calculations were defined. The cutoff distances for van der Waals (vdW) as well as electrostatic interactions was chosen to be 13.0 \AA . At this distance the longest ranged vdW interaction energy (C-C) drops to a value 1.5×10^{-3} times the value at the energy minimum. Dysthe et al. in Ref. [19] claim, that the effects of the choice of the cutoff distances on the calculated viscosity is small. However, since Dysthe et al. conducted their tests only in gas phase simulations. In this thesis, the effects of the vdW cutoff on the total energy and pressure were corrected by the equations

$$\begin{aligned}
 E_{\text{LRC}} &= \frac{1}{2} \sum_{i=1}^n N'_i \sum_{j=1}^n 4\pi\rho'_j \int_{r_c}^{\infty} g_{ij}(r) E_{ij}(r) r^2 dr \quad , \\
 p_{\text{LRC}} &= \frac{1}{6} \sum_{i=1}^n \rho'_i \sum_{j=1}^n 4\pi\rho'_j \int_{r_c}^{\infty} g_{ij}(r) \left[r \frac{dE_{ij}(r)}{dr} \right] r^2 dr \quad ,
 \end{aligned}
 \tag{3.1}$$

provided by Sun in Ref. [42]. In Eqs. (3.1) the sums run over all n different atom types, N'_i denotes the total number of atoms of type i , ρ'_i is the number density of atom type i in the MD system. g_{ij} denote the radial pair distribution functions (RDF) and $E_{ij}(r)$ is the distance dependent interaction energy between atom type i and j .

To apply these equations, the RDF should be converged to unity at the force cutoff distance. It was found, that $g(r)$ is close to one at 13.0 \AA for all systems near atmospheric pressure, see figure Fig. 3.3. However, when the pressure for normal alkanes increases to 1 GPa, the fluctuations in $g(r)$ at close to 13.0 \AA become larger when compared to lower pressures, see Fig. 3.4, although its value is still close to unity.

Although the requirement of $g(r) = 1$ for distances larger than the cutoff is not strictly fulfilled, especially for the MD systems at high pressure, the tail correction is applied in all the MD simulations to provide comparability.

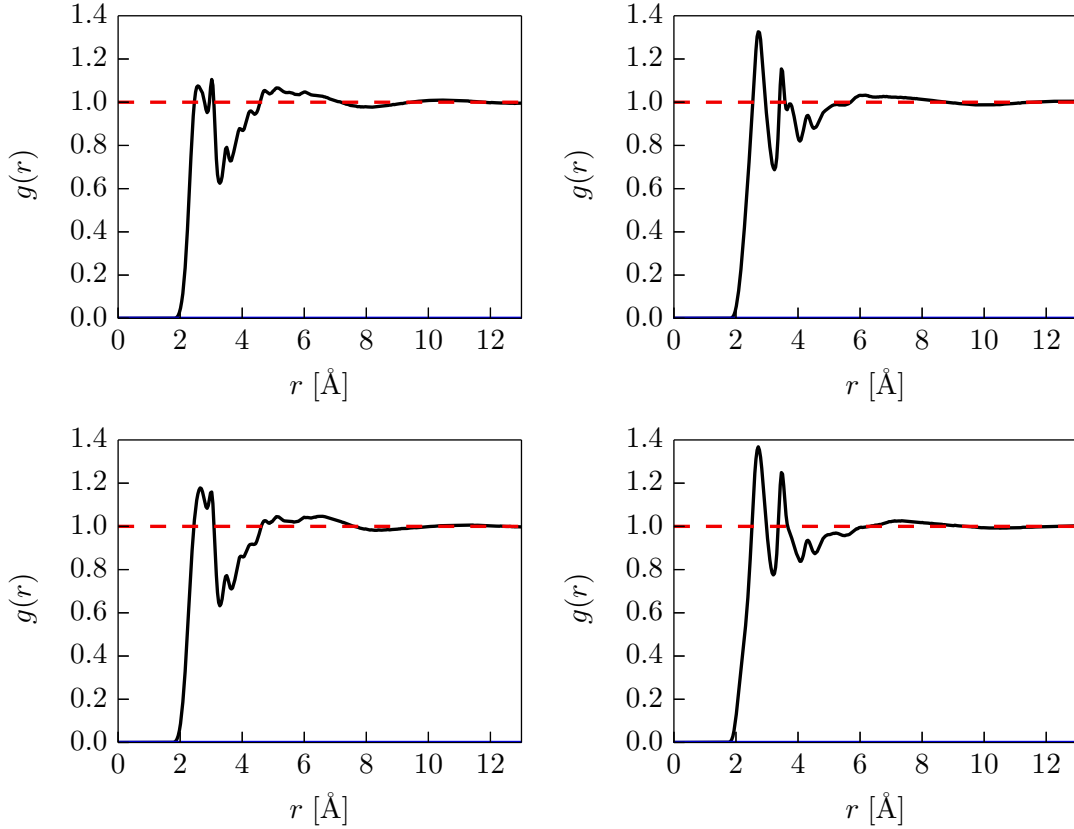


Figure 3.3: All-atom radial distribution functions $g(r)$ at equilibrium for n -octane (top left), i -octane (top right), n -hexadecane (bottom left) and i -hexadecane (bottom right) and a pressure of 100 kPa. The dashed, horizontal line marks the unity.

Furthermore, to keep consistency with the simulations published by Siu et al. in Ref. [41], electrostatic long range forces are included in the simulations. The “*Particle-Particle Particle-Mesh*” (PPPM) solver described by Hockney et al. in Ref. [43] was used with a maximum relative error in the force calculations of 10^{-5} to include Coulomb interactions also beyond the cutoff distance.

3.3 Time Integration

The proper selection of the time integration algorithm is important for achieving a good computational efficiency. The integrator used for all the MD simulations here was the “*reversible REference System Propagator Algorithm*” (rRESPA) introduced by Tuckerman et al. [11]. Using this integration scheme, it is possible to optimize the calculations of the computationally most expensive pairwise interactions. This is achieved by introducing multiple timesteps for the computation of interactions over different length scales. For further details about this algorithm the reader is referred to the description of the rRESPA v2 algorithm on page 16.

This integration scheme enables an outer timestep of 4 fs with good energy conservation, recall Eq. (3.2). A comparison of the computational efficiency for various integration schemes on 8 cores is given in Tab. 3.1. The computational efficiency was assessed by comparing the time needed to calculate a trajectory with a total simulated duration of 100 ps for the 100 kPa n -hexadecane MD system used for this work.

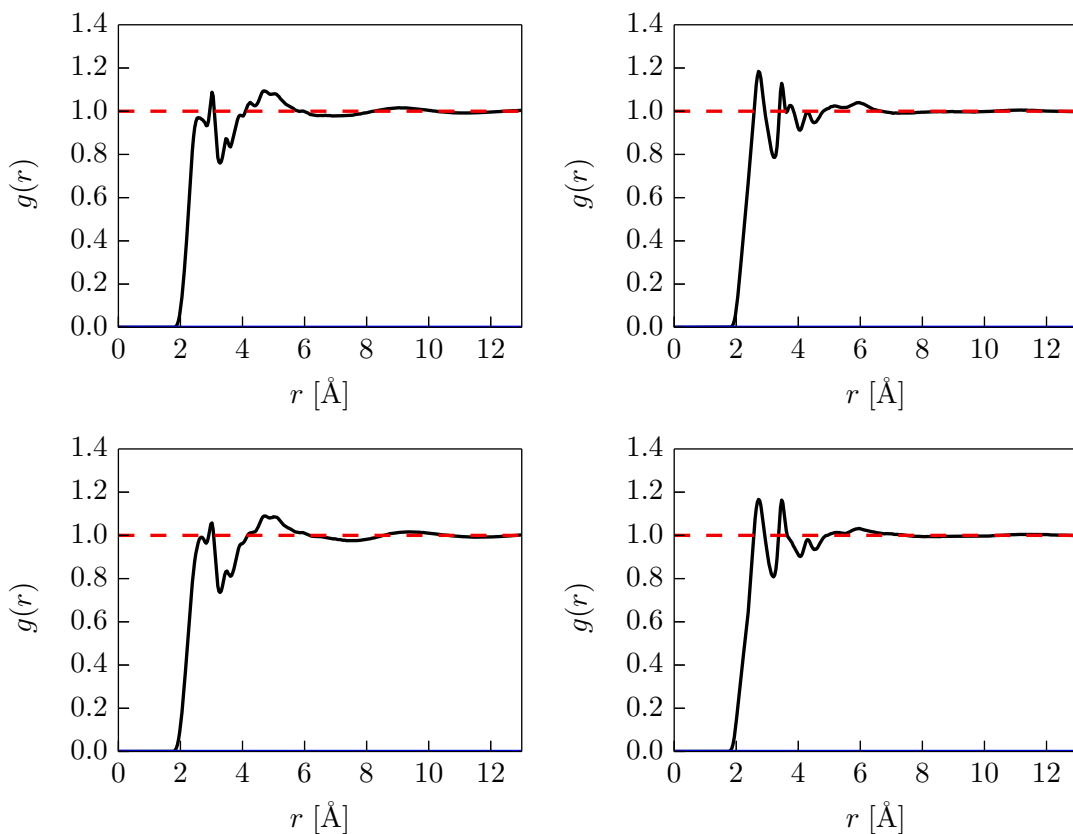


Figure 3.4: All-atom radial distribution functions $g(r)$ at equilibrium for n -octane (top left), i -octane (top right), n -hexadecane (bottom left) and i -hexadecane (bottom right) and a pressure of 1 GPa. The dashed, horizontal line marks the unity.

Integrator	rel. computational cost
Verlet	3.2
rRESPA v1	1.8
rRESPA v2	1.0

Table 3.1: A comparison of computational cost for different integration algorithms relative to the rRESPA v2 algorithm.

The time integration algorithms tested were:

Verlet standard Verlet integrator with a timestep of 0.5 fs

rRESPA v1 a multi-timestep algorithm with 3 levels: level 1 is calculated with a timestep of one fourth and level 2 at half of the outer, level 3, timestep of 2 fs such that at level 1 intramolecular forces are calculated, at level 2 van der Waals and Coulombic interactions within the cutoff radius and at level 3 long range Coulombic interactions are updated.

rRESPA v2 is a multi-timestep algorithm with 4 levels. The levels are separated by a time factor of 2 each, meaning that the inner level (level 1) is updated every 0.5 fs if the outer timestep is 4 fs. All intramolecular forces were calculated at level 1, in level 2, 3 and 4 the pairwise interactions were split by additional cutoff distances. The *LAMMPS* implementation of this feature allows to specify 2 cutoff distances per level for the “inner” and

“middle” distances. The “inner” interactions were calculated at the rRESPA level 2 and include full pairwise interactions of up to $r_1 = 4.5 \text{ \AA}$ distance. From r_1 to $r_2 = 6.0 \text{ \AA}$, the forces were linearly down-scaled to zero. The “middle” interactions were calculated on level 3 and included forces up-scaled from zero at r_1 to full strength at r_2 as well as the full forces of up to a distance of $r_3 = 8.0 \text{ \AA}$. In the range from r_3 to $r_4 = 10.0 \text{ \AA}$ the forces were again down-scaled to zero in the “middle” region and up-scaled from zero to full for the “outer” region which is calculated at rRESPA level 4. The pairwise interactions between r_4 and $r_c = 13.0 \text{ \AA}$, the overall force cutoff, are taken into account by the “outer” level, see Fig. 3.5 for a graphical illustration.

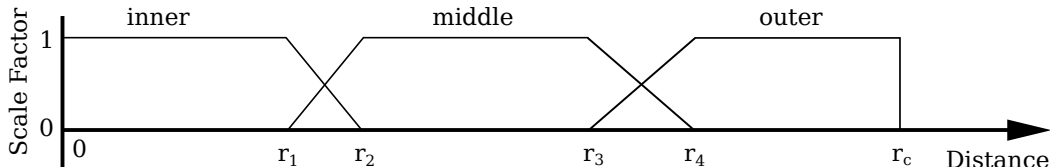


Figure 3.5: An illustration of the distance stepped “rRESPA v2” algorithm. It depicts the force scaling in the inner, middle and outer regions as a function of relative distance between two atoms. The radii r_{1-4} represent parameters of the integrator, while r_c is the overall force cutoff radius.

Note that the rRESPA v2 time integration algorithm is used for all simulations published within this work.

3.4 Thermostatting

The need for thermostatting the simulated molecules arises from the high sensitivity of the Green-Kubo formalism to drifts in the total pressure, especially when calculating the bulk viscosity. This drift can be caused by numerical errors made in the time integration algorithms in conjunction with systematic errors like van der Waals force cutoff or the limited accuracy of long range Coulombic interactions. These errors lead to a not perfectly conserved total energy for the microcanonical (NVE) ensemble. This unphysical change in the total energy leads to increasing temperature and thus to an increase in the pressure due to the constant simulation box volume. Although in a practical situation, this drift can be kept low by reducing the simulation timestep or employing a different time integration algorithm than rRESPA v2, nevertheless, a balance between integration accuracy and total computational cost needs to be found. Within this work, a timestep of 4 fs together with the above described rRESPA v2 algorithm ensured a drift in the total energy E (kinetic plus potential energy) within all simulations of less than

$$\frac{\Delta E}{E \Delta t} < 5 \times 10^{-5} \text{ ns}^{-1} \quad . \quad (3.2)$$

The energy drift was assessed by analyzing the change in total energy of the thermostats in the equilibrated MD simulations. This change corresponds to the energy transferred to or from the MD systems to keep them at a constant temperature. Since no energy is added or taken from the MD simulations on purpose, this change likely results from errors in the time integration scheme. Because the energy drift is not zero and the MD simulations are run over several tenths of nanoseconds, the temperature needs to be kept constant by means of a thermostat. Accordingly, the considered ensemble is changed to the canonical (NVT).

The NVT ensemble can be achieved by employing a Nosé-Hoover chain thermostat [9, 10], see chapter 2 for more details. The practical challenge, however, is to find an appropriate coupling constant of the thermostat to the MD system. According to the work of by Basconi et al. [44], on one hand, undercoupling the thermostat can result in distortions of the long-term phenomena (longer than a nanosecond) and, on the other hand, overcoupling results in significantly altered short term dynamics and differences in structural relaxations. In their work, Basconi et al. showed that the effect of a properly coupled Nosé-Hoover chain thermostat on the MD simulated viscosity of liquids is negligible.

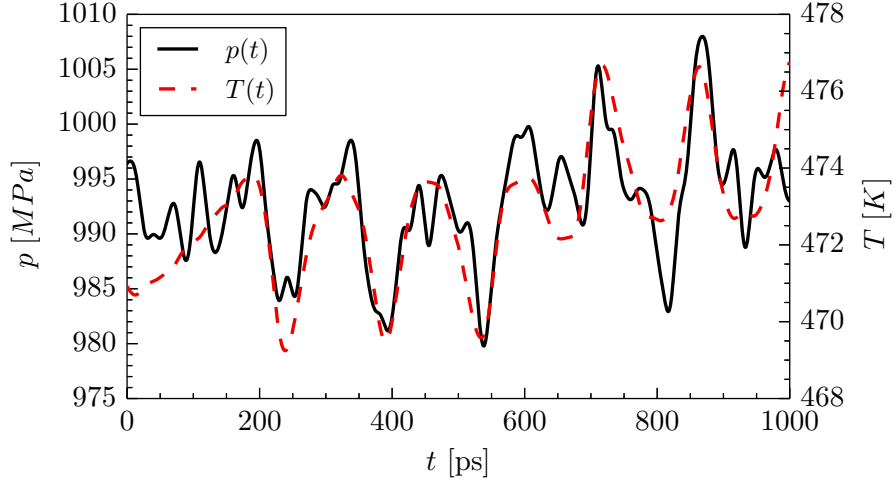


Figure 3.6: The effect of undercoupling a Nosé-Hoover thermostat to a *n*-hexadecane MD system at roughly 1 GPa pressure and 473.15 K, when the coupling parameter is set to 20 ps.

The effect of undercoupling is demonstrated in Fig. 3.6. The variation in total energy introduced by the thermostat leads to an oscillating temperature and ultimately influences the pressure on a timescale which could be problematic when determining the viscosity by the Green-Kubo formalism. This effect was found to be especially pronounced at high pressures and hence a MD system at 1 GPa was used to provide the example given in Fig. 3.6. Overcoupling results in an increase of rotational correlation times (RCT) with respect to an NVE ensemble. In Table 3.2 the results of testing the influence of the thermostat relaxation time (T_{damp} in *LAMMPS*) on the RCT at an atmospheric pressure for *n*-hexadecane at 473.15 K are given. Note that a lower value of T_{damp} corresponds to stronger coupling of the thermostat to the system.

Ensemble	T_{damp} [ps]	RCT [ps]	Deviation [%]
NVE	-	35.6	0.0
NVT	1.00	35.6	0.0
	0.10	35.8	0.6
	0.01	38.5	8.1

Table 3.2: Effect of the thermostat relaxation time T_{damp} on the rotational correlation time (RCT) in case of *n*-hexadecane at 100 kPa and 473.15 K.

In order to ensure that overall translational dynamics are not influenced by the thermostat as well as to be able to average over the effects of the thermostat in the pressure tensor with high statistical significance, T_{damp} was chosen to be 0.1 ps in all MD simulations.

The chain length of the thermostat was chosen to be 4, Cancès et al. recommend a chain length of ≥ 3 in Ref. [45], in order to improve ergodicity over a non-chained Nosé-Hoover thermostat, see Ref. [10].

Results and Discussion

The output from the MD simulations comprises all 6 independent components of the full pressure tensor, all 6 components of every intramolecular contribution to the total pressure tensor (resulting from the kinetic contribution, bond, angle and dihedral forces) as well as the total and potential energy. These (double precision) values are printed into a text file at every outer timestep of 4 fs, see Appendix A. According to the Nyquist-Shannon sampling theorem, a sampling rate of 250 samples/ps allows to correctly sample the highest frequency motion within the system, i.e., the C-H bond stretching occurring a frequency of about 90 ps^{-1} .

In addition to this detailed output, averaged quantities with lower precision are also written to a file to monitor the MD simulations conveniently. Thus the following quantities are output after averaging over 80 fs: pressure, temperature, kinetic energy, potential energy, total energy, thermostat energy, van der Waals energy, Coulomb energy, long-range Coulomb energy, bond energy, angle energy and dihedral energy. In order to be able to determine the dynamics of structural properties of the molecules, the position of every atom during the MD simulation is written to a dump-file every 250 timesteps (1 ps), see Appendix A.

4.1 Detection of Equilibrium

The purpose of equilibration is to provide a starting MD system where not only the velocities of the involved atoms are drawn from the canonical distribution, but also the positions and orientations of the molecules are compatible with the chosen ensemble. This is achieved by initially creating a system of molecules (which is usually highly ordered and at zero absolute temperature) and then applying a thermostat to heat the system up to the desired temperature. It is assumed that given sufficient time the system will converge towards an equilibrium state that corresponds to the canonical ensemble. The processes of system creation, equilibration and data production was split into the following tasks:

1. creating atomic coordinates corresponding to the respective molecular structure by minimizing the potential energy;
2. finding and parameterizing all involved bonds, angles and dihedrals as well as the non-bonded properties of all atoms, according to a modified L-OPLS force field;
3. importing the structure and parameters to *LAMMPS* and replicating the molecules to a total number of 1024 molecules for the octane isomers and 512 molecules for the hexadecane isomers;

4. adjusting the simulation box dimension to create a cubic box and heating each of the 4 systems to the desired temperature;
5. isotropically adjusting the simulation box dimensions of MD systems to come close to the experimental densities of the liquids at atmospheric pressure;
6. replicating the four “seed” systems five times and adjust the pressure in each MD system to the respective target pressure;
7. fine adjusting the volumes of MD systems;
8. data production.

Being able to concentrate and optimize one of these tasks at a given time this achieves a certain modularity and helps to reduce difficulties associated with the handling of large data files. The practical implementation of all points listed above can be summarized as follows.

1. The freeware *Avogadro*^a was used for easy and intuitive creation of molecular structures that can be energy-minimized by assuming various force fields , e.g., the “Universal Force Field” (UFF). The structures can then be exported in the “.mol2” file format for further usage.
2. A Python script was written to find all possible bond, angle, dihedral and improper interactions from an imported molecular structure. The force field parameters can be then easily added to the generated output file.
3. After importing the generated molecular structure, the corresponding *LAMMPS* “replicate” command can be used to create the initial systems.
4. To increase the temperature to the target one, a Langevin thermostat was used. The total number of simulation steps in this task was 20.000.
5. Using the isothermal-isobaric ensemble (NPT), the volume of the system was allowed to change to achieve a pressure of approximately 100 kPa. The total number of simulation steps in this task was 15.000.
6. From small test simulations the volume of the MD systems at the desired pressures can be roughly estimated. The volume for the main MD simulations was based on this estimations and the MD simulations were continued for the NVT ensemble over 800.000 timesteps.
7. In order to bring the system pressures closer to the target pressures, a further, small, adjustment to the system volumes was applied and the NVT simulation was run for further 200.000 timesteps.
8. The systems prepared in this manner are then used for the production of data to which the Green-Kubo method and others can be applied (after an additional check whether equilibrium can be assumed).

^aavogadro.cc

Each of the total 20 MD systems was simulated for more than 4 ns before any MD data was considered for the calculation of physical properties (including the check for equilibrium). In Fig. 4.1 the initial phase of a *n*-hexadecane system equilibration process are depicted (the volume of the simulation box was not yet adjusted to yield the density at atmospheric pressure).

In order to demonstrate the structure of a *LAMMPS* input script, an example of a data production script is given in Appendix A.

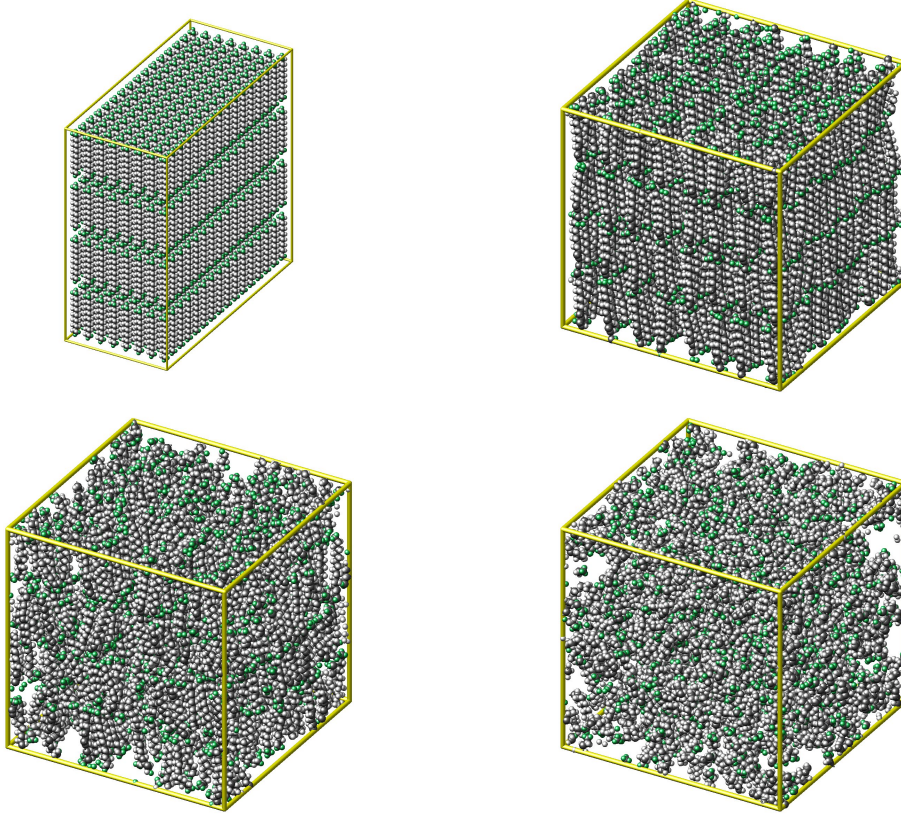


Figure 4.1: Snapshots of the simulation box for *n*-hexadecane at various stages of the equilibration process. The snapshot at the top left shows the initial arrangement of molecules, the second snapshot in the top right corner gives the box after adjusting its dimensions to a cube and for a temperature slightly above absolute zero (10 K). The snapshots in the second row (from left to right) were taken at 60 and 120 ps after the equilibration started and the temperature was increased to 250 and 473.15 K, respectively.

In order to apply the Green-Kubo formula to determine the equilibrium shear and/or bulk viscosity of an MD system, the simulated trajectories need to have reached a steady state. In order to find out whether the simulations correspond to a steady state, Jones and Mandadapu [17] suggested to use the Hellinger metric

$$\|\rho^{(m)}(\xi) - \rho^{(m-1)}(\xi)\|_H = \left[\int_{\Omega} \left(\sqrt{\rho^{(m)}(\xi)} - \sqrt{\rho^{(m-1)}(\xi)} \right)^2 d\xi \right]^{\frac{1}{2}}, \quad (4.1)$$

to compare the probability density functions $\rho^{(m)}(\xi)$ of the quantity $\xi(t)$, e.g., the time-dependent pressure of the system or a single component of the pressure tensor. Here $\rho^{(m)}(\xi)$ is calculated by using normalized histograms of the time series of $\xi(t)$ divided into N_m blocks. Since Jones and Mandadapu used a cumulative calculation of $\rho^{(m)}(\xi)$, this is calculated on the basis of all the

samples of $\xi(t)$ that were already used to calculate $\rho^{(m-1)}(\xi)$ plus the number of samples in one additional block. In Eq. (4.1) Ω represents the union of the supports of $\rho^{(m)}(\xi)$ and $\rho^{(m-1)}(\xi)$.

In order to circumvent unnecessary loss of simulation data, the method described by Jones and Mandadapu was modified by avoiding a cumulative calculation of the density functions and introducing an estimate of the equilibrium density distribution function ρ_{eq} as follows,

$$\|\rho^m(\xi) - \rho_{eq}\|_H = \left[\int_{\Omega} \left(\sqrt{\rho^m(\xi)} - \sqrt{\rho_{eq}} \right)^2 d\xi \right]^{\frac{1}{2}}, \quad (4.2)$$

where $\rho^m(\xi)$ is calculated from a histogram of data contained only in block m . An estimate for ρ_{eq} can be obtained from a histogram over a suitable region of the trajectory. Here and further on, the beginning and end of this region will be denoted by t_{eq} and t_{run} respectively, refer to Fig. 4.2 for a graphical illustration. This method allows for direct comparison of the m -series of Hellinger distances without the need of separating the influence of statistics from the influence of non-steady state contributions. It must be noted, however, that this m -series of Hellinger distances for a given, finite trajectory does not converge to zero but rather to a finite value, see Appendix B. Thus, when comparing this Hellinger distance for different MD systems, it must be ensured that the number of $\xi(t)$ samples in block m is the same.

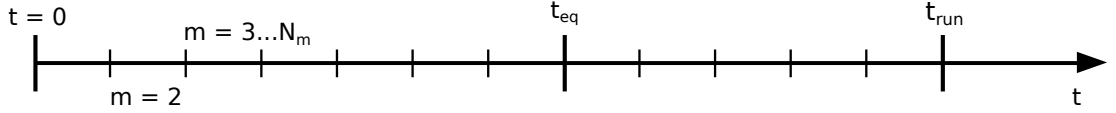


Figure 4.2: Illustration for the time-parameters t_{eq} : the time moment from which the MD system can be considered as being in equilibrium, t_{run} : the total simulated time and for the block index m .

In Figs. B.1-B.5, the results of applying this method to the simulated systems after the equilibration is shown. The first $t_{run} = 30$ ns of the trajectories were used and split into $N_m = 60$ blocks, each containing $N_{block} = 1.25 \times 10^5$ samples of the average over all off-diagonal elements of the pressure tensor

$$p^{off} = \frac{1}{3} \sum_{\mu < \nu} \sigma_{\mu\nu}. \quad (4.3)$$

The number of bins for the histograms was chosen to be 49 (the rounded off value of the cubic root of the number of samples per block). Note the difference in the y-axis when comparing figures for different pressures.

Another method of assessing the convergence of a MD system to its equilibrium is to check the convergence of a variable of interest with respect to its equilibrium value,

$$|\langle \xi \rangle_m - \langle \xi \rangle_{eq}| = \left| \frac{1}{m_{stop} - m_{start}} \int_{m_{start}}^{m_{stop}} \xi(t) dt - \frac{1}{t_{run} - t_{eq}} \int_{t_{eq}}^{t_{run}} \xi(t) dt \right|, \quad (4.4)$$

where m_{start} and m_{stop} represent the time of the first and last sample of $\xi(t)$ in block m . Figs. B.6-B.10 display the convergence of p^{off} to its equilibrium value. $\langle p^{off} \rangle_m$ represents the block average of block m and $\langle p \rangle_{eq}$ is an estimation for the equilibrium value calculated by averaging over the last half of the 30 ns trajectory. Note the difference in the y-axis when comparing different pressures.

A system is considered to be in equilibrium, as soon as the results of both methods proposed above are independent of m .

When the influence of the choice of t_{eq} on the result is examined, it is found to be small for all systems (t_{run} was fixed at 30 ns), and hence will not be treated in detail, an illustration is given in Fig. 4.3.

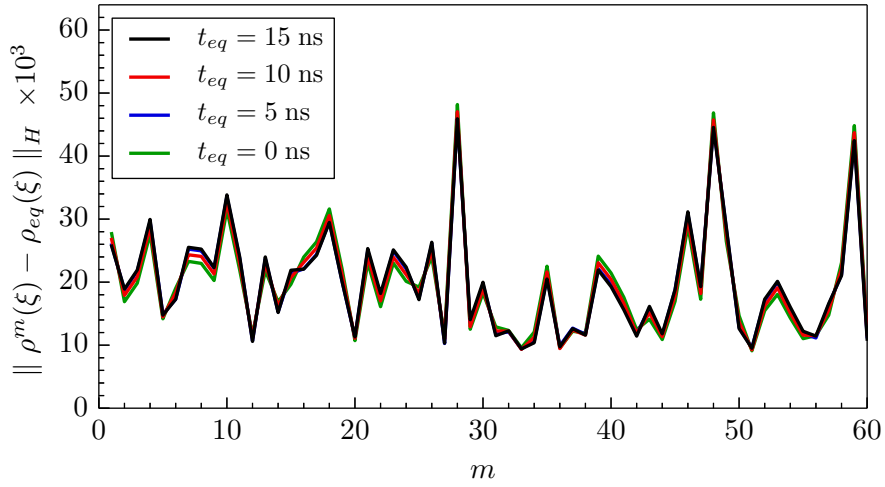


Figure 4.3: The influence of t_{eq} , see Fig. 4.2, on the Hellinger metric for the n -octane system at 1 GPa and 348.15 K.

The results of the equilibrium detection, as quantified in Eqs. (4.2) and (4.4) and provided by Figs. B.1-B.10, are summarized in Tab. 4.2. For the parameters chosen refer to Tab. 4.1.

The parameters used to calculate the Hellinger metric and the block averages are given in Tab. 4.1. It summarizes the maxima of the Hellinger metric HM_{max} as well as the maximum deviation of the average of the off-diagonal pressure tensor elements from their estimated equilibrium values Δp_{max}^{off} and $\langle p^{off} \rangle_{eq}$. In this section, only the maxima of the different methods are listed. Full graphs of the Hellinger metric or the block averages as a function of the block index m can be found in Figs. B.1-B.10 in the appendix.

N_m	=	60
t_{run}	=	30 ns
t_{eq}	=	15 ns

Table 4.1: Parameters used for equilibrium detection.

System	$\langle p \rangle_{eq}$ [MPa]	$HM_{\max} \times 10^3$	Δp_{\max}^{off} [MPa]
<i>n</i> -octane	0.01	13.4	0.17
	249.01	17.0	0.46
	503.76	26.1	1.03
	752.47	37.8	1.67
	995.13	46.0	2.17
<i>i</i> -octane	0.57	14.8	0.33
	248.62	16.1	0.51
	502.80	29.7	1.26
	751.83	45.9	2.15
	995.56	75.8	3.62
<i>n</i> -hexadecane	0.29	14.0	0.25
	249.64	17.8	0.67
	503.70	22.2	0.97
	751.88	32.9	1.73
	994.24	27.2	1.51
<i>i</i> -hexadecane	0.04	13.0	0.32
	249.29	25.6	1.23
	502.15	44.3	2.45
	748.24	92.2	5.48
	987.35	135.2	8.31

Table 4.2: Maximum value of the Hellinger metric HM_{\max} and that of the absolute deviations Δp_{\max}^{off} of the average of the off-diagonal components of the pressure tensor p^{off} , see Eq. (4.3), from its equilibrium value for an estimated pressure $\langle p \rangle_{eq}$ and a temperature of 348.15 K for the octane isomers and of 473.15 K for the hexadecane isomers, respectively.

As can be observed from Tab. 4.2, the Hellinger metric as well as the deviation of the average over the off-diagonal pressure tensor elements from its equilibrium value exhibit stronger fluctuations and a higher absolute magnitude for the *i*-hexadecane MD systems at pressures greater than 250 MPa when compared to all other MD systems investigated here. This suggests, that the *i*-hexadecane systems at pressures greater than 250 MPa might not be in full equilibrium and hence, results reported for these systems should not be considered as being reliable. When including the results from the rotational correlation time evaluation, see Tab. 4.7, these findings are additionally backed up since τ_1^{rot} significantly exceeds the total equilibration time and in case of 1 GPa even the total simulated time.

All other MD systems behave consistently and do not show significant drifts in the calculated metrics. Hence, it is assumed that initial equilibration phase of approximately 4 ns is sufficient to provide systems that are well converged to an equilibrium. Therefore the data from these 4 ns is not included in any of the calculations performed or graphs plotted for this work.

4.2 Zero-shear and Bulk Viscosities

The calculation of viscosity-related quantities is performed in close agreement with post-processing methods published by Jones and Mandadapu [17]. The discretized versions of Eqs. (2.20) read

$$\xi_\tau(N_c \Delta t) \approx \sum_{j=0}^{N_c} \frac{\lambda}{N_r N_\tau} \sum_{r=1}^{N_r} \sum_{i=1}^{N_\tau} \xi_r(i \Delta t) \xi_r((i+j) \Delta t) \Delta t \omega_j \quad \lambda = \frac{V}{k_B T} \quad , \quad (4.5)$$

and can be applied directly to calculate viscosities $\xi_\tau(N_c \Delta t)$ of the liquids from MD data. See Tab. 4.3 for an explanation of the notation used. The exact nature of the result $\xi_\tau(N_c \Delta t)$ depends on the choice of ξ_r . Is ξ_r chosen to be one of the off-diagonal elements of the pressure tensor, the result corresponds to the shear viscosity of the MD system. By using the diagonal components of the stress tensor and applying the corrections given in Eq. (2.18), the bulk viscosity can also be obtained. The sum over all replicas N_r of the system includes the total number of simulations for the MD and additionally, some symmetry considerations. This means that under the assumption that no anisotropic phase was formed, all three off-diagonal components of the pressure tensor are independent of each other and hence can according to Ref. [17] be considered different replicas of the same MD system.

Δt	simulation time step
N_a	initial number of samples per block
N_b	number of blocks
N_c	number of samples used for correlation
N_r	number of independent replicas of the system
N_τ	total number of timesteps in the simulation
ω_i	quadrature weights
V	volume of the system
k_B	Boltzmann constant
T	temperature

Table 4.3: Computational parameters.

In order to estimate the errors in the calculated viscosities, Jones and Mandadapu applied the method of the large-block limit for block averages. This method can be implemented by

splitting the N_τ simulation trajectories (consisting of N_τ samples) into blocks of length N_a each and then recursively increasing the block size by averaging over the blocks of smaller size. By calculating the standard deviation of the resulting quantity as a function of block size and taking the limit of infinite block size one can at least in principle estimate the error in the results due to finite averaging. Jones and Mandadapu provided a method to estimate an upper boundary of the variance in case of transport coefficients,

$$\text{var}\xi_\tau(\tau_c) < 4\xi^2 \frac{\tau_c}{\tau} \quad , \quad (4.6)$$

when ξ is replaced by a sufficiently accurate estimate ξ_τ . A further input parameter that is needed for calculating the correlation is the significant correlation time. Jones and Mandadapu recommend to estimate this by a prior guess of the relevant transport coefficient (or obtaining it from other sources). This method was found to be only of limited value for this work since the viscosity depends exponentially on pressure which makes it hard to estimate. Thus, other means of finding the upper limit for the correlation time were used. Cui et al. proposed to use the rotational correlation time (τ^{rot}) of molecules as a natural time scale for liquids [13,46]. By using a small multiple (2 is used in this work) of τ^{rot} which can easily be calculated from the MD data as the significant correlation time τ_c , one circumvents the need for having good prior estimates for the transport coefficients.

In addition, for calculating the viscosity of MD systems by autocorrelating the pressure tensor elements as given by Eq. (2.26), the same formalism can be applied to “partial” formulations of the pressure tensor which only include certain contributions to the total $\sigma_{\mu\nu}$. These contributions can be restricted to include only specific terms like e.g., the kinetic term, or certain components of forces \mathbf{F}_i according to Eq. (2.27). The “partial” viscosities calculated in his way, do not sum up to yield the total zero-shear viscosity as calculated by autocorrelation and integration of the full pressure tensor. This is a direct consequence of the inherent nonlinearity of the autocorrelation and can be demonstrated on an example comparing the full pressure tensor autocorrelation

$$\begin{aligned} C^{tot}(\tau) &= \underbrace{(\mathcal{K}(t) + \mathcal{V}(t))}_{\sigma_{\mu\nu}(t)} \underbrace{(\mathcal{K}(t+\tau) + \mathcal{V}(t+\tau))}_{\sigma_{\mu\nu}(t+\tau)} \\ &= \mathcal{K}(t)\mathcal{K}(t+\tau) + \mathcal{V}(t)\mathcal{V}(t+\tau) + \mathcal{K}(t)\mathcal{V}(t+\tau) + \mathcal{V}(t)\mathcal{K}(t+\tau) \\ &\neq \mathcal{K}(t)\mathcal{K}(t+\tau) + \mathcal{V}(t)\mathcal{V}(t+\tau) = C^{kin}(\tau) + C^{vir}(\tau) \quad , \end{aligned} \quad (4.7)$$

with the sum of the autocorrelations

$$C^{kin}(\tau) = \mathcal{K}(t)\mathcal{K}(t+\tau) \quad , \quad (4.8)$$

and

$$C^{vir}(\tau) = \mathcal{V}(t)\mathcal{V}(t+\tau) \quad , \quad (4.9)$$

obtained from the kinetic

$$\mathcal{K}_{\mu\nu}(t) = \sum_{i=1}^N m_i v_{i\mu}(t) v_{i\nu}(t) \quad , \quad (4.10)$$

and the virial

$$\mathcal{V}_{\mu\nu}(t) = \sum_{i=1}^N r_{i\mu}(t) F_{i\nu}(t) \quad , \quad (4.11)$$

contributions separately. For the sake of readability the indices μ and ν were omitted in the expressions for $C^{tot}(\tau)$, $C^{kin}(\tau)$, $C^{vir}(\tau)$ $\mathcal{K}(t)$ and $\mathcal{V}(t)$ in the Eqs. (4.7-4.9).

The results of the viscosity calculations by applying the Green-Kubo formula are given in Tabs. 4.4 and 4.5 and are plotted in Fig. 4.4. The listed viscosities represent the maximum of the time integral over the autocorrelation functions in the interval from $\tau_c = 0$ to $\tau_c = 2\tau^{rot}$ (τ^{rot} was calculated from vector A - refer to section 4.3 and Tab. 4.7 for further details), see also Appendix C. Due to excessively high τ^{rot} in the *i*-hexadecane systems at 750 MPa and 1 GPa, the upper autocorrelation and integration limit was fixed to 6 ns. The total amount of simulation data available for analysis of each system τ_{run} , is provided in Tabs. 4.4 and 4.5.

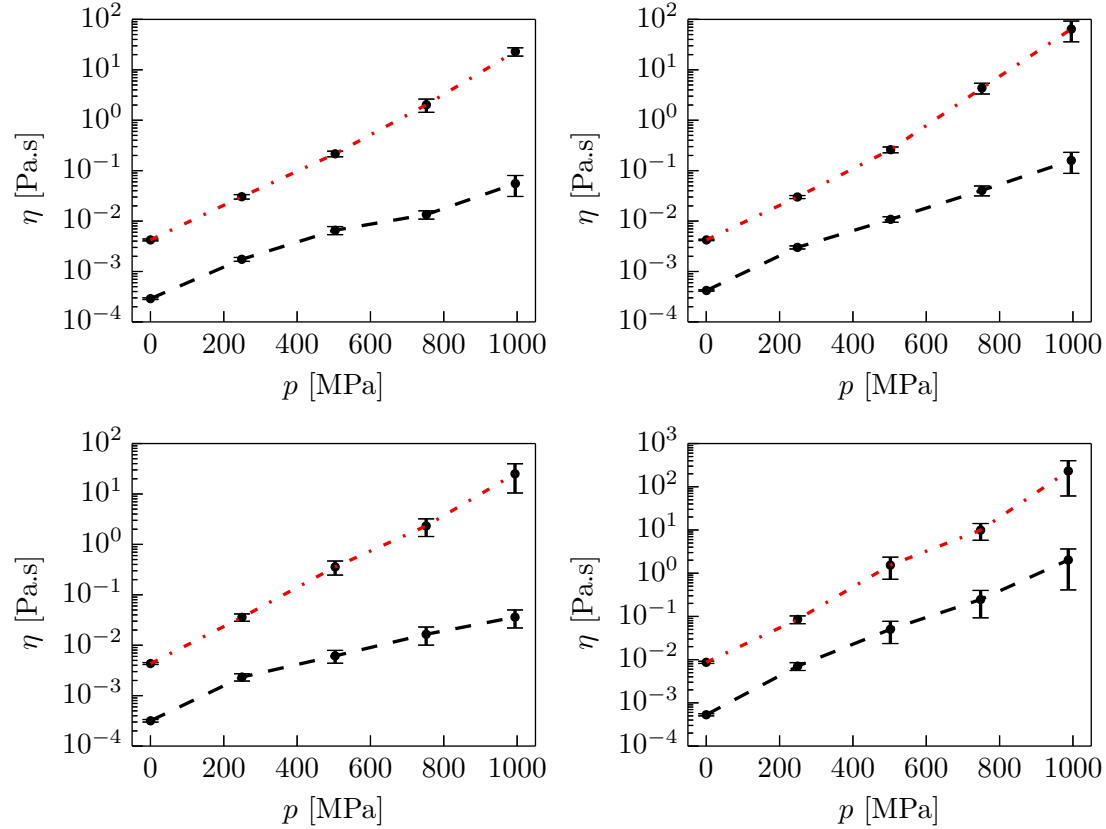


Figure 4.4: Pressure-dependent zero-shear and bulk viscosity for *n*-octane (top left), *i*-octane (top right), *n*-hexadecane (bottom left) and *i*-hexadecane (bottom right). The dash-dotted (red) lines represent the bulk, whereas and the dashed (black) lines the zero-shear viscosities. The error-bars correspond to the standard deviation calculated by taking the square root of the variance given by Eq. (4.6).

			total zero-shear viscosity			kinetic viscosity			bond viscosity			angle viscosity		
	$\langle p \rangle_{eq}$	τ_{run}	$\eta_{tot} \times 10^3$	$\sigma_{\eta_{tot}} \times 10^3$	τ_c	$\eta_{kin} \times 10^6$	$\sigma_{\eta_{kin}} \times 10^6$	τ_c	$\eta_{bond} \times 10^2$	$\sigma_{\eta_{bond}} \times 10^2$	τ_c	$\eta_{angl} \times 10^2$	$\sigma_{\eta_{angl}} \times 10^2$	τ_c
<i>n</i> -octane	0.01	60.5	0.289	0.011	23.7	17.215	0.596	18.1	0.246	0.011	30.0	0.613	0.027	30.0
	249.01	52.8	1.744	0.154	102.6	21.611	1.939	106.2	1.539	0.157	138.0	4.364	0.446	138.0
	503.76	46.8	6.579	1.201	389.8	26.697	4.717	365.4	3.773	0.689	390.2	11.943	2.180	390.2
	752.47	45.2	13.450	2.532	400.6	42.213	12.357	968.7	9.929	2.930	984.2	36.492	10.767	984.2
	995.13	44.3	55.437	24.681	2193.0	33.818	15.375	2287.0	24.181	11.064	2316.6	96.192	44.015	2316.6
<i>i</i> -octane	0.57	58.7	0.420	0.013	13.8	12.601	0.362	12.1	0.258	0.008	13.8	0.161	0.005	13.8
	248.62	51.9	3.007	0.209	62.7	14.670	0.998	60.1	1.525	0.106	62.7	1.022	0.071	62.7
	502.80	46.5	10.823	1.358	183.1	16.534	2.188	203.5	6.082	0.807	204.8	4.315	0.573	204.8
	751.83	44.7	40.605	9.010	550.8	27.140	6.531	647.8	20.918	5.042	650.0	14.398	3.471	650.0
	995.56	43.8	159.358	71.093	2178.0	50.200	22.274	2154.5	89.690	40.013	2178.0	74.147	33.079	2178.0
<i>n</i> -hexadecane	0.29	64.7	0.317	0.019	55.8	17.411	0.608	19.8	0.616	0.041	71.2	1.724	0.114	71.2
	249.64	54.7	2.335	0.388	378.3	19.359	3.191	371.5	5.000	0.833	379.2	16.171	2.693	379.2
	503.70	38.6	6.145	1.751	784.3	29.961	8.883	849.1	15.270	4.655	897.5	55.742	16.920	889.9
	751.88	46.8	16.489	6.461	1794.9	40.653	17.093	2066.8	27.344	11.500	2068.0	110.962	45.602	1974.5
	994.24	45.8	36.055	14.049	1738.7	38.184	22.165	3858.5	60.939	35.563	3900.0	277.649	162.030	3900.0
<i>i</i> -hexadecane	0.04	60.1	0.530	0.031	50.3	13.075	0.765	51.4	1.685	0.099	51.5	0.506	0.030	51.5
	249.29	49.4	7.066	1.457	525.4	14.995	2.025	225.3	21.323	4.239	488.4	6.837	1.405	522.2
	502.15	47.4	50.260	26.687	3344.0	35.644	18.882	3328.4	101.654	37.543	1617.8	33.472	12.538	1664.2
	748.24	45.6	246.023	153.200	4416.7	46.585	33.313	5824.7	726.581	527.345	6000.0	209.817	152.283	6000.0
	987.35	37.8	2023.334	1612.399	6000.0	47.778	37.980	5970.4	1711.770	1364.113	6000.0	538.479	429.115	6000.0

Table 4.4: Zero-shear viscosities as a function of pressure $\langle p \rangle_{eq}$ in MPa for all simulated molecular systems together with the square root of their variance in Pa.s and the (significant) correlation time τ_c in ps. Additionally to the total zero-shear viscosity η_{tot} , the partial contributions η_{kin} , η_{bond} and η_{angl} as well as the total simulated time τ_{run} in ns are also given. The partial viscosities result from autocorrelating only the kinetic, bond, angular, dihedral and long range force contributions of the total pressure tensor.

			total zero-shear viscosity			dihedral viscosity			long range viscosity			bulk viscosity		
	$\langle p \rangle_{eq}$	τ_{run}	$\eta_{tot} \times 10^3$	$\sigma_{\eta_{tot}} \times 10^3$	τ_c	$\eta_{dihed} \times 10^6$	$\sigma_{\eta_{dihed}} \times 10^6$	τ_c	$\eta_{long} \times 10^2$	$\sigma_{\eta_{long}} \times 10^2$	τ_c	$\eta_{bulk} \times 10^2$	$\sigma_{\eta_{bulk}} \times 10^2$	τ_c
<i>n</i> -octane	0.01	60.5	0.289	0.011	23.7	7.834	0.349	30.0	1.389	0.062	30.0	0.423	0.018	27.8
	249.01	52.8	1.744	0.154	102.6	29.654	2.902	126.4	9.384	0.960	138.0	3.039	0.311	138.0
	503.76	46.8	6.579	1.201	389.8	60.821	11.103	390.2	24.166	4.412	390.2	21.565	2.742	189.3
	752.47	45.2	13.450	2.532	400.6	103.261	18.670	369.6	73.152	21.584	984.2	202.850	59.425	970.2
	995.13	44.3	55.437	24.681	2193.0	219.532	91.195	1909.3	173.647	79.456	2316.6	2300.632	431.886	389.9
<i>i</i> -octane	0.57	58.7	0.420	0.013	13.8	3.208	0.098	13.8	0.625	0.019	13.8	0.423	0.013	13.7
	248.62	51.9	3.007	0.209	62.7	12.882	0.863	58.3	3.518	0.245	62.7	3.003	0.209	62.7
	502.80	46.5	10.823	1.358	183.1	35.589	4.351	173.7	14.381	1.909	204.8	26.047	3.439	202.6
	751.83	44.7	40.605	9.010	550.8	126.034	30.381	650.0	46.429	11.192	650.0	436.036	104.809	646.3
	995.56	43.8	159.358	71.093	2178.0	336.503	145.148	2036.1	216.965	96.793	2178.0	6422.901	2832.296	2128.0
<i>n</i> -hexadecane	0.29	64.7	0.317	0.019	55.8	5.657	0.199	20.0	3.887	0.258	71.2	0.433	0.019	30.8
	249.64	54.7	2.335	0.388	378.3	15.454	1.226	86.0	34.780	5.793	379.2	3.580	0.595	377.0
	503.70	38.6	6.145	1.751	784.3	26.479	3.463	165.2	118.264	35.855	887.8	35.710	11.089	931.4
	751.88	46.8	16.489	6.461	1794.9	73.637	21.887	1032.7	227.668	93.052	1952.9	232.190	88.932	1715.0
	994.24	45.8	36.055	14.049	1738.7	87.916	23.642	828.1	544.837	317.956	3900.0	2509.633	1464.542	3899.8
<i>i</i> -hexadecane	0.04	60.1	0.530	0.031	50.3	11.260	0.659	51.5	3.472	0.203	51.5	0.867	0.051	51.5
	249.29	49.4	7.066	1.457	525.4	68.130	11.685	363.5	44.510	8.867	490.3	8.536	1.743	515.5
	502.15	47.4	50.260	26.687	3344.0	286.127	101.381	1489.1	209.542	76.810	1593.7	153.654	81.273	3318.5
	748.24	45.6	246.023	153.200	4416.7	2178.903	1581.426	6000.0	1463.519	1062.208	6000.0	994.076	416.396	1998.5
	987.35	37.8	2023.334	1612.399	6000.0	5991.433	4774.584	6000.0	2926.778	2332.355	6000.0	23108.684	16987.395	5105.6

Table 4.5: Continuation of Tab. 4.4 completed with the partial viscosities η_{dihed} and η_{long} as well as the bulk viscosity η_{bulk} .

An example of the result of the viscosity integrals (time integral of the average of the autocorrelation functions of the off-diagonal elements of the pressure tensor) as a function of the upper integration boundary τ_c is given in Fig. 4.6. The graphs of the integrals of all other simulated MD systems are provided in the Appendix C in Figs. C.1-C.19 for zero-shear viscosity and Figs. C.20-C.24 for bulk viscosity.

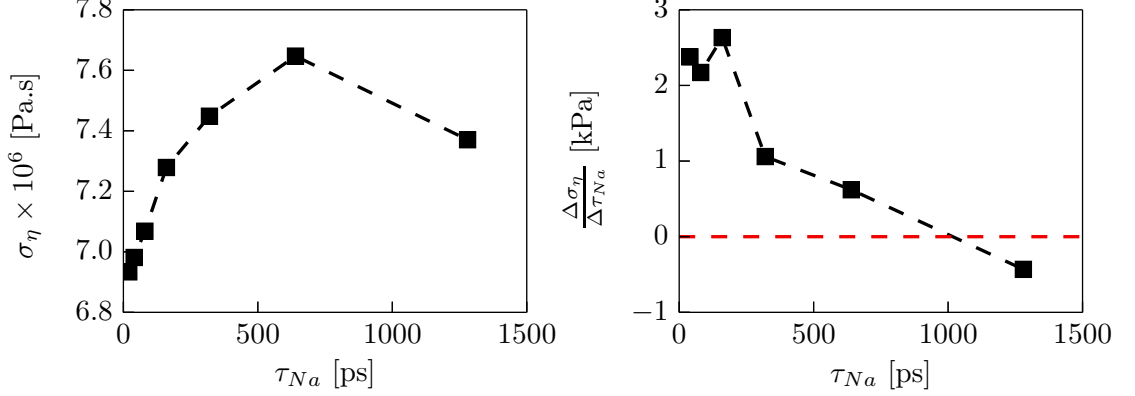


Figure 4.5: The standard deviation σ_η of the zero-shear viscosity (left) and the finite differences $\Delta\sigma_\eta/\Delta\tau_{Na}$ (right) in case of *n*-octane at 100 kPa as a function of averaging block size τ_{Na} .

An example for the calculation of the large-block limit of the shear viscosity's standard deviation is given in Fig. 4.5. *n*-Octane at a pressure of 100 kPa was chosen for this example since it was the closest of all systems to converge towards a constant value in the large block limit.

A comparison of the simulated zero-shear viscosities with experimental data reported in literature is given in Tab. 4.6 and visualized in Fig. 4.7. In Tab. 4.6, the reported parameters for pressure-viscosity relations – the pressure-viscosity-index z , see Eq. (2.37) and the pressure-viscosity-coefficient α recall Eq. (2.34) and (2.30) – were calculated by using viscosity data within the entire range of available pressures. α_0 , see Eqs. (2.32) and (2.30), was calculated by using the viscosity at 0.1 MPa as reference ($p = 0$) and the viscosity at 250 MPa as second data point to estimate the derivative in the low pressure region as a ratio of finite differences.

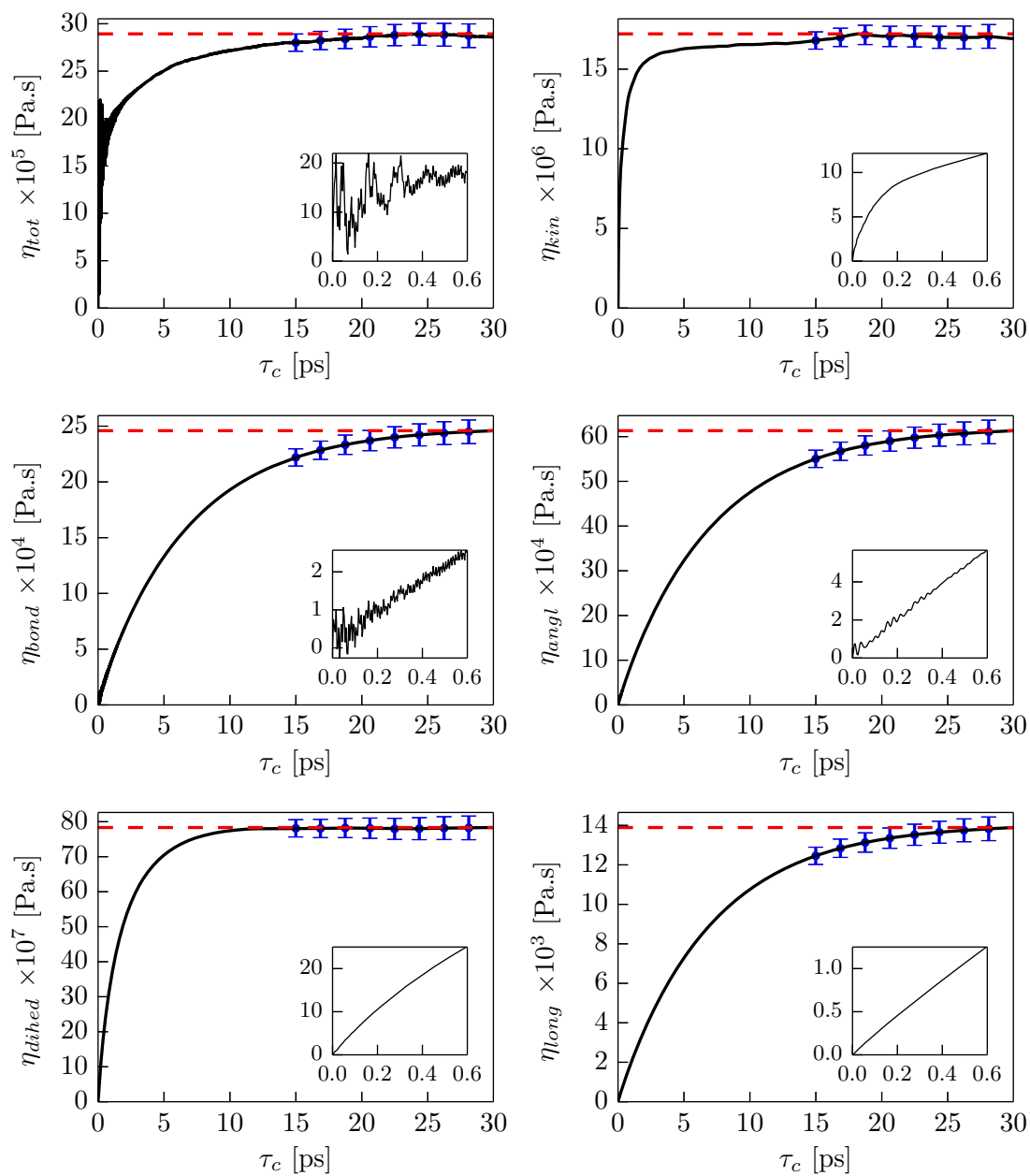


Figure 4.6: Contributions to zero-shear viscosity in case of *i*-octane at 100 kPa and 348.15 K. The small insets show the first 0.6 ps in higher resolution (the units of the scales are the same as in the large graphs). The error bars represent the standard deviation of the viscosities calculated by the square root of Eq. (4.6). The dashed (red) lines correspond to the maximum value of the viscosities.

System	$\langle p \rangle_{eq}$	η	σ_η	η^{lit}	z	z^{lit}	α_0	α_0^{lit}	α	α^{lit}	Ref.
	[MPa]	[mPa.s]					[GPa ⁻¹]		[GPa ⁻¹]		
<i>n</i> -octane	0.01	0.011	0.289	0.304							[47]
	249.01	1.744	0.154	1.555							[47]
	503.76	6.579	1.201	4.27	0.291	0.248	7.21	6.44	5.46	6.98	[47]
	752.47	13.450	2.532	—							-
	995.13	55.437	24.681	—							-
<i>i</i> -octane	0.57	0.420	0.013	0.281							[48]
	248.62	3.007	0.209	1.82 ^a							[48]
	502.80	10.823	1.358	5.628	0.315	0.281	7.93	7.46	5.82	8.16	[48]
	751.83	40.605	9.010	—							-
	995.56	159.358	71.093	—							-
<i>n</i> -hexadecane	0.29	0.317	0.019	0.363 ^b							[49–51]
	249.64	2.335	0.388	—							-
	503.70	6.145	1.751	—	0.280	-	8.00	-	5.63	-	-
	751.88	16.489	6.461	—							-
	994.24	36.055	14.049	—							-
<i>i</i> -hexadecane	0.04	0.530	0.031	0.357 ^c							[52]
	249.29	7.066	1.457	4.0 ^d							[52]
	502.15	50.260	26.687	—	0.389	0.369	10.40	9.70	6.82	13.50	-
	748.24	246.023	153.200	—							-
	987.35	2023.334	1612.399	—							-

Table 4.6: Comparison of the calculated zero-shear viscosities η with experimental data η^{lit} reported in literature. In addition, the square root of the variance σ_η , the fitted pressure dependence to Roelands' relation (pressure-viscosity-index z) and Barus' relation (pressure-viscosity-coefficient α or α_0) are also given and compared.

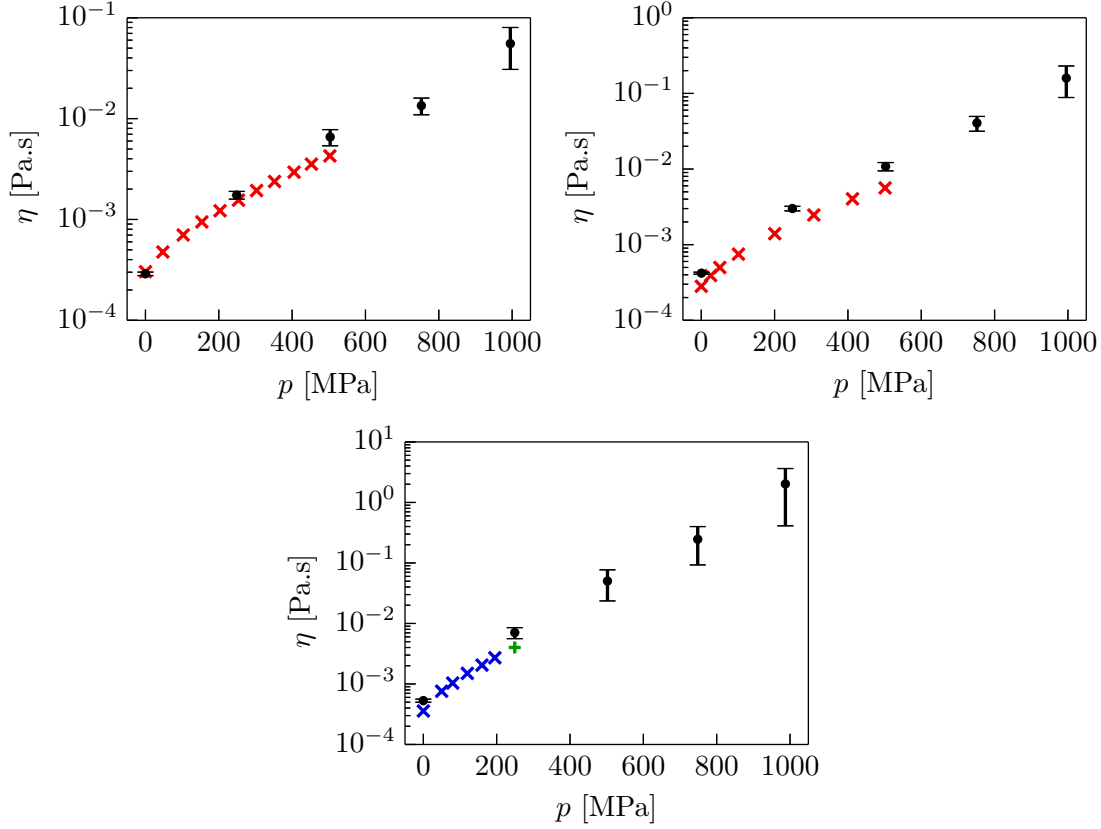


Figure 4.7: Comparison of calculated zero-shear viscosities with experimentally obtained data for *n*-octane (top left), *i*-octane (top right) and *i*-hexadecane (bottom middle). Crosses correspond to experimental data taken from Ref. [47] for *n*-octane and from Ref. [48] for *i*-octane, pluses to temperature extrapolated values, whereas stars correspond to temperature and pressure extrapolated values from Ref. [52] for *i*-hexadecane.

No high pressure viscosity data at a temperature of 473.15 K is available for the hexadecane isomers in literature. However, for *n*-hexadecane measurement results at ambient pressure and 473.15 K as well as for *i*-hexadecane high pressure measurements in the range of 0.1 to 195 MPa at 453.15 K are available in literature. In order to compare the measured data to the simulation results, *i*-hexadecane the viscosities reported were extrapolated to the required temperature. This was achieved by means of a nonlinear least-squares fit

$$\eta(T) \simeq c_1 (T - c_2)^{c_3} \quad , \quad (4.12)$$

with the parameters c_{1-3} . In addition to these temperature extrapolation, a pressure extrapolation to 250 MPa at 473.15 K was carried out by fitting the logarithm of the normalized viscosities to a simple power law, namely

$$\ln(\eta(p)) \simeq d_1 \left[\ln \left(\frac{\eta(p)}{\eta(p = 0.1 \text{ MPa})} \right) \right]^{d_2} \quad , \quad (4.13)$$

^aObtained by linear interpolation of logarithmized viscosities.

^bAverage of the values found in the given references.

^cTemperature extrapolation applied according to Eq. (4.12).

^dTemperature and pressure extrapolation according to Eqs. (4.12) and (4.13).

by using the fitting parameters d_1 and d_2 .

No experimental data regarding the bulk viscosity of the studied liquids at or near the state points considered in this work was found.

In Fig. 4.8, the zero-shear viscosity is plotted in relation with three different pressure-viscosity relations. In order to determine the pressure-viscosity-index z , used in Roelands' relation, for each MD system the logarithm of Roelands' relation recall Eq. (2.37) was fitted to the logarithm of viscosities by means of a nonlinear least-squares fit. The pressure-viscosity-coefficient α from Barus' relation, was calculated in two different manners given in Eqs. (2.32) and (2.34). The numerical integration in the last equation was carried out by using the trapezoidal rule for non-equidistant data sets.

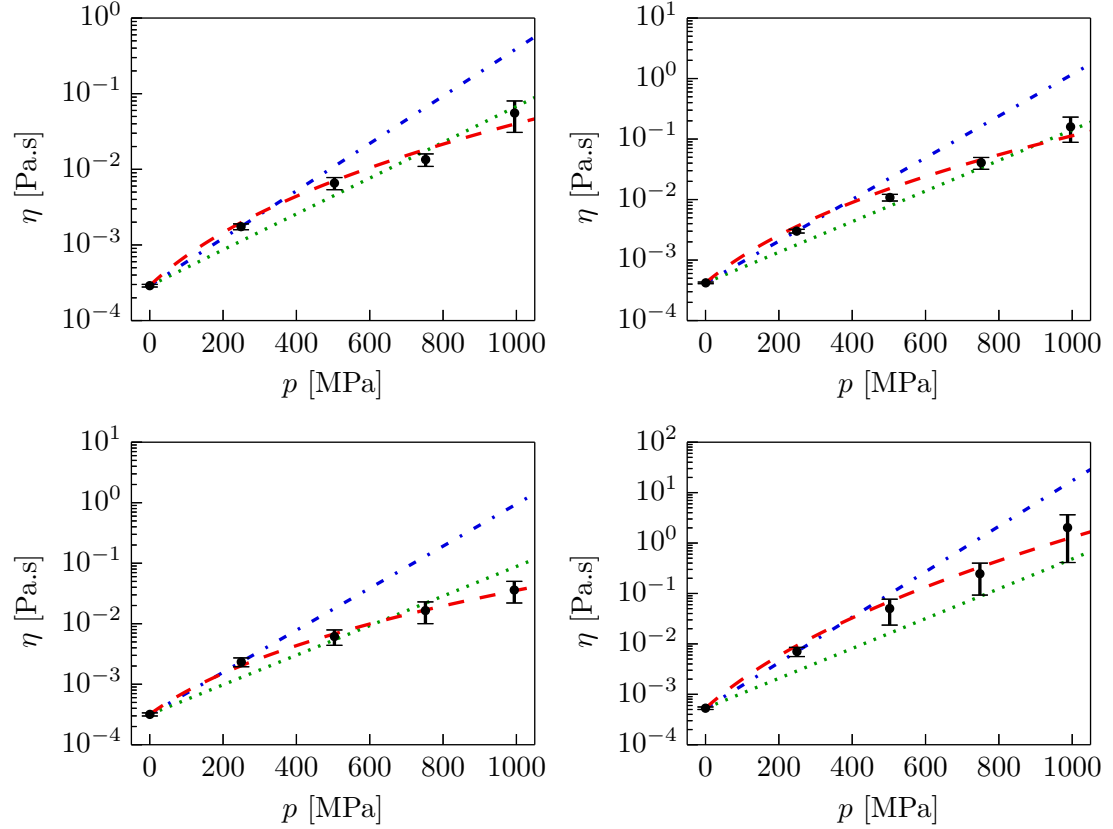


Figure 4.8: Calculated pressure-dependent zero-shear viscosities for *n*-octane (top left), *i*-octane (top right), *n*-hexadecane (bottom left) and *i*-hexadecane (bottom right). The dashed (red) line corresponds to Roelands' relation in Eq. (2.37), the dash-dotted (blue) line to Barus' relation in Eq. (2.30) with α calculated according to Eq. (2.32) and the dotted (green) line corresponds to Barus' relation with α calculated according to Eq. (2.34), respectively.

Fig. 4.9 depicts the viscosities calculated from separate contributions to the overall pressure tensor as provided by Eq. (2.27) and further discussed on page 28.

In general, the EMD simulations coupled with the Green-Kubo formula for calculating the zero-shear viscosity, yielded results that compare well to the experimental data available from literature, see Tab. 4.6 and Fig. 4.7. However, the simulation results point towards a systematical error, e.g., a general overestimation of viscosities obtained for iso-alkanes both at ambient and high pressure. A general statement about the calculated results for normal alkanes can not be given, due to the lack of high pressure experimental data for *n*-hexadecane at the considered

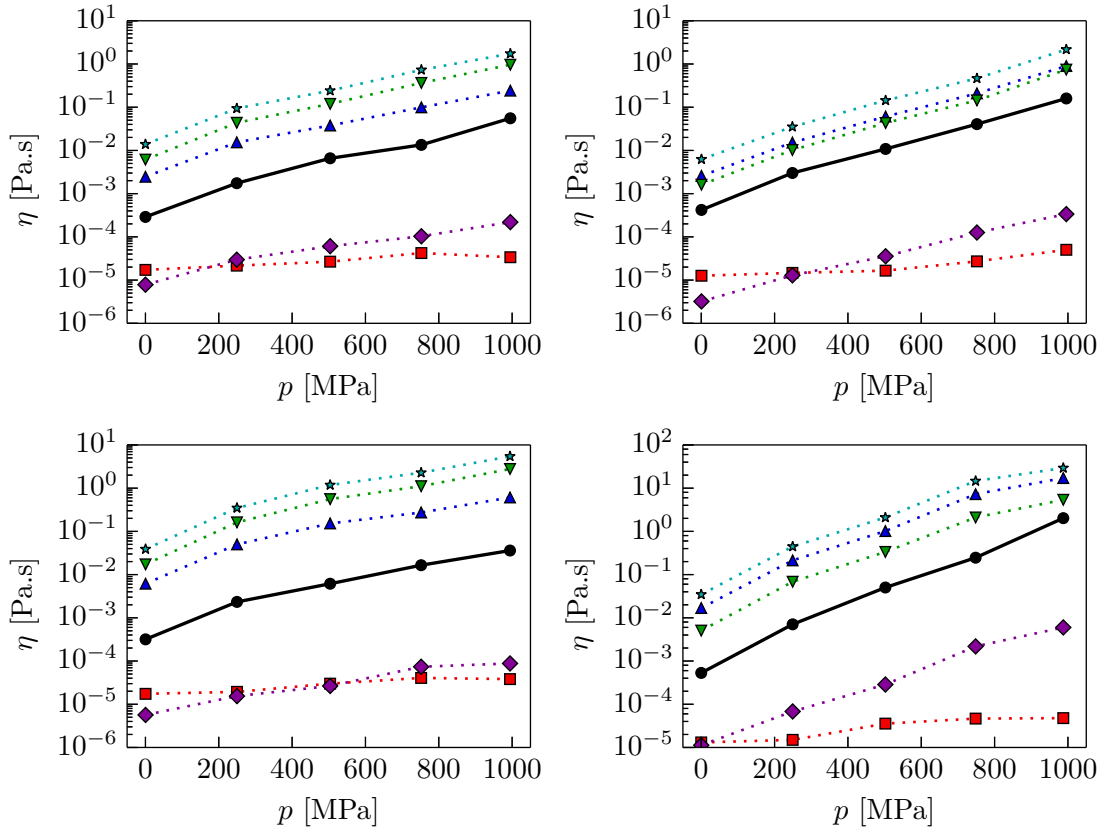


Figure 4.9: Calculated contributions to the pressure-dependent zero-shear viscosities (\bullet) for *n*-octane (top left), *i*-octane (top right), *n*-hexadecane (bottom left) and *i*-hexadecane (bottom right). Additionally, the partial contributions η_{kin} (\blacksquare), η_{bond} (\blacktriangle), η_{angl} (\blacktriangledown), η_{dihed} (\blacklozenge) and η_{long} (\star) are also given for treating solely the kinetic, bond, angular, dihedral and long-range force contributions. Error bars are omitted for a better visualization.

temperature. Nevertheless, it seems that the agreement between experimental and simulation results is better for normal- than for iso-alkanes. This observed deviation between simulation and experiment can be caused by a not fully optimized force field for iso-alkanes in combination with its modifications applied in this work, refer to section 3.2 for further details. The force field was fitted by Siu et al. in [41] to correctly describe the transport properties of *n*-alkanes and alkenes, but was not explicitly designed for use with branched alkanes. Furthermore, the high statistical uncertainty of the simulation results and the possibly significant integral cutoff error (especially in the case of *i*-hexadecane) for high pressures yield further deviations. These high standard deviations at high pressures have two main reasons:

1. nearly exponential increase of rotational correlation times with pressure and
2. reduced computational efficiency for MD systems with high density caused by application of high pressure.

1. is backed up by the analysis of the rotational correlation times which strongly increase as pressure increases, see Figs. 4.11 and 4.12. This directly translates to an increasing number of MD timesteps τ_c required to calculate the viscosity according to the algorithm used for this work, recall page 28. An increasing τ_c then leads to a higher variance of the viscosities obtained from

the MD simulations with a fixed total simulated time τ_{run} , see Eq. (4.6). The total simulated time τ_{run} necessary to achieve a certain relative precision in the calculated viscosity can be estimated based on the rotational correlation time τ^{rot} of the considered molecule and Eq. (4.6) as follows

$$\frac{\sigma_{\eta}}{\eta} = 2\sqrt{\frac{2\tau^{rot}}{\tau_{run}}} \quad (4.14)$$

The decrease in computational efficiency mentioned in 2. results from the increase in the total number of pairwise force evaluations that need to be done every timestep due to the high density, i.e., more atoms are present within the force cutoff distance at higher pressures. Since all simulations were started and stopped at the same time, the only exceptions being the *n*-hexadecane at 500 MPa and *i*-hexadecane at 1 GPa where the runs were aborted early due to run errors, this can be seen directly in the decrease of τ_{run} in Tab. 4.5 with increasing pressure.

The observation about the absolute viscosity values does not fully transfer to the values obtained from the fits to the pressure-viscosity relations. All molecules, for which a comparison with literature is possible, showed good agreement in the parameters z and α_0 , while α seems to differ rather strongly from the values given in literature. In general, it was found that the simulated pressure dependence of the shear viscosity follows Roelands' pressure-viscosity relation, see Fig. 4.8. Using Barus' relation with a constant pressure-viscosity coefficient can result in significant differences at high pressures when using α_0 as defined in Eq. (2.32), or a just moderate description of the pressure dependency via α as defined by Eq. (2.34).

The calculation of the large-block limit of the standard deviation of the viscosity results, as described in section 4.2, did not yield the desired results. Even in the best case of all simulated MD systems, *n*-octane at 100 kPa, convergence of the standard deviation to a limiting value could not be observed in Fig.4.5. The finite differences on the right plot in Fig. 4.5 should be converging towards zero in a exponential or power law manner to be able to determine the large-block limit of the standard deviation. This means that it is hardly possible for all considered MD systems to estimate the large-block limit for two reasons. Firstly, the estimate of the standard deviation itself is subject to statistical errors, at least at large block sizes. Secondly, an extrapolation of the standard deviations to their limiting values was found to be numerically unstable due to the limited dataset available).

The the partial contributions to the pressure-dependent zero-shear viscosity visualized in Fig. 4.9, show that long range interactions seem to be dominant in all simulated MD systems. However, a noticeable difference in the relative bond and angular contributions between normal- and iso-alkenes is found. While in the *n*-alkanes, the angular contribution significantly dominates over the bond contribution, the opposite seems to be true for *i*-hexadecane. In the case of the short chained *i*-octane, both contributions are almost identical in magnitude. The remaining contributions, resulting from the kinetic and the dihedral term in the pressure tensor, are orders of magnitude smaller than the others. All contributions except the kinetic term, show similar dependence on pressure when compared to the total viscosity. The kinetic term seems to be largely independent of pressure.

A comparison between the rotational correlation time and the zero-shear viscosity shows a strong correlation between these quantities, see Fig. 4.13. This suggests a common mechanism that influences both pressure dependencies namely of the rotational correlation time as well as the shear viscosity of a liquid. If a direct physical connection and mathematical relation between these two quantities could be formulated, the calculation of high pressure viscosities could be replaced by evaluating the rotational correlation time only, which can be determined with much

higher statistical significance and hence less computational effort than would be necessary to calculate the zero-shear viscosity directly.

Bulk viscosity, a property of liquids where measurement results can be hardly found in the available literature, was also computed. The obtained results show, that the bulk viscosity tends to increase even faster than exponential with pressure, see Fig. 4.4. This strong increase and the fact that the bulk viscosity is already at ambient pressure an order of magnitude higher than the zero-shear viscosity, leads to a huge difference of around three orders of magnitude for *n*-hexadecane at 1 GPa. This leads to the question of whether the common approximation that the bulk viscosity of a fluid in a tribological contact can be neglected, is indeed applicable.

4.3 Rotational Correlation Time

The calculation of the rotational correlation times τ^{rot} of molecules can be performed by auto-correlating normalized intramolecular vectors that are chosen to represent a molecules orientation [19]. To the resulting autocorrelation function

$$C^{sim}(t) \simeq \mathcal{A} e^{t/\tau_1^{rot}} + (1 - \mathcal{A}) e^{t/\tau_2^{rot}} , \quad (4.15)$$

a superposition of two exponential functions can then be fitted by means of nonlinear least squares fitting. The fitting parameters \mathcal{A} , τ_1^{rot} and τ_2^{rot} are so obtained. The intramolecular vectors considered within this work are illustrated in Fig. 4.10. Vector A was chosen with the intention to best coincide with the direction of the minimum moment of inertia of each molecule. Vector B was chosen to be as orthogonal as possible to vector A.

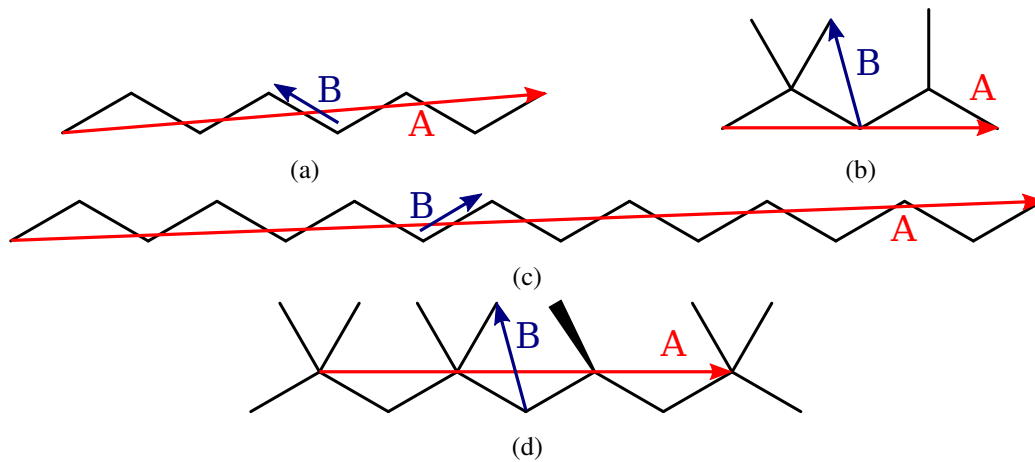


Figure 4.10: The intramolecular vectors used for calculating the rotational correlation times for (a) *n*-octane, (b) *i*-octane, (c) *n*-hexadecane and (d) *i*-hexadecane. The long (red) vectors will be referred to as “vector A”, the short (blue) vectors will be referred to as “vector B”.

The calculated rotational correlation times of the simulated alkanes are given in Tab. 4.7 as well as in Figs. 4.11 and 4.12 for a better visualization.

System	$\langle p \rangle_{eq}$	vector A			vector B		
		τ_1^{rot} [ps]	τ_2^{rot} [ps]	\mathcal{A}	τ_1^{rot} [ps]	τ_2^{rot} [ps]	\mathcal{A}
<i>n</i> -octane	0.01	15.0	2.26	0.95	14.7	2.22	0.62
	249.01	69.0	2.91	0.95	67.9	5.50	0.61
	503.76	195.1	7.06	0.95	192.0	10.68	0.61
	752.47	492.1	15.85	0.95	487.5	18.82	0.60
	995.13	1158.4	37.46	0.94	1147.1	32.13	0.60
<i>i</i> -octane	0.57	6.9	1.88	0.85	6.4	1.88	0.75
	248.62	31.4	4.27	0.81	28.9	5.09	0.68
	502.80	102.5	12.07	0.77	94.1	13.63	0.61
	751.83	325.1	32.46	0.74	307.3	36.15	0.56
	995.56	1090.0	88.83	0.73	1021.4	91.39	0.53
<i>n</i> -hexadecane	0.29	35.6	3.91	0.95	34.3	2.63	0.49
	249.64	189.6	6.97	0.95	185.1	5.08	0.48
	503.70	469.0	10.42	0.96	458.6	9.17	0.48
	751.88	1034.7	90.54	0.93	994.9	14.40	0.48
	994.24	1950.7	74.48	0.95	1887.0	20.20	0.48
<i>i</i> -hexadecane	0.04	25.7	4.87	0.92	19.4	5.02	0.48
	249.29	262.8	40.35	0.89	198.7	28.92	0.37
	502.15	1672.9	154.25	0.91	1386.1	124.66	0.32
	748.24	10365.8	658.12	0.93	9594.9	505.34	0.30
	987.35	62112.3	4532.03	0.93	32540.5	1616.28	0.39

Table 4.7: Rotational correlation times, see Eq. (4.15), of all molecular systems for the intramolecular vectors A and B introduced in Fig. 4.10.

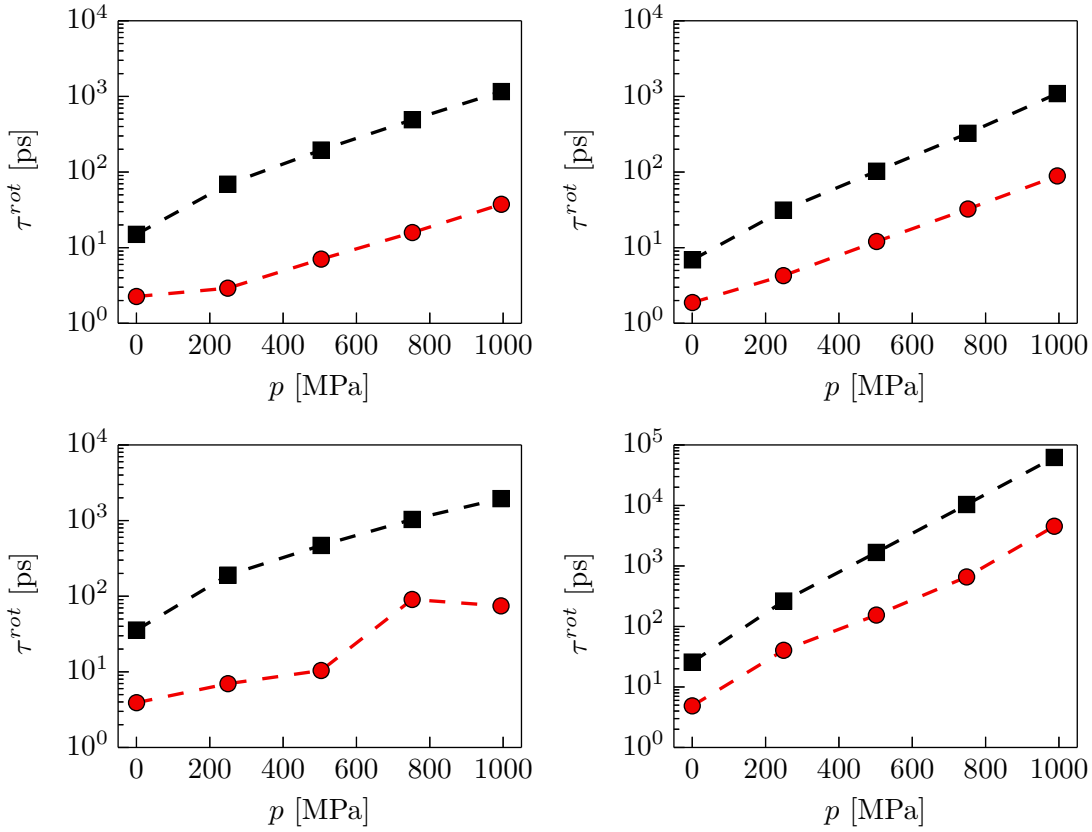


Figure 4.11: The pressure-dependent rotational relaxation time τ_1^{rot} (■) and τ_2^{rot} (●) calculated using vector A (as specified in Fig. 4.10) for *n*-octane (top left), *i*-octane (top right), *n*-hexadecane (bottom left) and *i*-hexadecane (bottom right).

In Fig. 4.13, the pressure dependency of the rotational correlation time is compared to the pressure dependency of the shear viscosity.

The chosen model for $C^{sim}(t)$, recall Eq. (4.15), takes the observed short term drop of $C^{sim}(t)$ into account and hence fits well to the calculated correlation functions. The dependence of the fitting results on the choice of the vector is low, as can be seen in Fig. 4.14. The most significant difference in the results for the different vectors A and B is a different relative contribution of the two exponential functions represented by the fitting parameters \mathcal{A} and $1 - \mathcal{A}$. The absolute value of the short and fast relaxation times τ_1^{rot} and τ_2^{rot} depend only weakly on the choice of vectors used for the computing of the rotational autocorrelation as can be observed from the slopes of graphs in Fig. 4.14 or directly from Tab. 4.7.

In general, it is seen that the longest rotational correlation time (τ_1^{rot}) for the branched molecules increases fairly exponential with the applied pressure. For the linear alkanes, a slower than purely exponential increase is found. Among the possible explanations for these differences could be the different overall shape of molecules, see the 3D structure of the branched alkanes in see Fig. 4.15. Another reason of differences could be the differences in the flexibility of molecules. It could be caused by the steric hindrance of the methyl substituents on the main C-chain of the iso-alkanes. However, to find the exact mechanism, further simulations and analysis of the data is necessary.

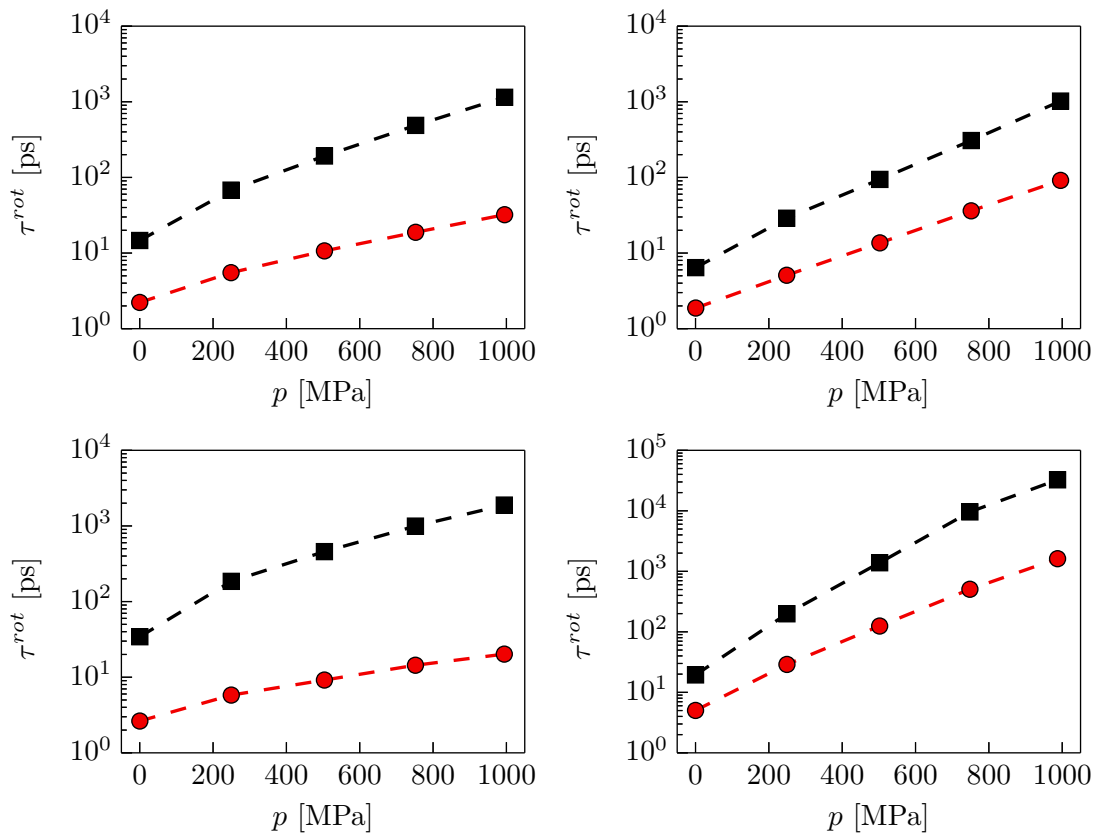


Figure 4.12: The same as Fig. 4.11 for vector B.

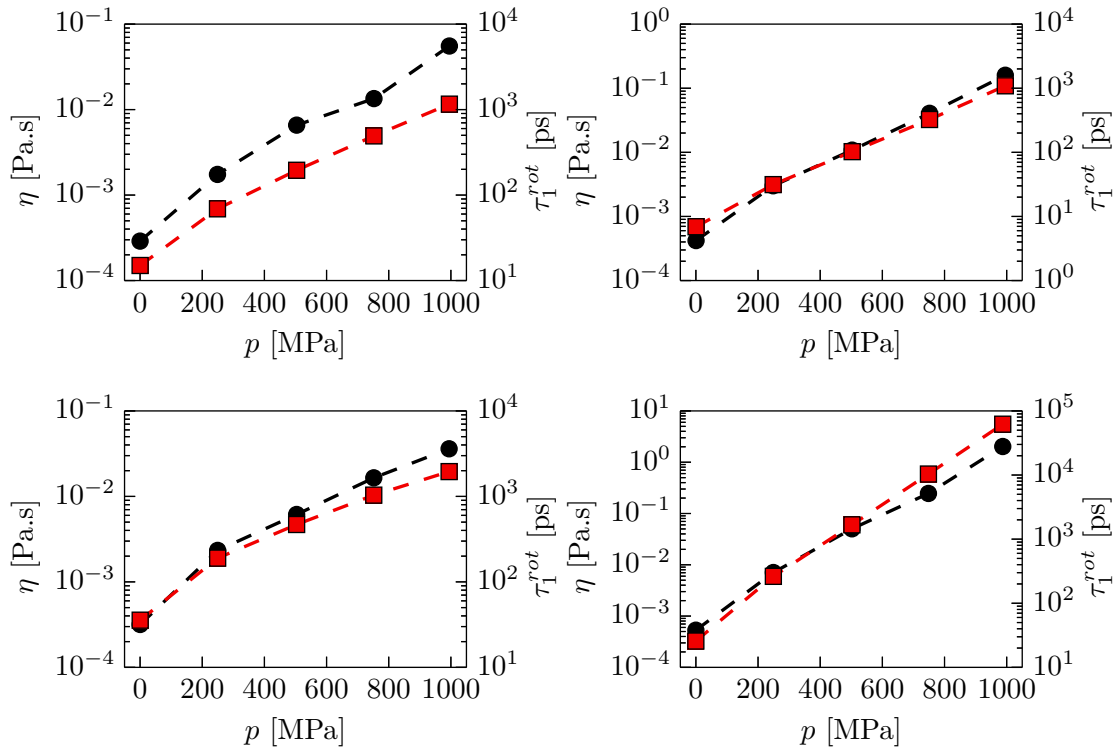


Figure 4.13: A comparison between the pressure-dependent zero-shear viscosities η (●) and the rotational correlation time τ_1^{rot} (■) for *n*-octane (top left), *i*-octane (top right), *n*-hexadecane (bottom left) and *i*-hexadecane (bottom right).

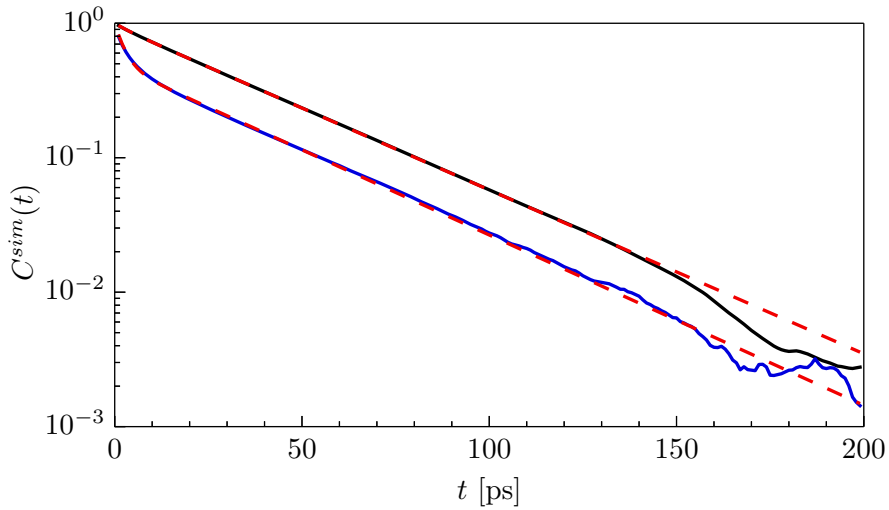


Figure 4.14: Rotational autocorrelation functions $C^{sim}(t)$ obtained using the normalized vector A (red) and B (blue) for *n*-hexadecane at 100 kPa. The solid lines correspond to the calculated autocorrelation function, while the dashed lines to the fitted one, see Eq. (4.15).

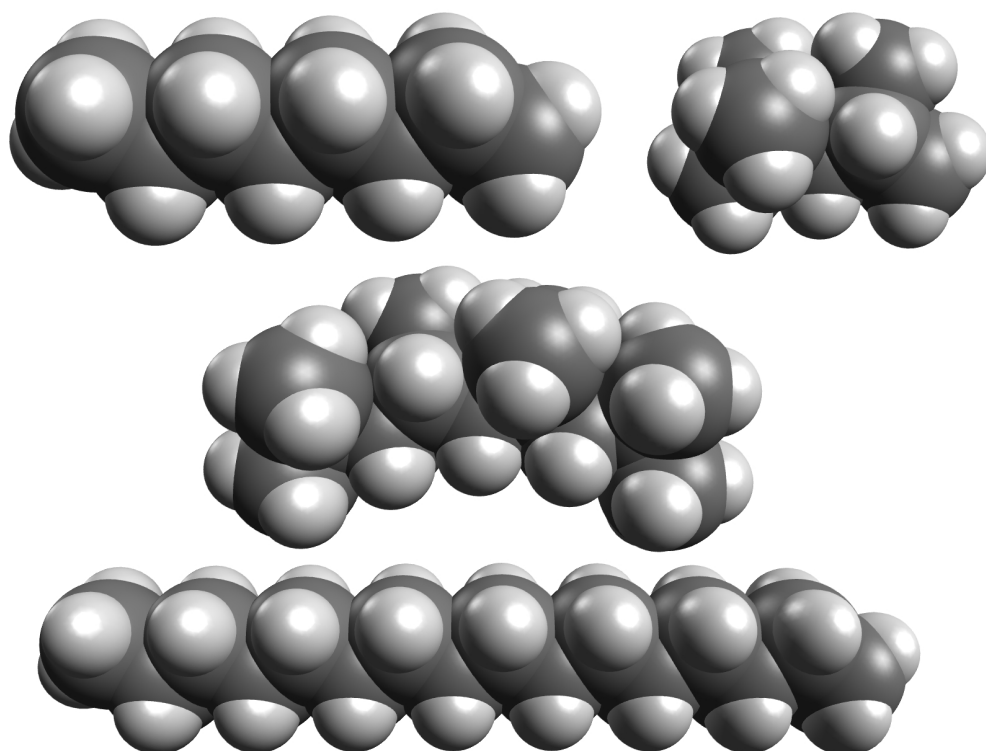


Figure 4.15: 3D renderings of *n*-octane (top left), *i*-octane (top right), *i*-hexadecane (middle) and *n*-hexadecane (bottom). The radii of the spheres correspond to the van der Waals radii of atoms.

Summary and Conclusion

The following molecular systems were simulated by means of equilibrium molecular dynamics for this work:

- 1024 molecules of *n*-octane at 348.15 K,
- 1024 molecules of 2,2,4-trimethylpentane (*i*-octane) at 348.15 K,
- 512 molecules of *n*-hexadecane at 473.15 K and
- 512 molecules of (6S)-2,2,4,4,6,8,8-heptamethylnonane (*i*-hexadecane) at 473.15 K.

The temperatures were selected to ensure that, at least in accordance with the experiments, the systems stay in the liquid phase at all the pressure chosen, namely 0.1, 250, 500, 750 and 1000 MPa.

The molecular dynamics (MD) simulations were set up using a modified version of the OPLS-aa force field, periodic boundary conditions, a PPPM long-range electrostatic solver, a rRESPA multiple timescale integrator and a Nosé-Hoover chain thermostat. An equilibration period of 4 ns was taken before any molecular dynamics data was considered for further analysis. A test for successful equilibration of all systems was performed and measured how close they are to their equilibrium. This was done by calculating the Hellinger metric of the density distribution functions of the off-diagonal pressure tensor elements relative to an “equilibrium” distribution function obtained from the end of the MD trajectories. Furthermore, the convergence of block averages to their expected equilibrium value was also studied. It was found that all systems except *i*-hexadecane at 500, 750 and 1000 MPa were sufficiently close to equilibrium after 4 ns equilibration time.

The structural data obtained from the production runs were used to calculate the rotational relaxation times of molecules by fitting the normalized autocorrelation of intramolecular positions to an exponentially decaying model. These results were used to estimate the maximum significant correlation time for the Green-Kubo viscosity formula by providing a characteristic molecular timescale.

The Green-Kubo zero-shear and bulk viscosity calculations were carried out by computing time integrals over block averages of correlation functions for various pressure tensor elements. With these block averages, the uncertainty of the obtained viscosities can also be estimated by extrapolation to the large-block limit. It was found, however, that this extrapolation is not accurate enough given the limited size of the datasets obtained within this work. Therefore, an

estimation of the variance in the viscosity results based on the assumption of a Gaussian process as proposed in literature was used instead.

In order to provide insights into the “origin” of viscosity, partial contributions (kinetic, bond, angle, dihedral and long range forces) to the overall pressure tensor were considered and for these resulting viscosities were analyzed separately.

It was found that by applying the Green-Kubo viscosity formula to molecular systems at various pressures provides valuable data for the investigation of the rheological properties of alkanes. MD results obtained for linear alkanes are in good agreement with experimental measurements, while the viscosities of the branched alkanes were systematically overestimated by the force field applied in this work. Furthermore, for molecular systems with long rotational correlation times, a high computational effort is necessary to provide accurate viscosity data.

For the systems investigated here it was shown that

- the pressure-viscosity relation formulated by Roelands describes the pressure-dependent zero-shear viscosity better than the classical Barus relation;
- the pressure-dependent rotational correlation times correlate strongly with the calculated viscosities;
- different partial contributions to the viscosity are dominant for normal and iso alkanes;
- the bulk viscosity increases even stronger with increasing pressure than the zero-shear viscosity and it is also significantly greater in magnitude at ambient pressure.

CHAPTER 6

Outlook

The molecular dynamics (MD) results generated in this thesis will be subject of a more in-depth analysis of the relation between the chemical structure of molecules and their high-pressure rheological properties. More information about structural and dynamical properties of the investigated fluids can be obtained by analyzing the generated MD data in more detail. Further analysis could include, among others, the determination of characteristic trans-gauche transition frequencies, characterizations of the dynamics of intramolecular angles, bond lengths and so on. Additional attempts could be made to include and test the free-volume formulations of the pressure-viscosity relations for their applicability.

Furthermore, the experience gained in the field of molecular dynamics simulations of alkanes could be helpful for extending the simulations to non-equilibrium MD ones which can provide the shear rate dependence of viscosity under high pressure.

This work could also serve as a benchmark to compare the computational efficiency of viscosity determination by pure MD to hybrid methods such as a coupled Monte Carlo - MD (MCMD) approach. MCMD simulations could have a potential advantage over classical MD by offering a faster way of creating statistically independent systems.

LAMMPS Script

In the following, an example script that was used for MD data production with the *LAMMPS* program is given.

```
# Production run for 100kPa n-octane

# Control variables

variable      T equal 348.15      # temperature
variable      dt equal 0.004      # timestep

# General settings

units          metal
atom_style     full
boundary       p p p

pair_style     lj/cut/coul/long 13.0
bond_style     harmonic
angle_style    harmonic
dihedral_style opls
kspace_style   ppm 1.0e-5

special_bonds  lj/coul 0.0 0.0 0.5
pair_modify    shift no mix geometric tail yes

neighbor       2.5 bin
neigh_modify   delay 4

timestep       ${dt}
run_style      respa 4 2 2 2 inner 2 4.5 6.0 middle 3 8.0 10. &
               outer 4

# Read equilibrated system data
```

```

read_restart    n-oct-100kPa.init

reset_timestep 0

# Compute the required contributions to the pressure tensor

compute        pkin    all pressure thermo_temp ke
compute        pbnd    all pressure thermo_temp bond
compute        pangl   all pressure thermo_temp angle
compute        pdih    all pressure thermo_temp dihedral

# Define the simulation output

thermo_style    custom  step pxx pyy pzz pxy pxz pyz &
                etotal pe &
                c_pkin[1] c_pkin[2] c_pkin[3] &
                c_pkin[4] c_pkin[5] c_pkin[6] &
                c_pbnd[1] c_pbnd[2] c_pbnd[3] &
                c_pbnd[4] c_pbnd[5] c_pbnd[6] &
                c_pangl[1] c_pangl[2] c_pangl[3] &
                c_pangl[4] c_pangl[5] c_pangl[6] &
                c_pdih[1] c_pdih[2] c_pdih[3] &
                c_pdih[4] c_pdih[5] c_pdih[6]

thermo_modify   line one format float %.15e
thermo          1

variable        pres equal press
variable        tem  equal temp
variable        kine equal ke
variable        pote equal pe
variable        e    equal etotal
variable        van  equal evdwl
variable        k    equal elong
variable        c    equal ecoul
variable        bnd  equal ebond
variable        angl equal eangle
variable        dih  equal edihed

variable        t1   equal cpuremain/(3600.*24.)
variable        cp   equal cpu
variable        tsps equal spcpu

fix             out1 all ave/time 1 20 20 v_pres v_tem v_kine &
                v_pote v_e f_1 v_van v_c v_k v_bnd v_angl &
                v_dih file PTEdata.out

fix             out2 all ave/time 1 1 5000 v_cp v_tsps v_t1 &
                file CPUdata.out

```

```
dump          1 all custom 250 dump.out id mol type xu yu zu

# Perform NVT time integration

fix          1 all nvt temp $T $T 0.1 tchain 4

restart      5000 a.res b.res

restart      250000 out-*.res

run          20000000
```

For an easy access, important simulation parameters such as the temperature and the timestep are defined at the beginning of the script.

In the “General Settings” section, the overall simulation setup is defined, e.g., the *LAMMPS*-internal unit system is defined and periodic boundary conditions are applied to all three dimensions of the simulation box. Also, parameters for the force field are defined here via the manner in which bond, angle, dihedral and long-range interactions are calculated. Furthermore, the number of timesteps after which building neighbor lists are built as well as settings for the time integration algorithm can be also entered here.

The “compute” statements in the script store the partial results for the pressure tensor in variables which can then be written to a file with the “thermo_style” command.

At the end of the script, the first two “fix” commands are used for averaging certain quantities and printing the results to ASCII-files for monitoring the progress of the simulations. The last “fix” command specifies the parameters for the Nosé-Hoover chain thermostat, while the “run” command is used to start the simulations for 20.000.000 timesteps.

Hellinger Metric and Departure from Equilibrium

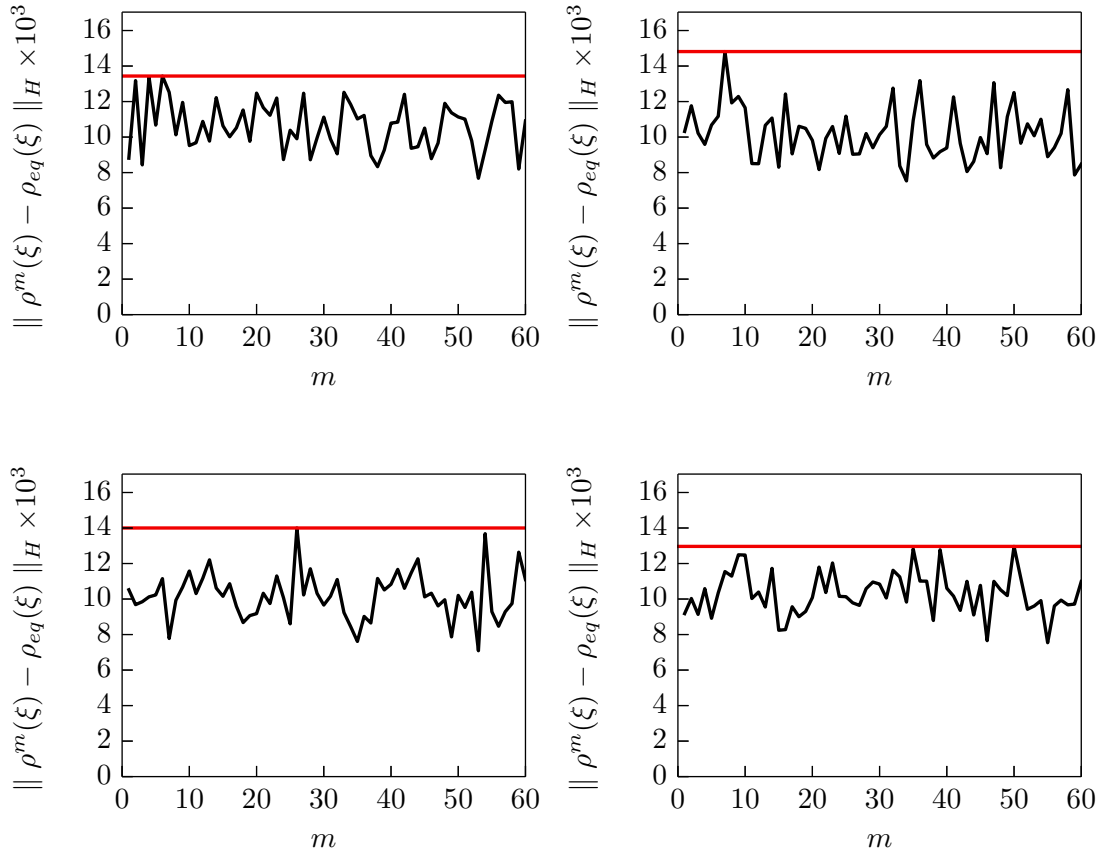


Figure B.1: Hellinger metric for p^{off} , introduced in Eqs. (4.2) and (4.3), as a function of the block index m for *n*-octane (top left), *i*-octane (top right), *n*-hexadecane (bottom left) and *i*-hexadecane (bottom right) at a pressure of 100 kPa and a temperature of 348.15 K for the octane isomers and 473.15 K for the hexadecane isomers. The horizontal (red) line represents the maximum of the Hellinger metric for the given system.

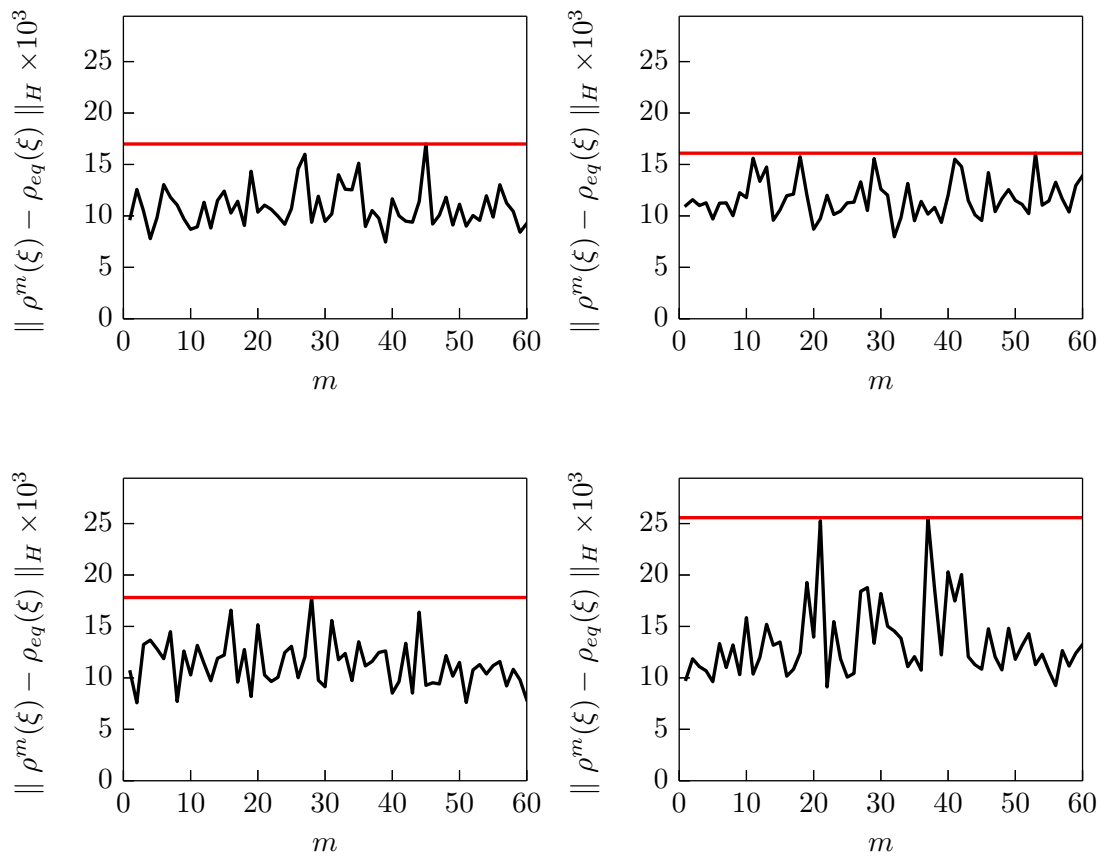


Figure B.2: As in Fig. B.1 for 250 MPa.

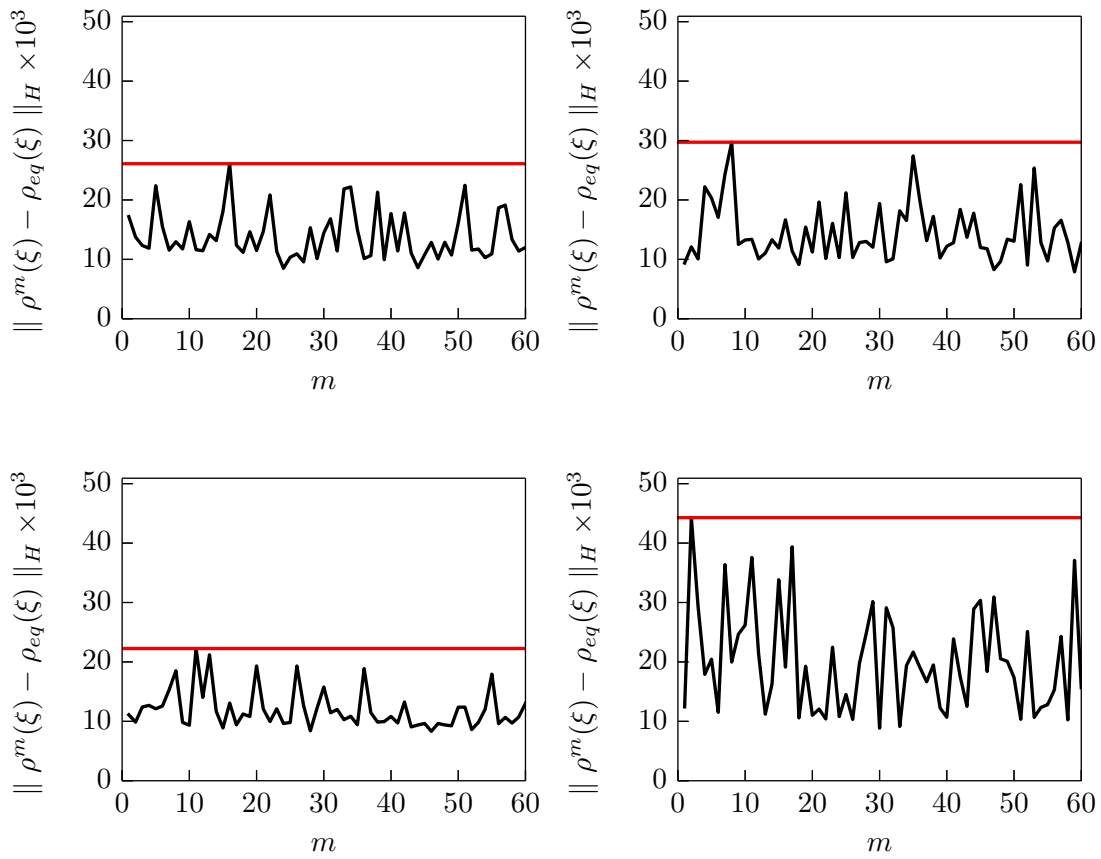


Figure B.3: As in Fig. B.1 for 500 MPa.

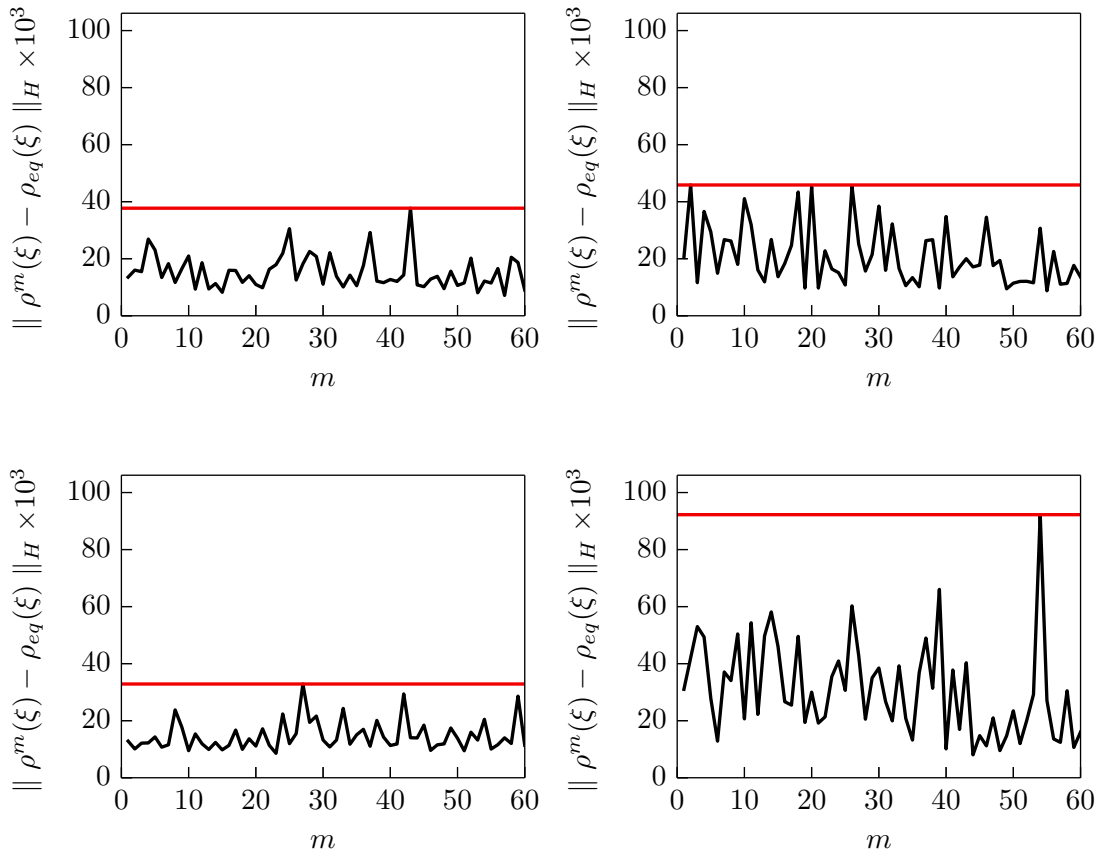


Figure B.4: As in Fig. B.1 for 750 MPa.

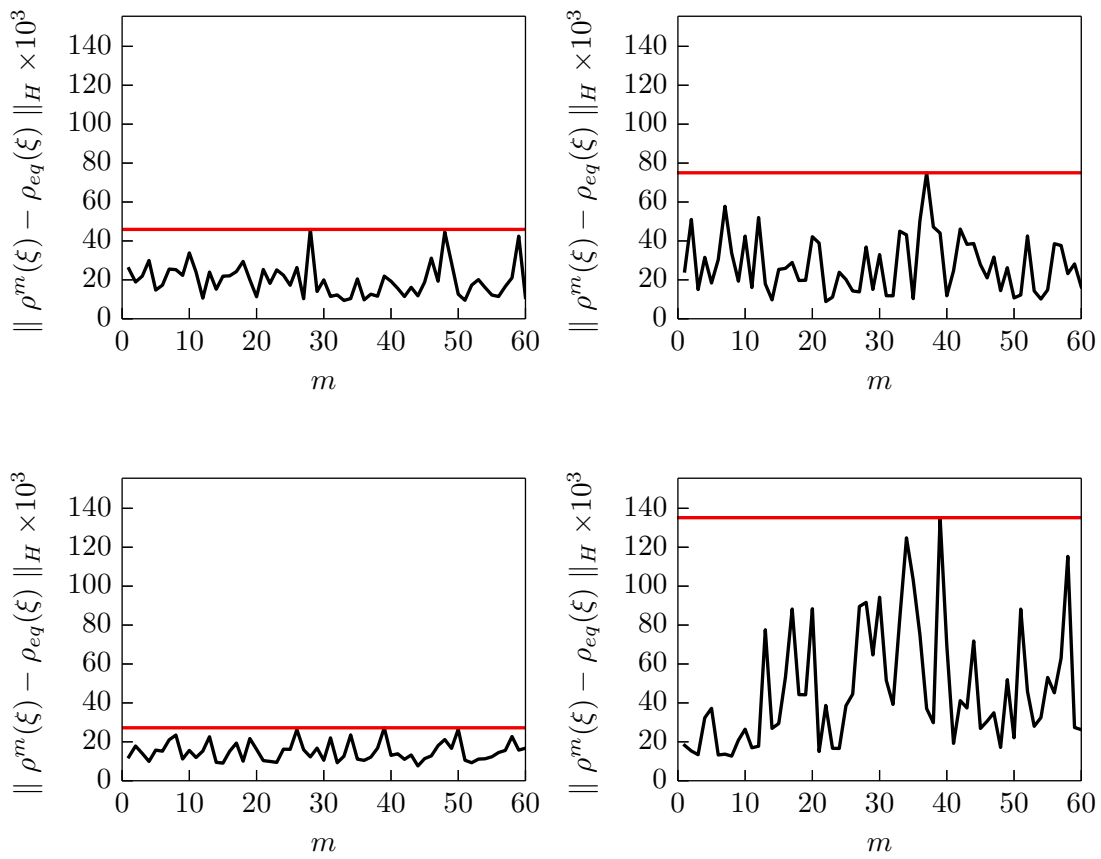


Figure B.5: As in Fig. B.1 for 1 GPa.

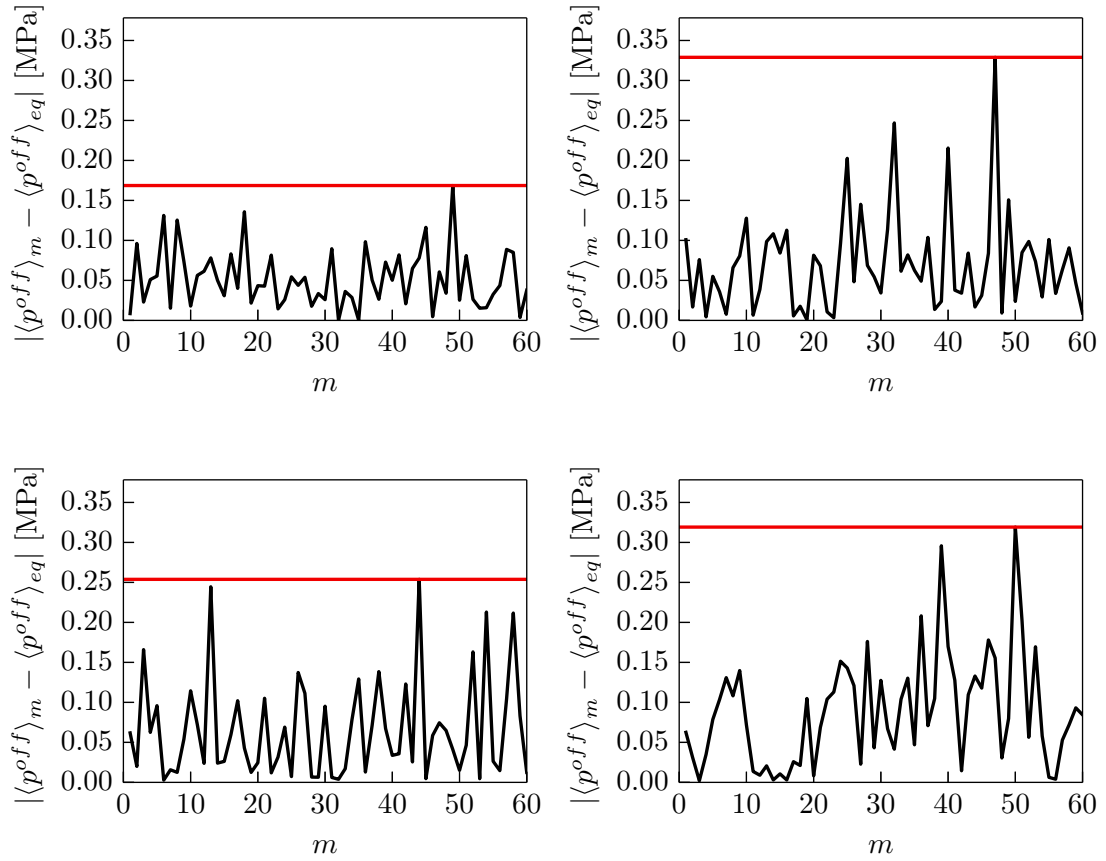


Figure B.6: The absolute deviation of $\langle p^{off} \rangle_m$ from its equilibrium value $\langle p^{off} \rangle_{eq}$ as a function of the block index m according to Eq. (4.4) for *n*-octane (top left), *i*-octane (top right), *n*-hexadecane (bottom left) and *i*-hexadecane (bottom right) at a pressure of 100 kPa and a temperature of 348.15 K for the octane isomers and 473.15 K for the hexadecane isomers. The horizontal (red) line represents the maximum of the deviation for the given system-pressure combination.

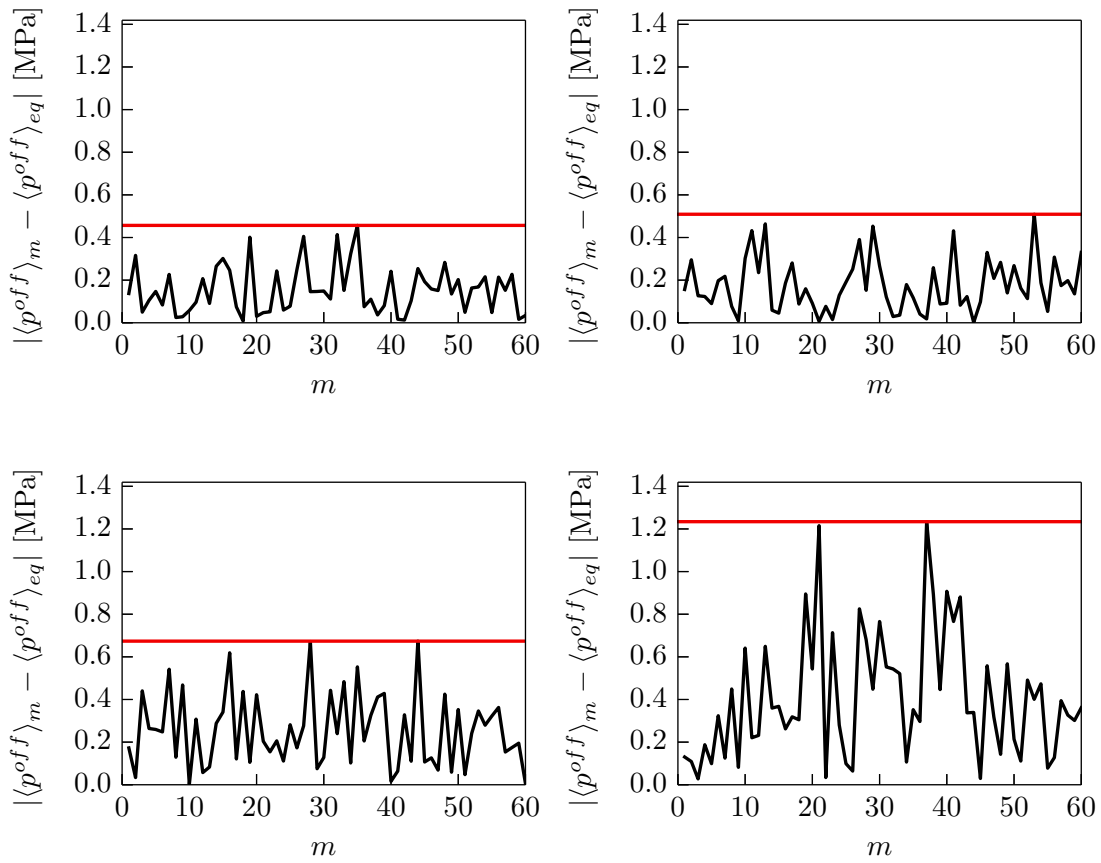


Figure B.7: As in Fig. B.6 for 250 MPa.

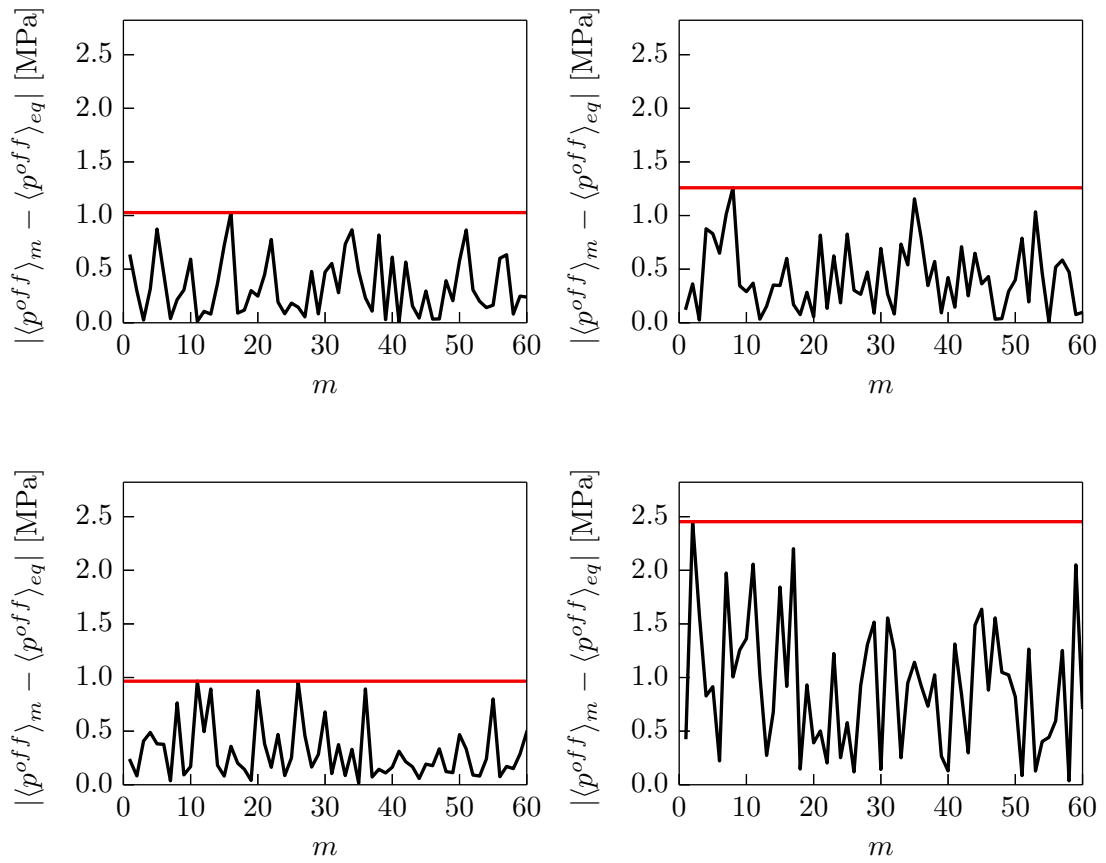


Figure B.8: As in Fig. B.6 for 500 MPa.

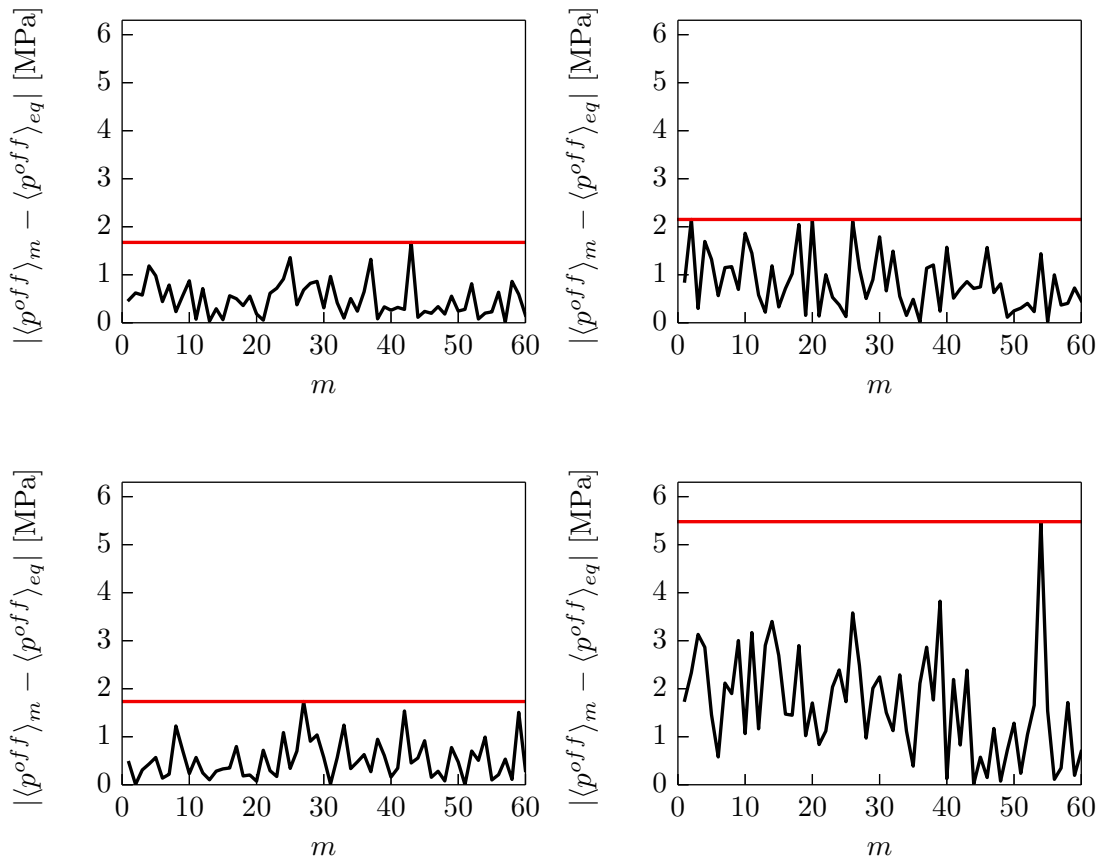


Figure B.9: As in Fig. B.6 for 750 MPa.

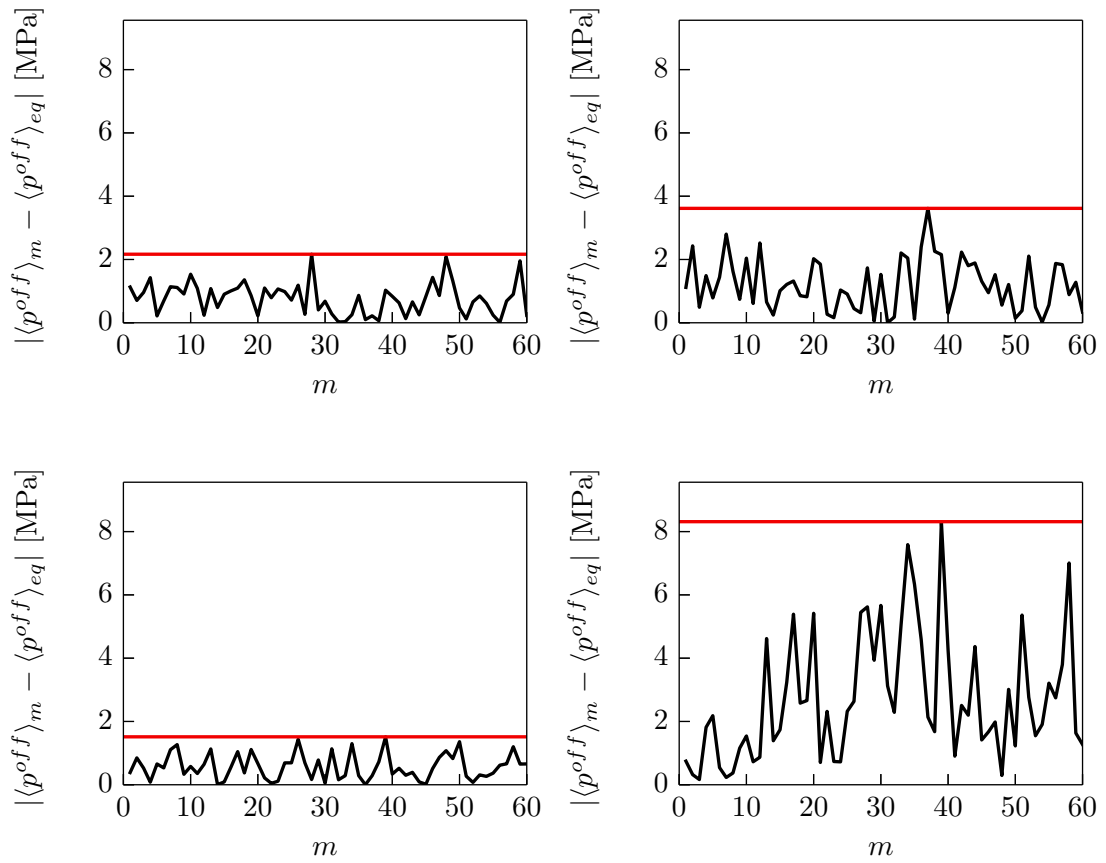
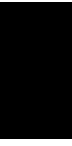


Figure B.10: As in Fig. B.6 for 1 GPa.

APPENDIX

C



Convergence of Zero-shear and Bulk Viscosities

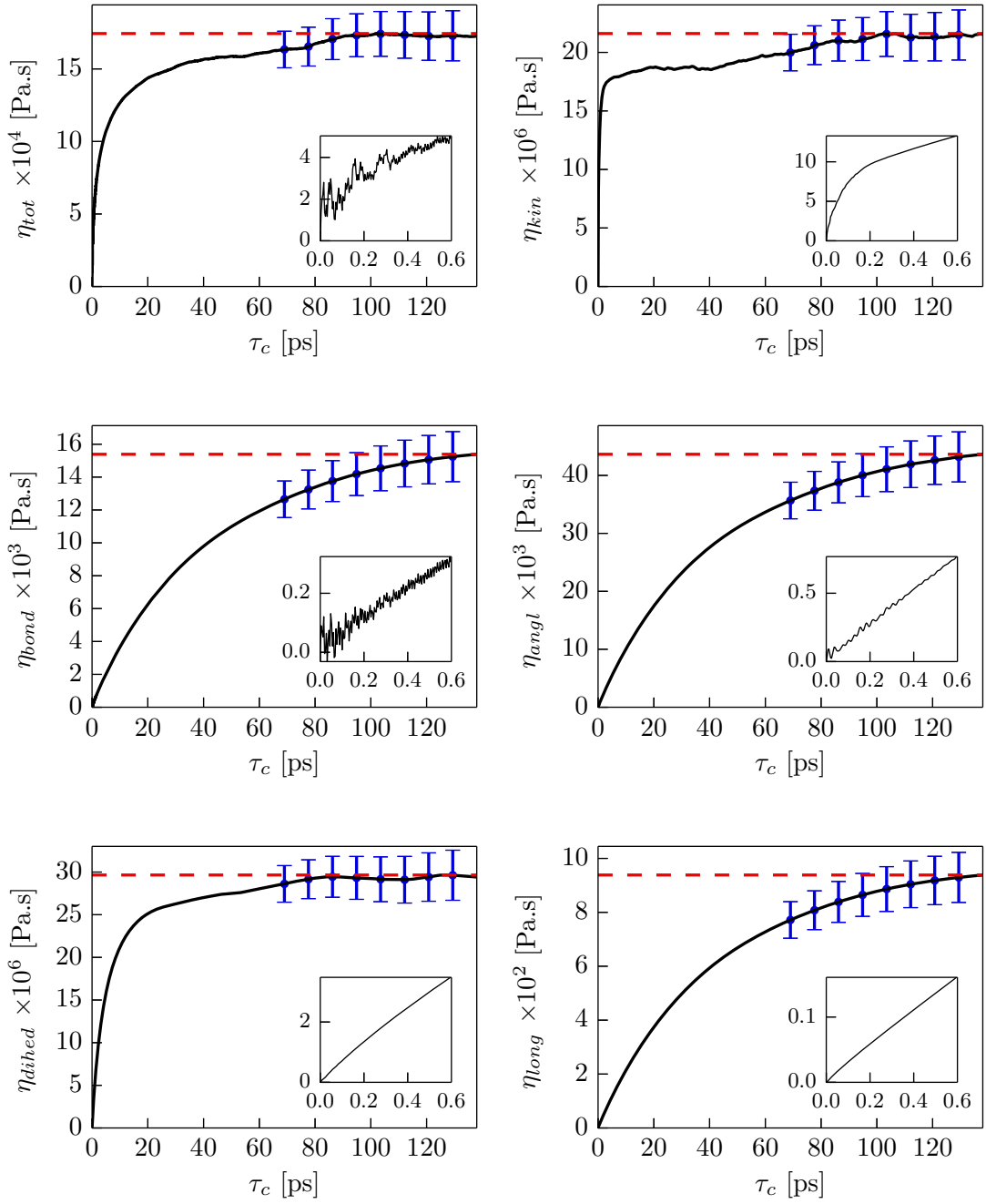


Figure C.1: Zero-shear viscosities in case of *n*-octane at 250 MPa and 348.15 K. The small insets show the first 0.6 ps in higher resolution (the units of the scales are the same as in the large graphs). The error bars represent the standard deviation of the viscosities as calculated by Eq. (4.6). The (red) dashed lines correspond to the maximum value of the viscosity.

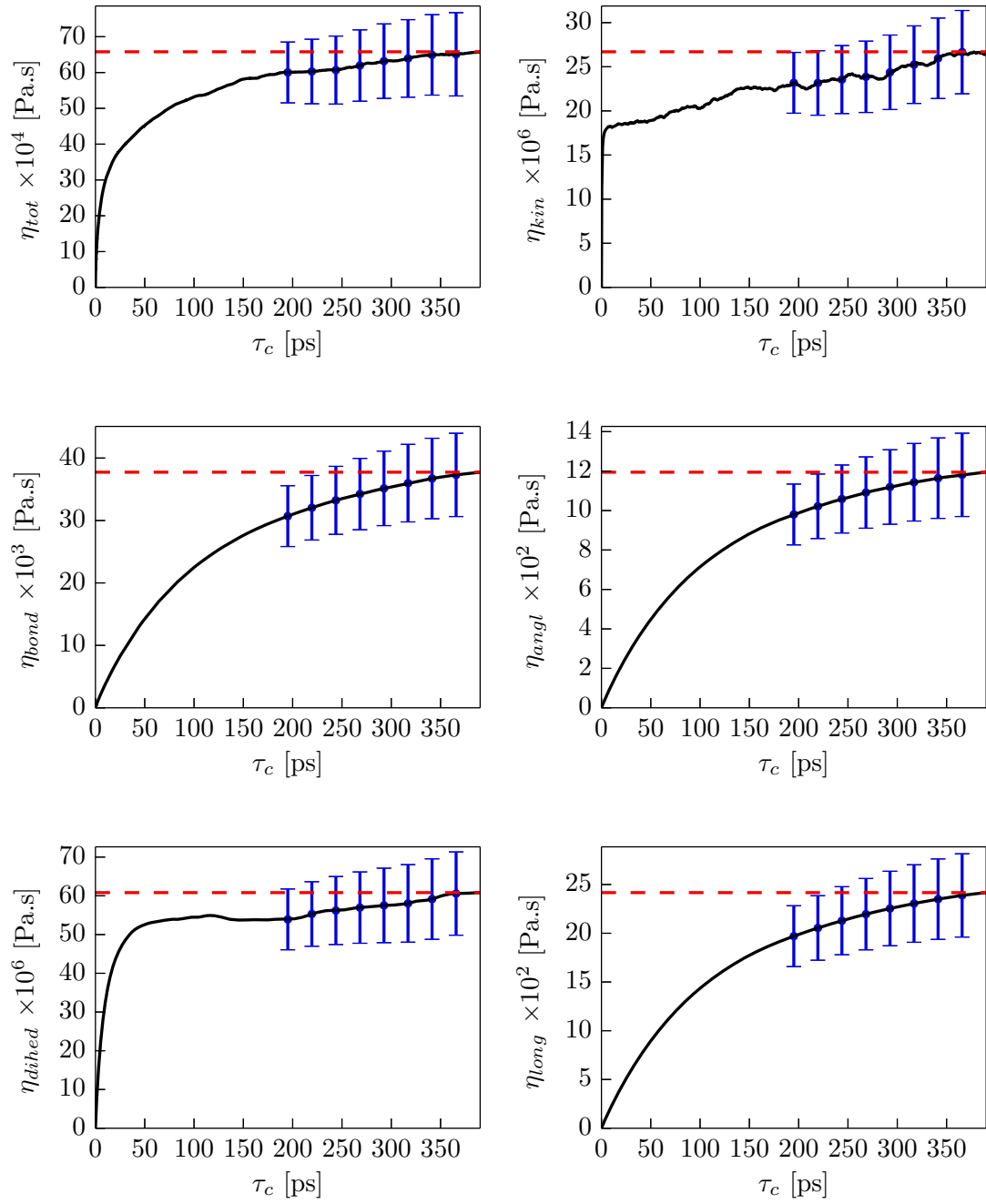


Figure C.2: As Fig. C.1 for 500 MPa.

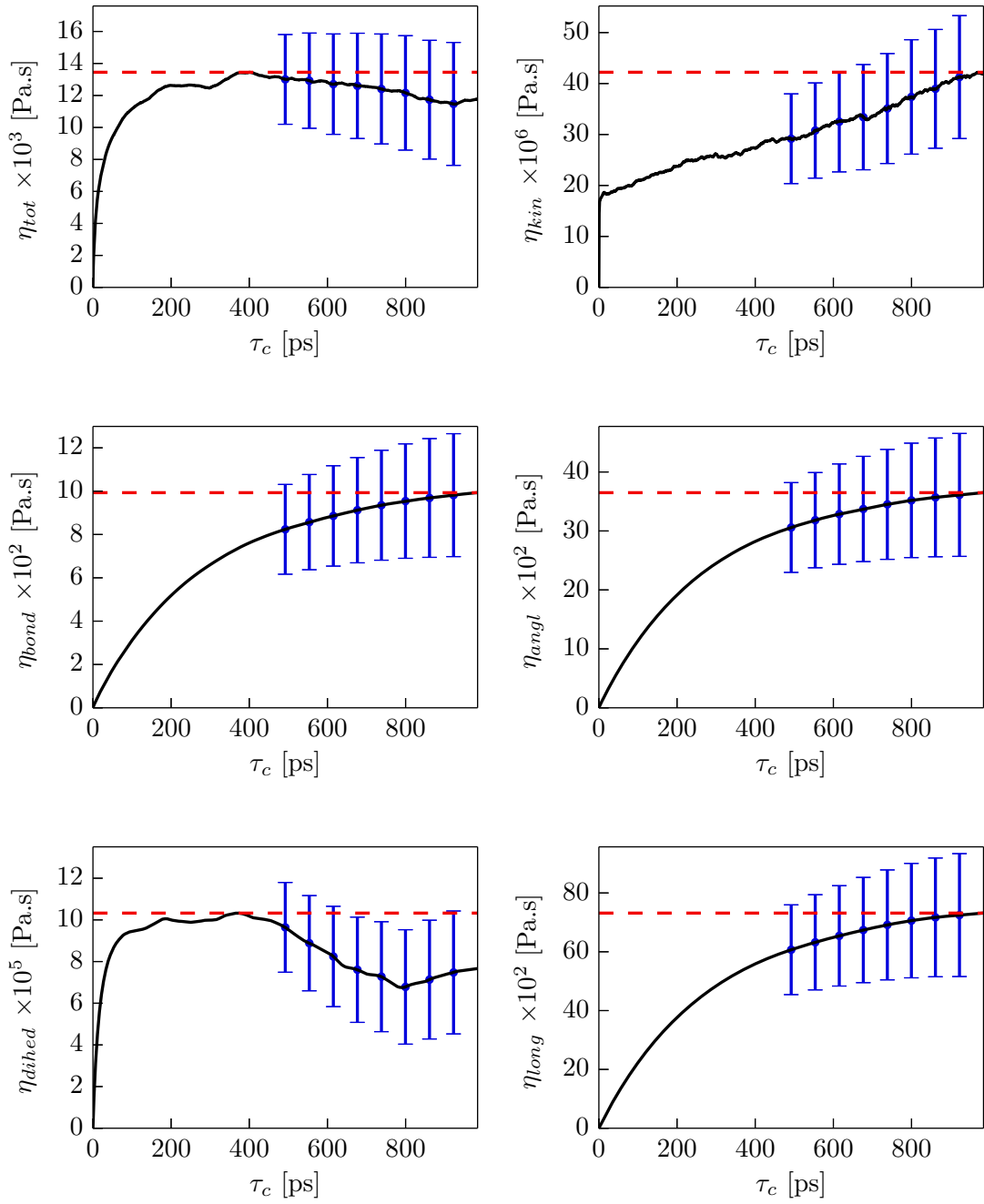


Figure C.3: As Fig. C.1 for 750 MPa.

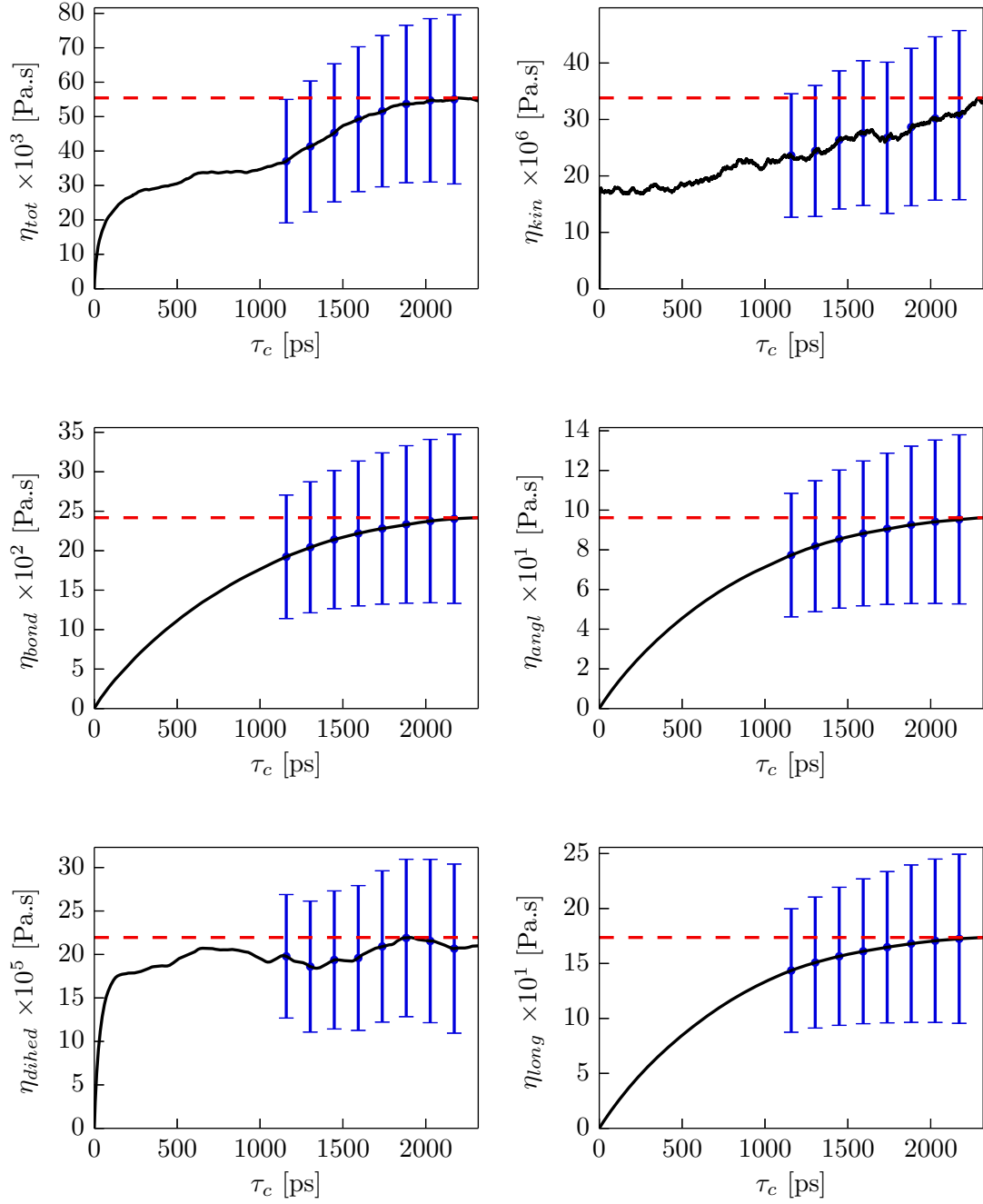


Figure C.4: As Fig. C.1 for 1 GPa.

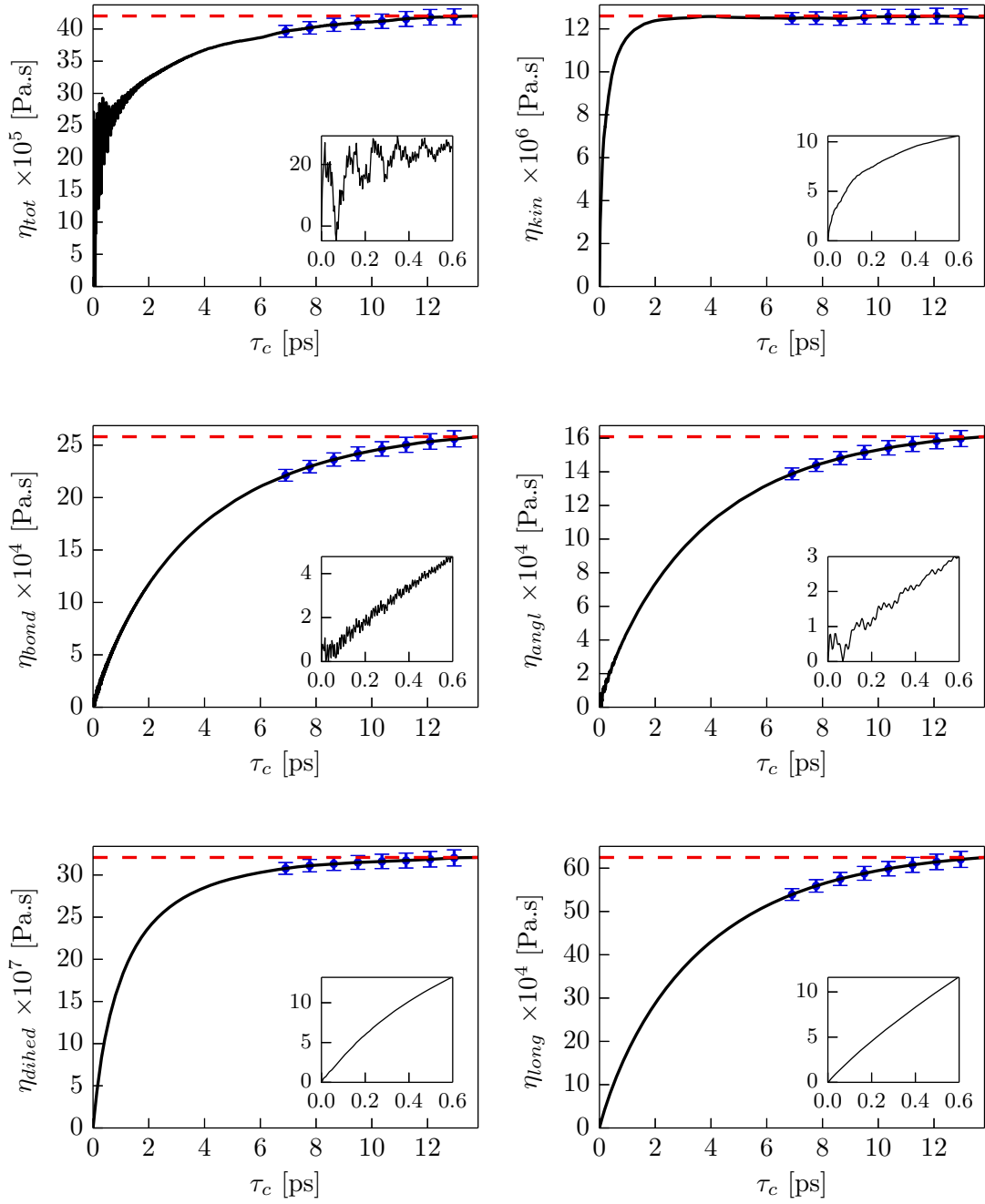


Figure C.5: Zero-shear viscosities in case of *i*-octane at 100 kPa and 348.15 K. The small insets show the first 0.6 ps in higher resolution (the units of the scales are the same as in the large graphs). The error bars represent the standard deviation of the viscosities as calculated by Eq. (4.6). The (red) dashed lines correspond to the maximum value of the viscosity.

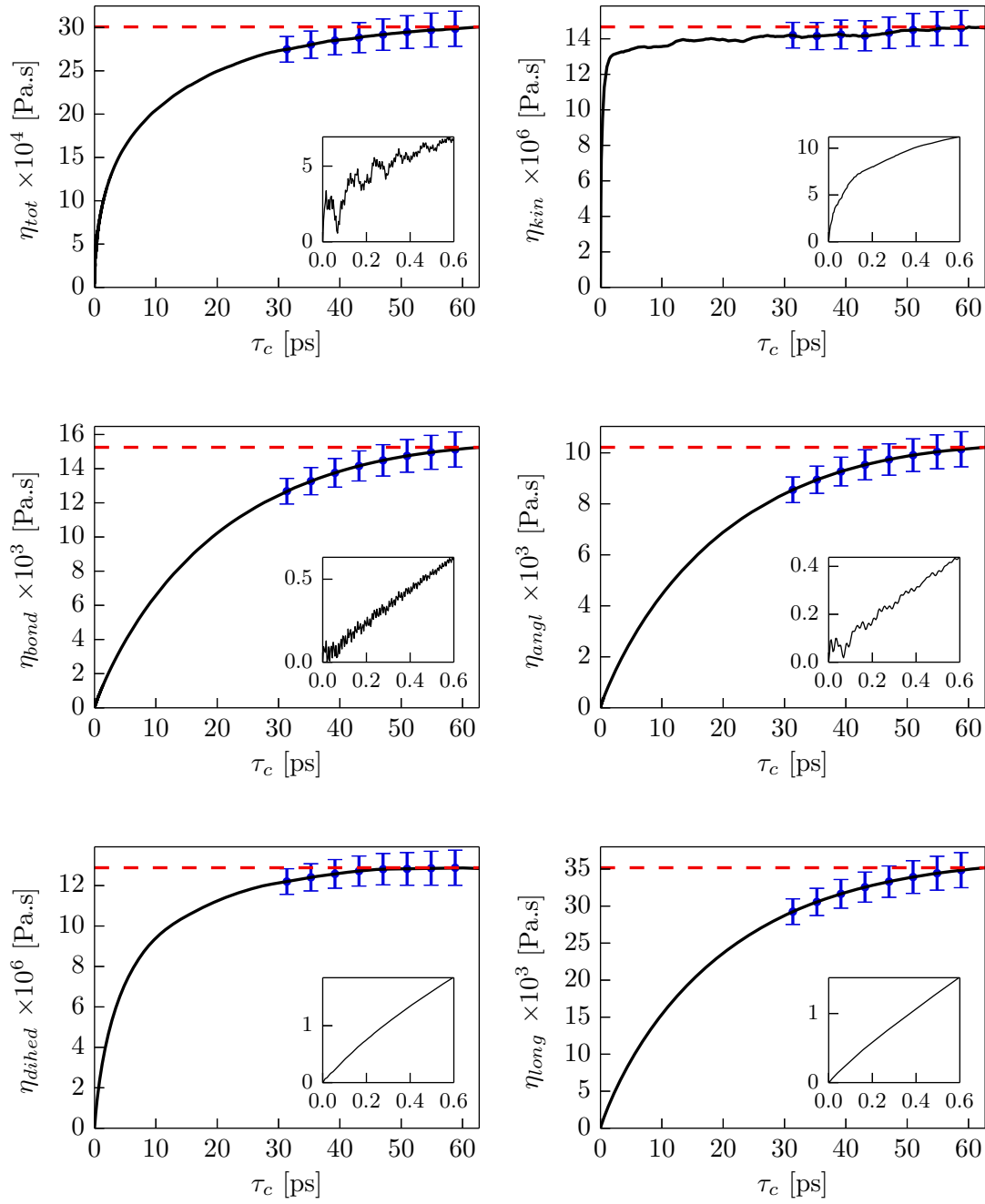


Figure C.6: As Fig. C.5 for 250 MPa.

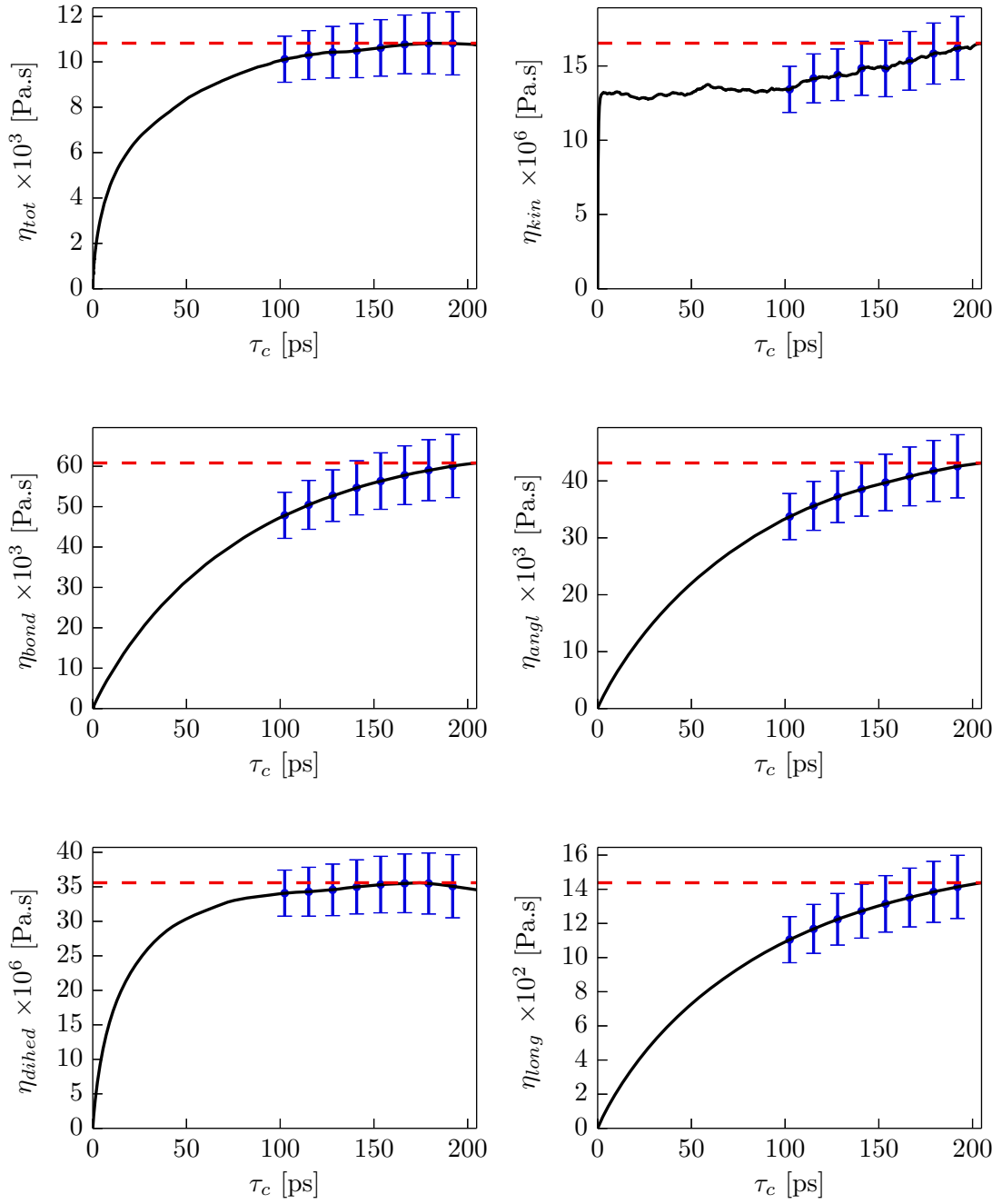


Figure C.7: As Fig. C.5 for 500 MPa.

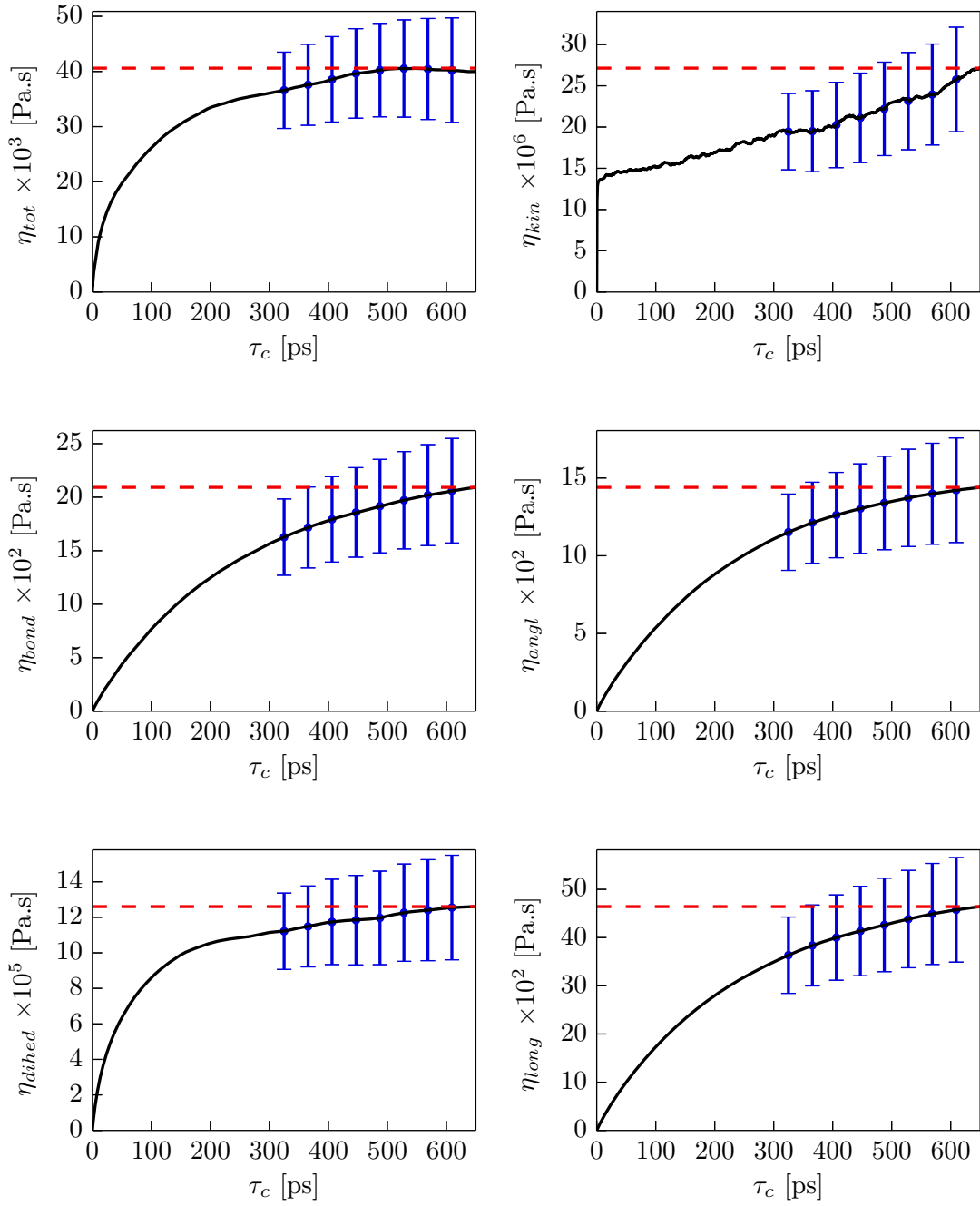


Figure C.8: As Fig. C.5 for 750 MPa.

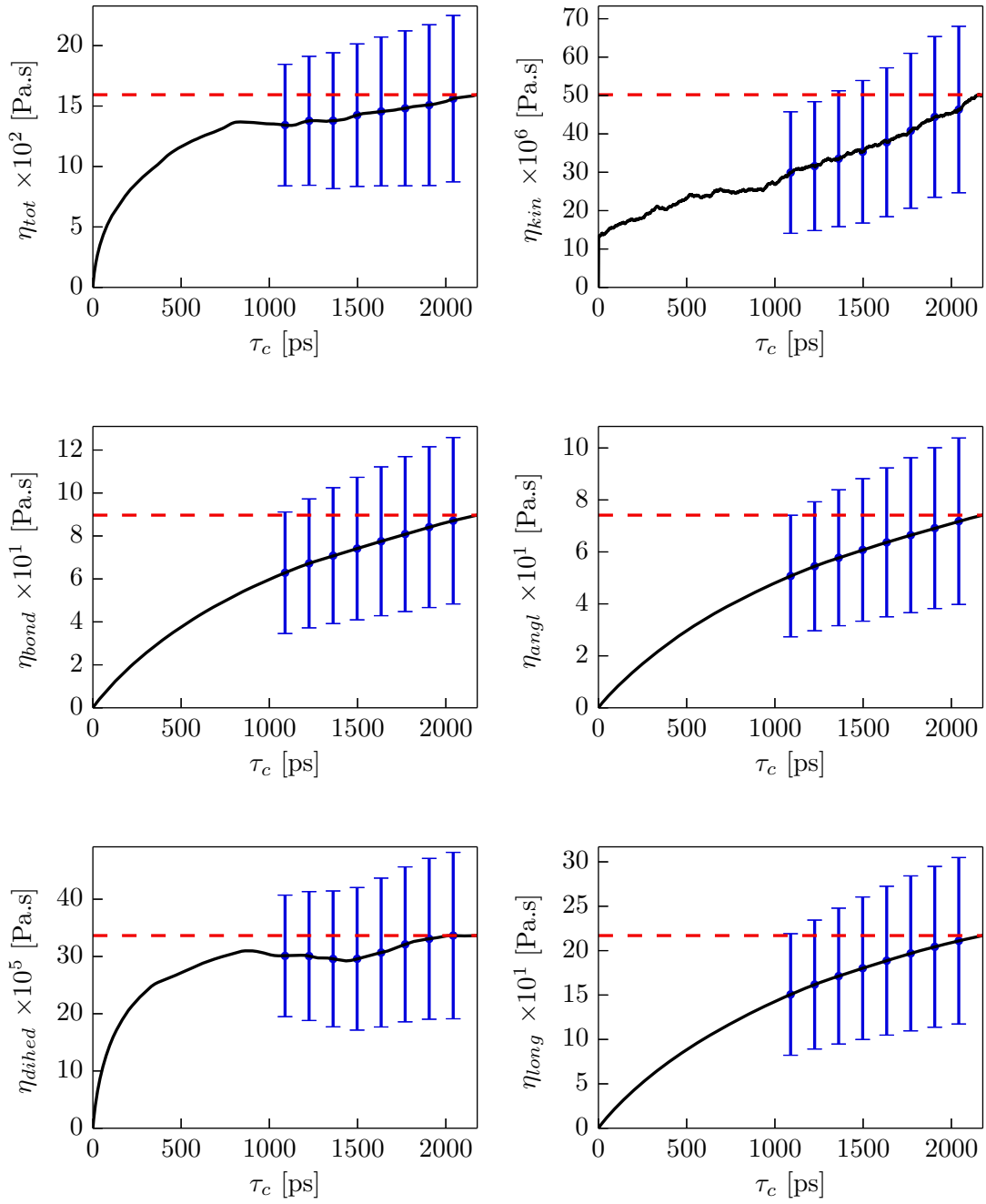


Figure C.9: As Fig. C.5 for 1 GPa.

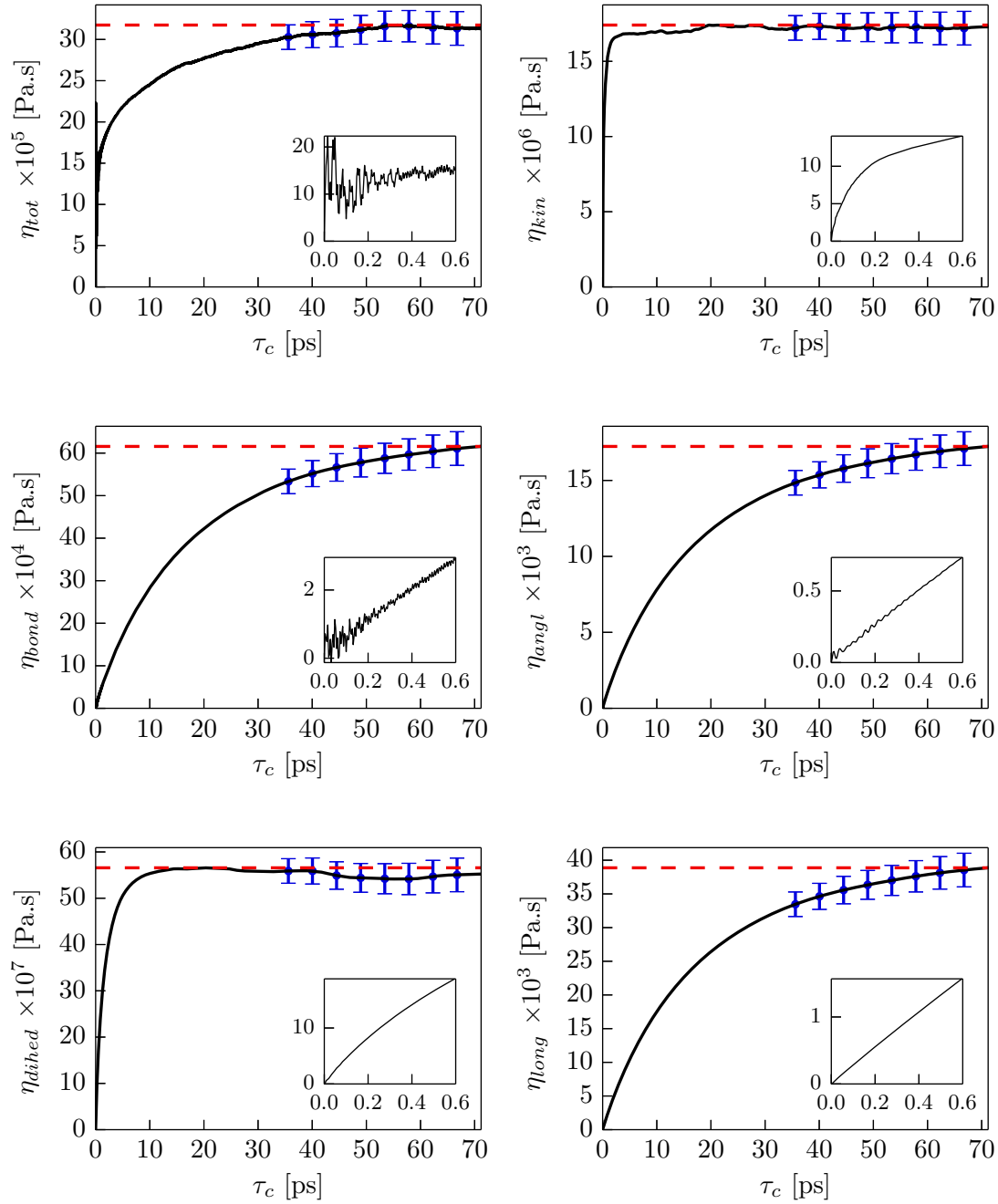


Figure C.10: Zero-shear viscosities in case of *n*-hexadecane at 100 kPa and 473.15 K. The small insets show the first 0.6 ps in higher resolution (the units of the scales are the same as in the large graphs). The error bars represent the standard deviation of the viscosities as calculated by Eq. (4.6). The (red) dashed lines correspond to the maximum value of the viscosity.

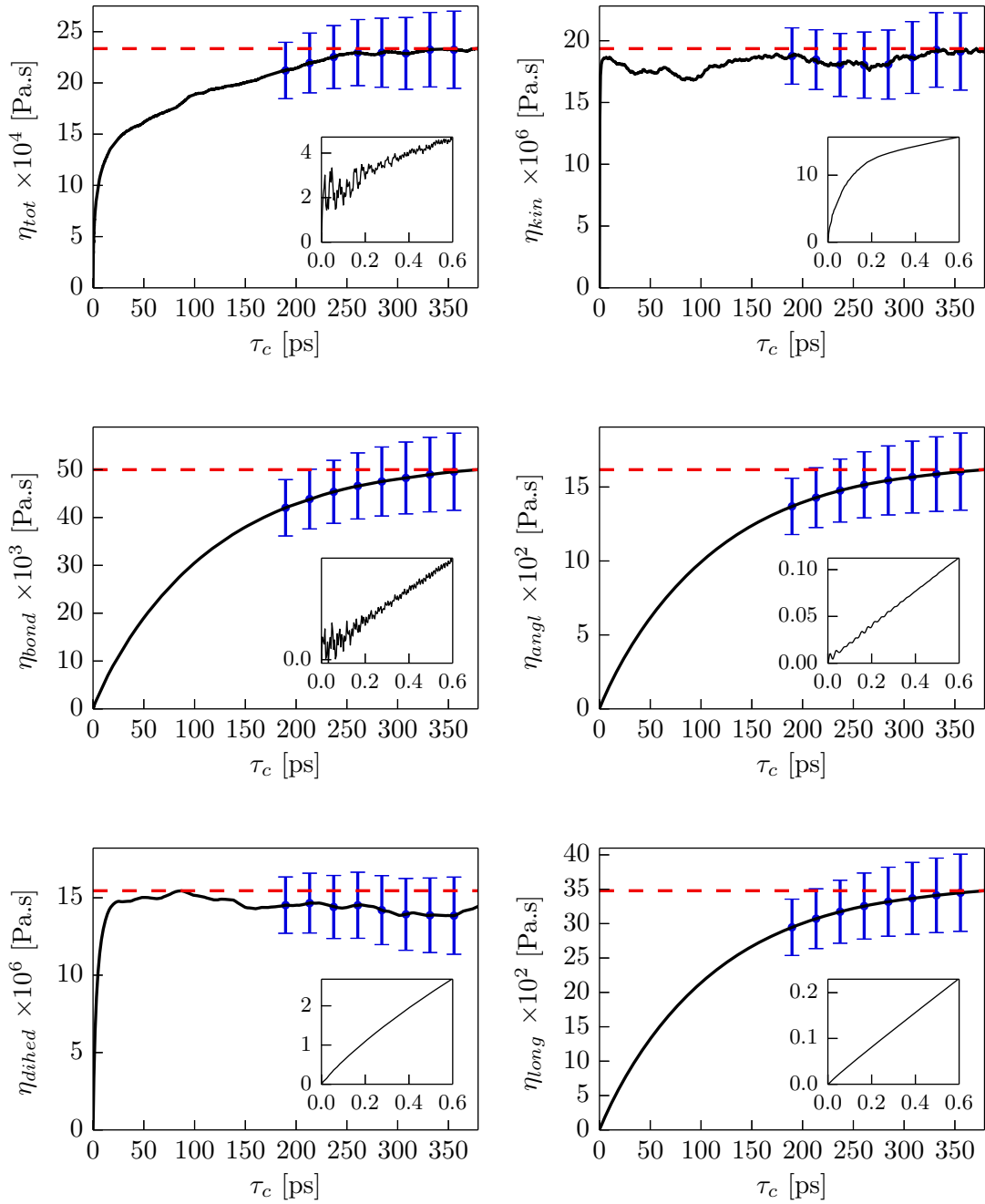


Figure C.11: As Fig. C.10 for 250 MPa.

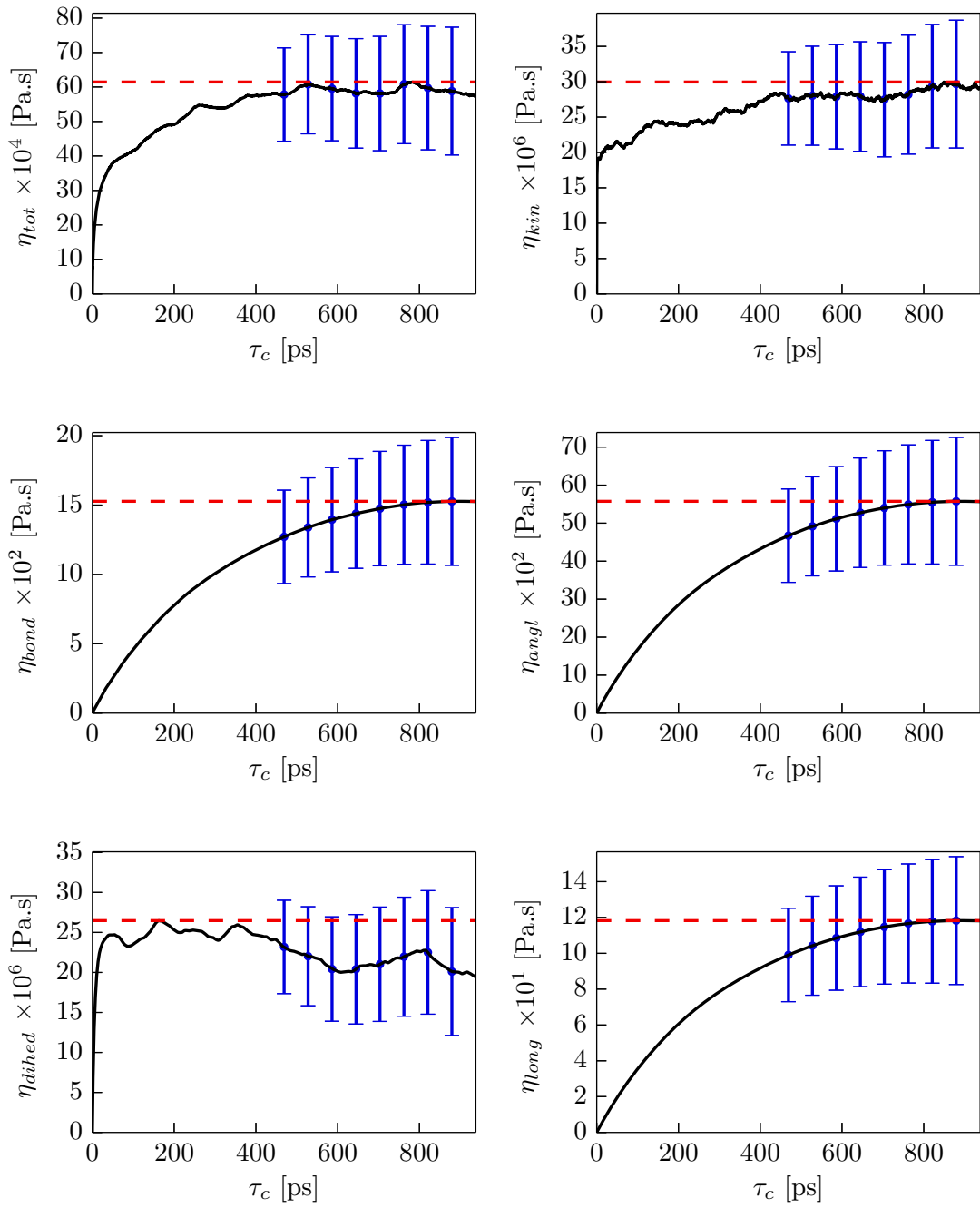


Figure C.12: As Fig. C.10 for 500 MPa.

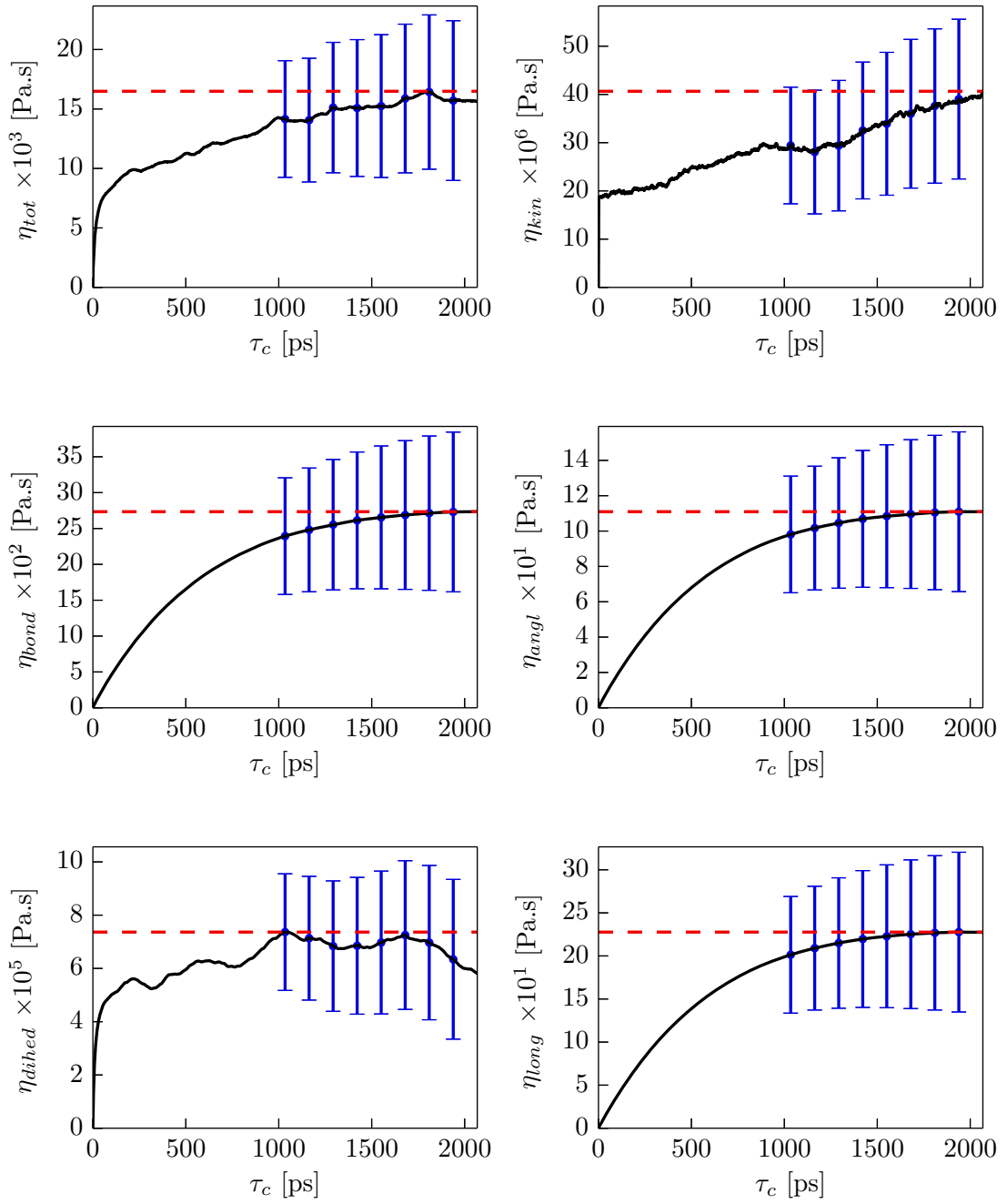


Figure C.13: As Fig. C.10 for 750 MPa.

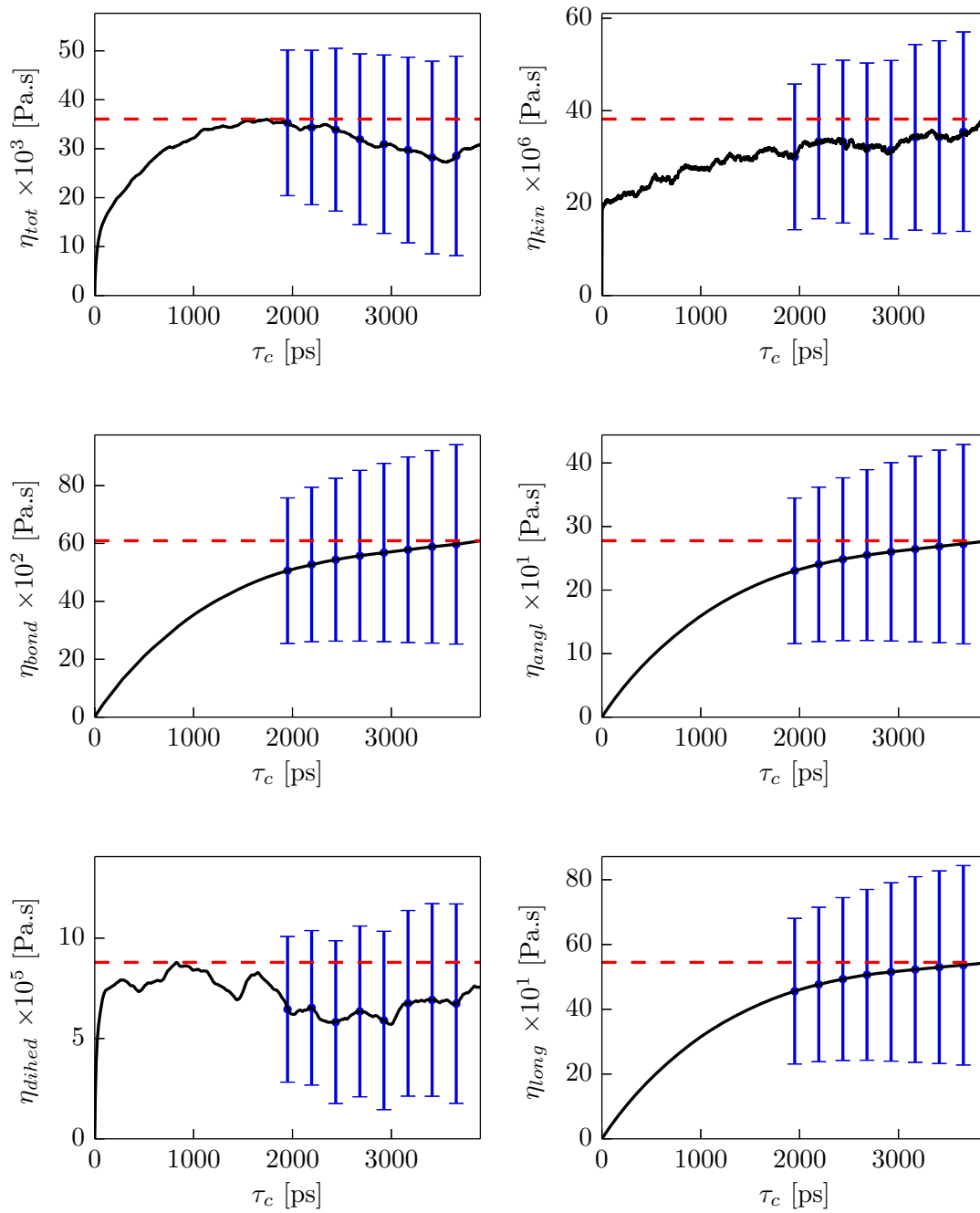


Figure C.14: As Fig. C.10 for 1 GPa.

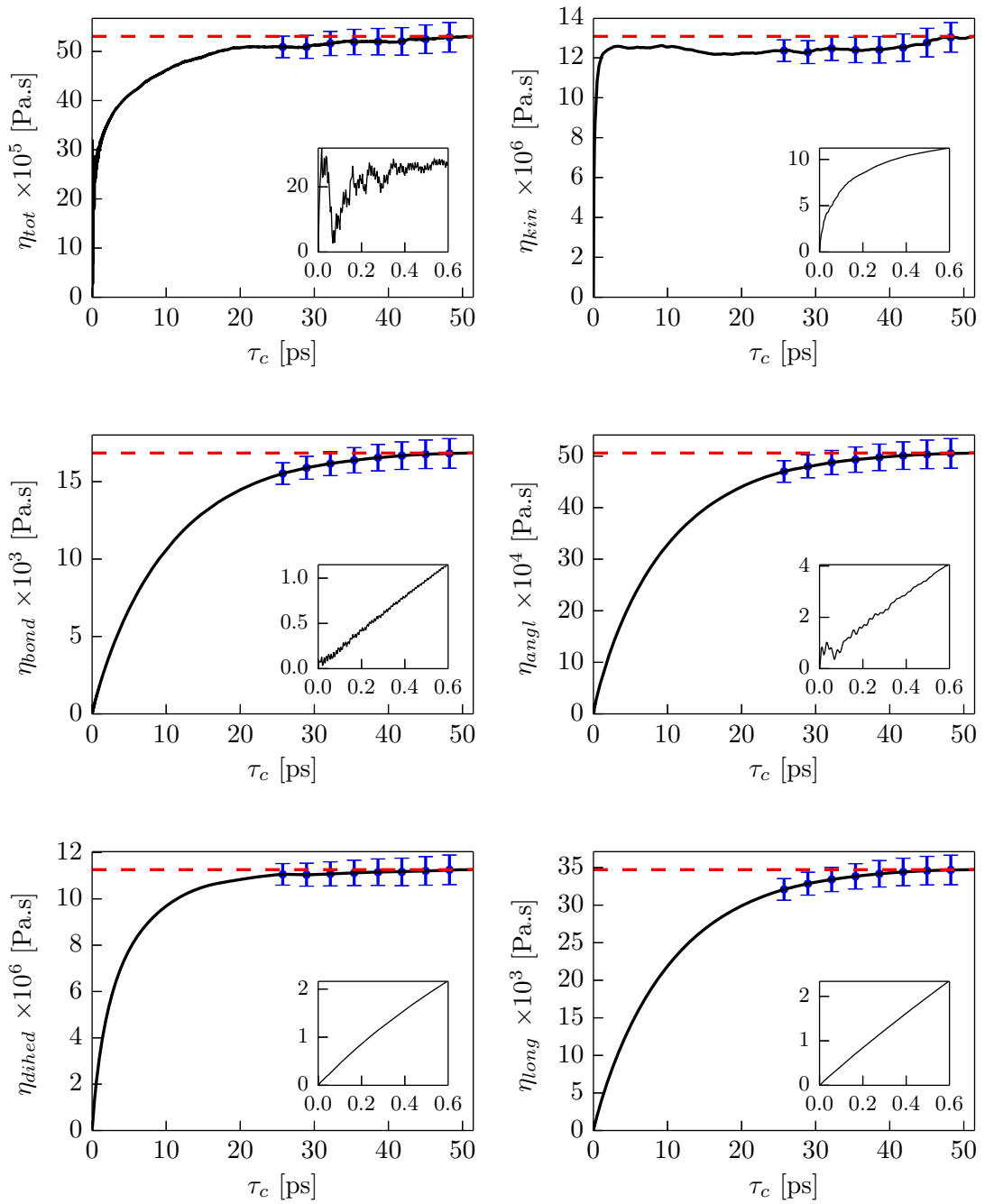


Figure C.15: Zero-shear viscosities in case of *i*-hexadecane at 100 kPa and 473.15 K. The small insets show the first 0.6 ps in higher resolution (the units of the scales are the same as in the large graphs). The error bars represent the standard deviation of the viscosities as calculated by Eq. (4.6). The (red) dashed lines correspond to the maximum value of the viscosity.

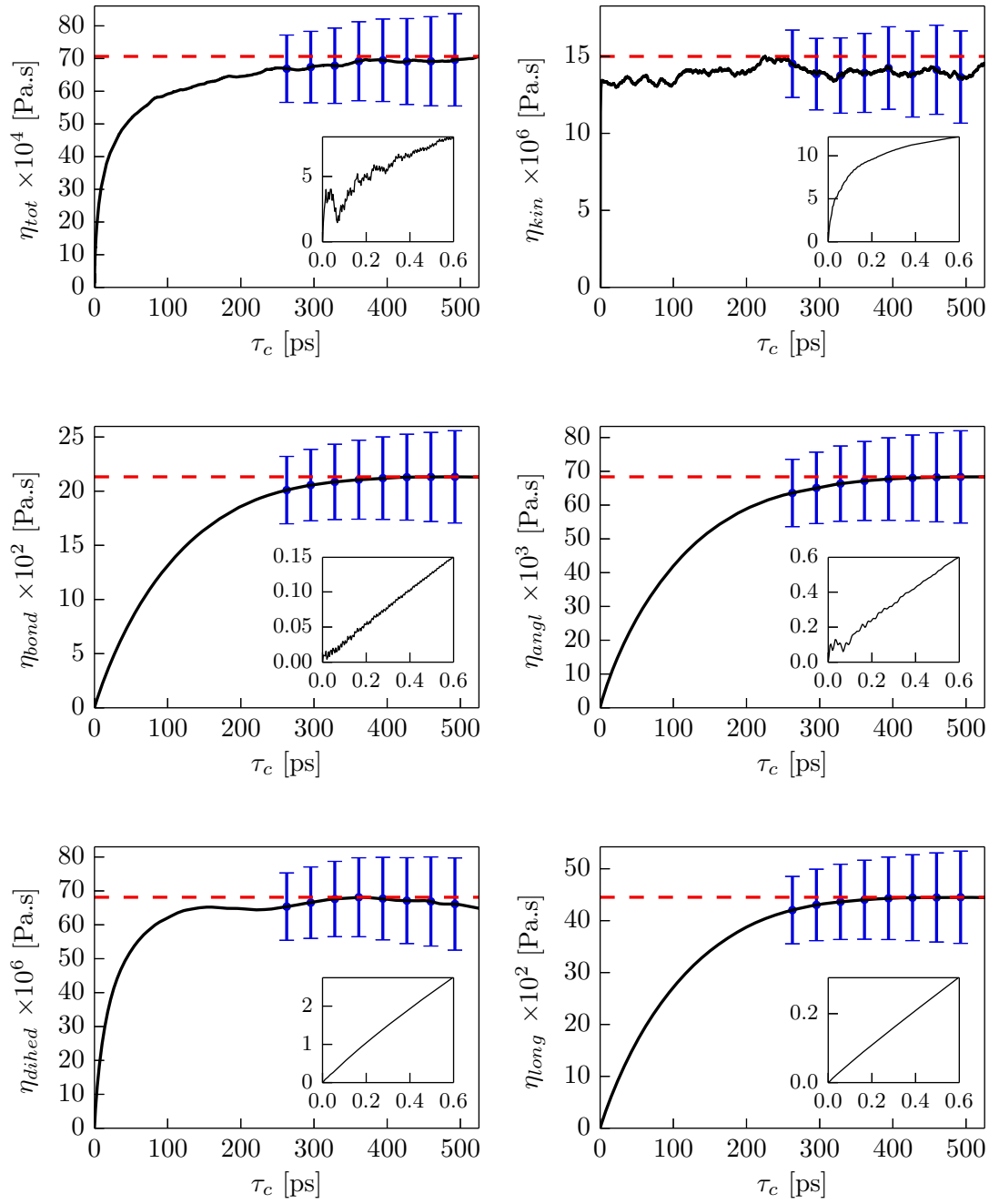


Figure C.16: As Fig. C.15 for 250 MPa.

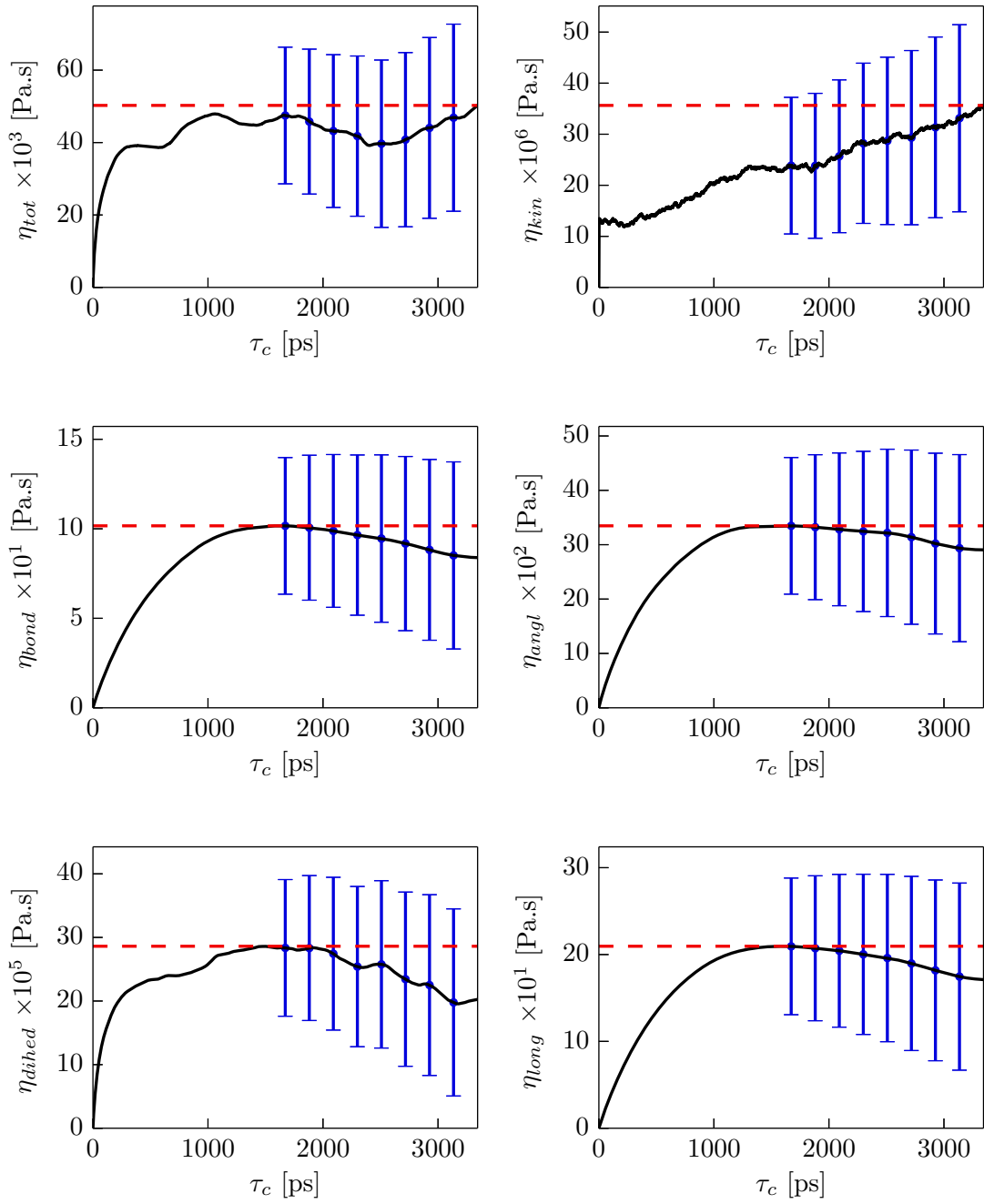


Figure C.17: As Fig. C.15 for 500 MPa.

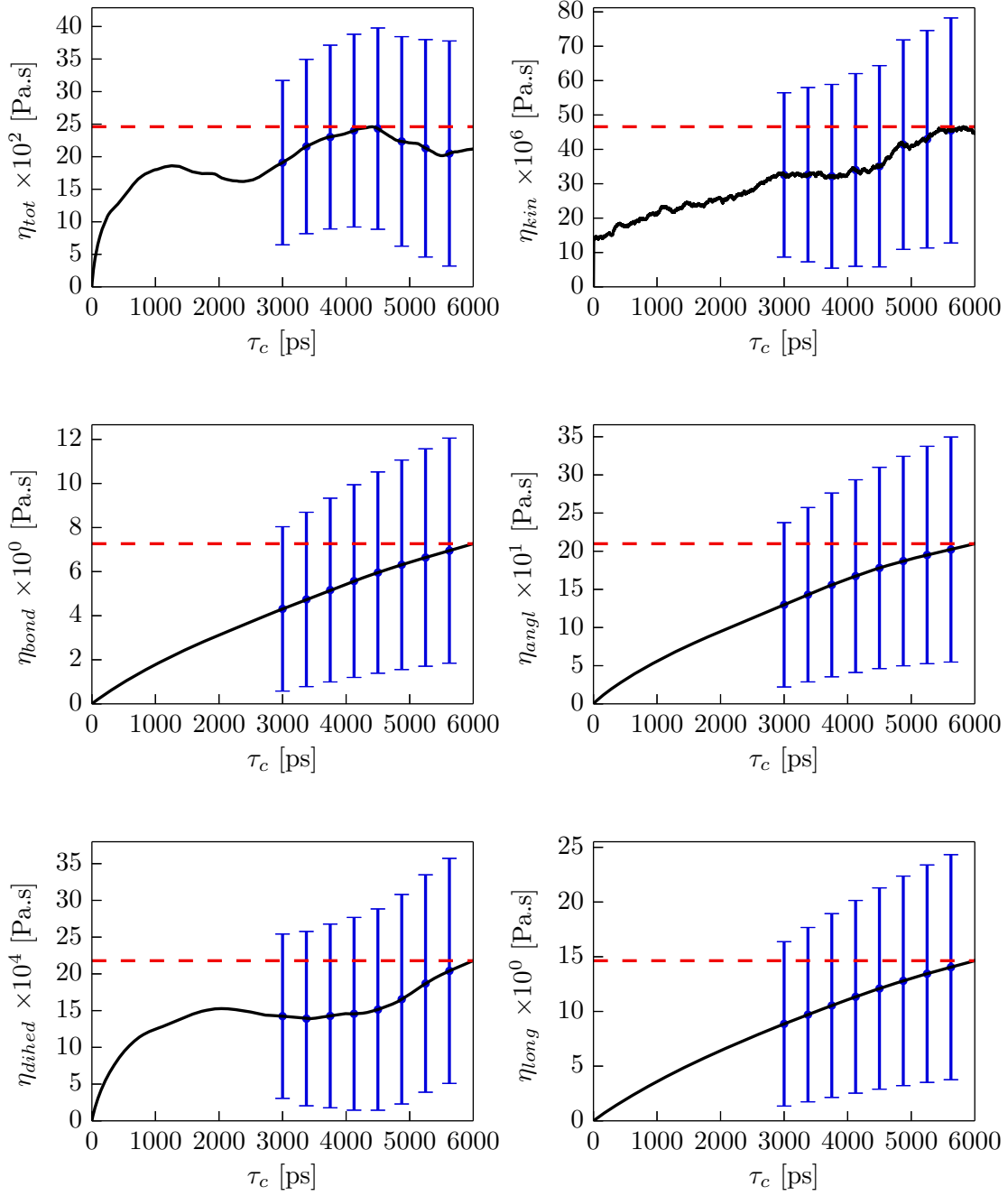


Figure C.18: As Fig. C.15 for 750 MPa.

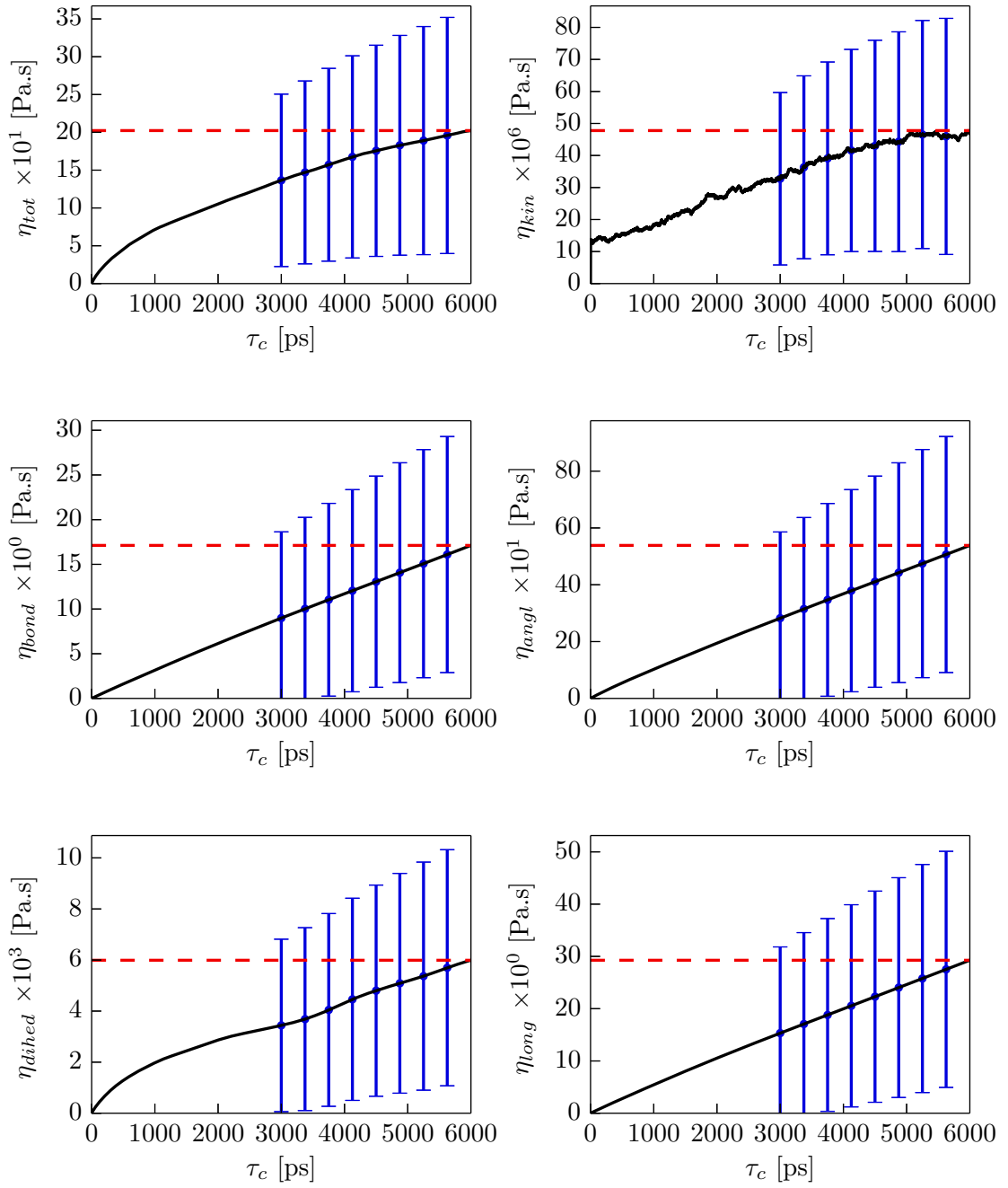


Figure C.19: As Fig. C.15 for 1 GPa.

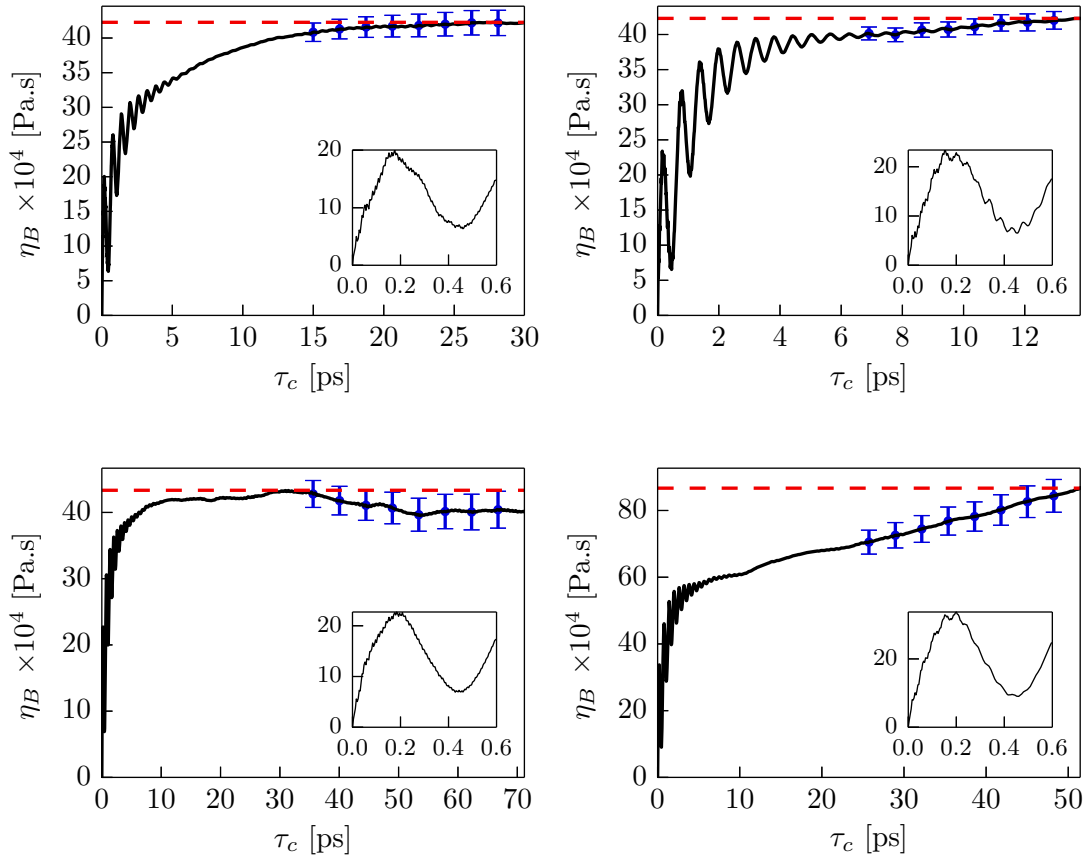


Figure C.20: Bulk viscosity in case of *n*-octane (top left), *i*-octane (top right), *n*-hexadecane (bottom left) and *i*-hexadecane (bottom right) at a pressure of 100 kPa and a temperature of 348.15 K for the octane isomers and 473.15 for the hexadecane isomers. The small insets show the first 0.6 ps in higher resolution (the units of the scales are the same as in the large graphs). The error bars represent the standard deviation of the viscosities as calculated by Eq. (4.6). The (red) dashed lines correspond to the maximum value of the viscosity.

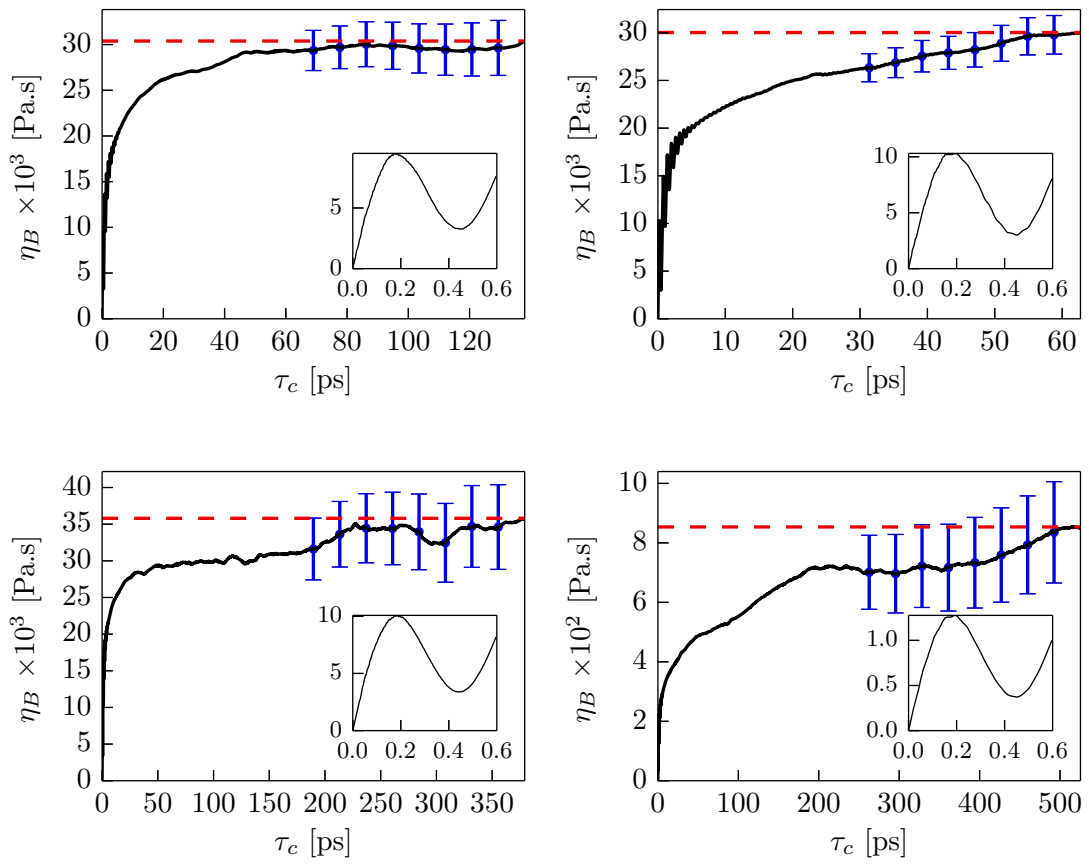


Figure C.21: As Fig. C.20 for 250 MPa.

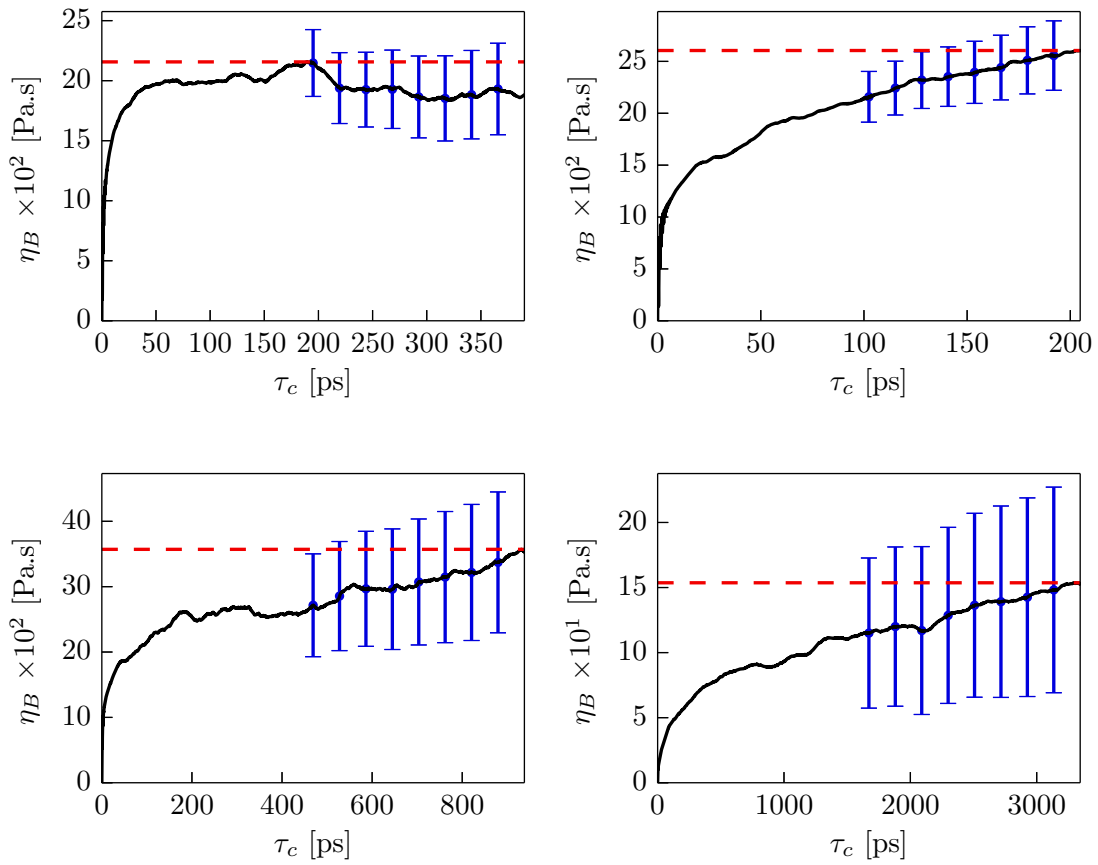


Figure C.22: As Fig. C.20 for 500 MPa.

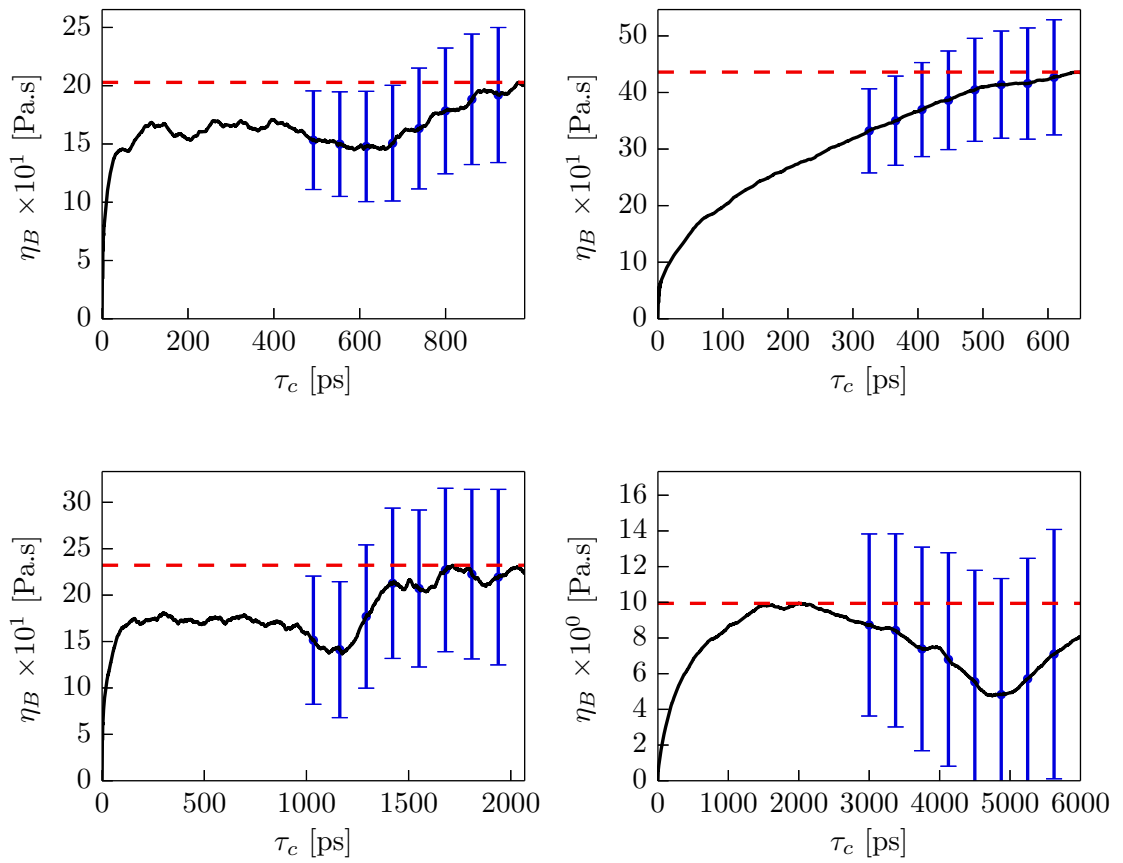


Figure C.23: As Fig. C.20 for 750 MPa.

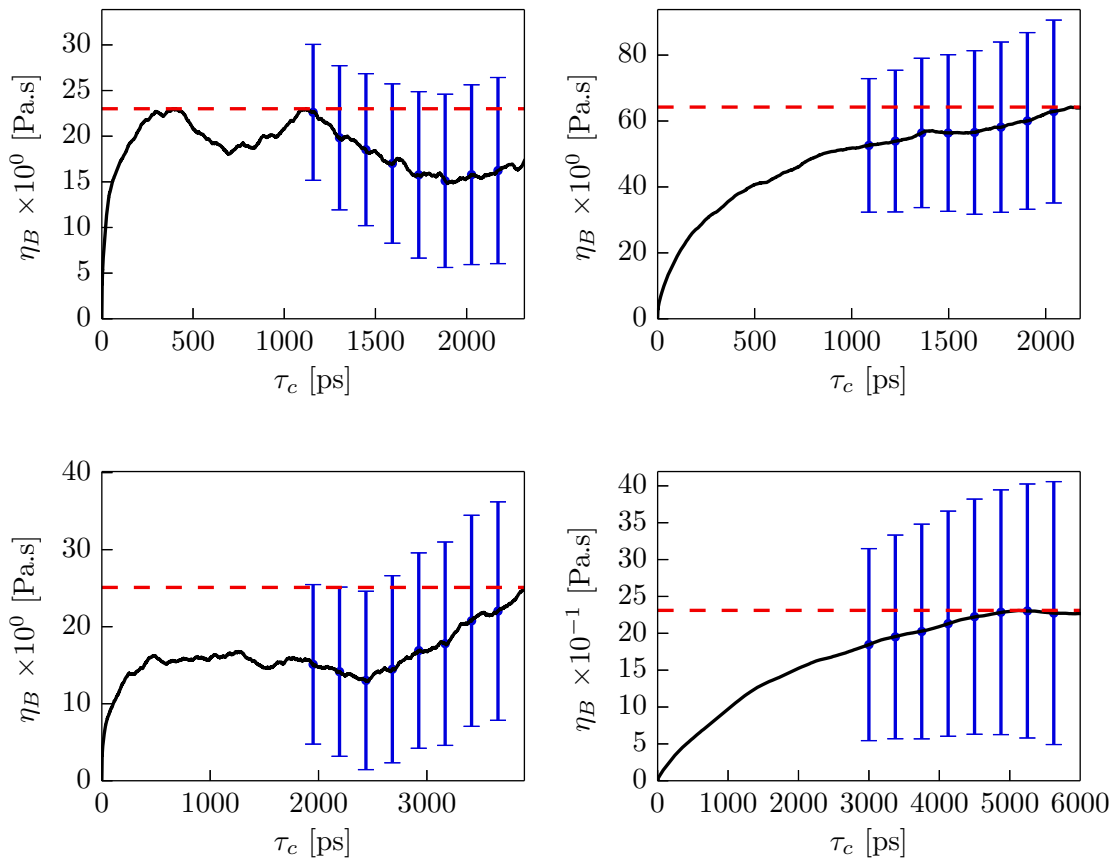


Figure C.24: As Fig. C.20 for 1 GPa.

Bibliography

- [1] M. Björling, W. Habchi, S. Bair, R. Larsson, and P. Marklund. Towards the true prediction of EHL friction. *Tribology International*, 66:19–26, 2013.
- [2] L. R. Rudnick, editor. *Synthetics, Mineral Oils, and Bio-Based Lubricants: Chemistry and Technology*. Taylor & Francis, 2006.
- [3] R. Kubo, M. Toda, and N. Hashitsume. *Statistical Physics II, Nonequilibrium Statistical Mechanics*. Springer Series in Solid-State Sciences, 1985.
- [4] R. Kubo. Statistical-Mechanical Theory of Irreversible Processes. I. *Journal of the Physical Society of Japan*, 12(6):570–586, 1957.
- [5] D. J. Evans and G. P. Morriss. *Statistical Mechanics of Nonequilibrium Liquids*. Academic Press, London, 1990.
- [6] R. Zwanzig. Time-correlation functions and transport coefficients in statistical mechanics. *Annual Review of Physical Chemistry*, 16:67–102, 1965.
- [7] M. E. Tuckerman and G. J. Martyna. Understanding Modern Molecular Dynamics: Techniques and Applications. *The Journal of Physical Chemistry B*, 104:159–178, 2000.
- [8] S. J. Plimpton. Fast parallel algorithms for short-range molecular dynamics. *Journal of Computational Physics*, 117:1–19, 1995.
- [9] W. G. Hoover. Canonical dynamics: Equilibrium phase-space distributions. *Physical Review A*, 31(3):1695–1697, 1985.
- [10] M. H. Cohen and D. Turnbull. Nose–hoover chains: The canonical ensemble via continuous dynamics. *The Journal of Chemical Physics*, 97:2635–2643, 1992.
- [11] M. Tuckerman, B. J. Berne, and G. J. Martyna. Reversible multiple time scale molecular dynamics. *The Journal of Chemical Physics*, 97:1990–2001, 1992.
- [12] O. A. Mazyar, G. Pan, and C. McCabe. Transient time correlation function calculation of the viscosity of a molecular fluid at low shear rates: a comparison of stress tensors. *Molecular Physics*, 107(14):1423–1429, 2009.
- [13] S. T. Cui, P. T. Cummings, and H. D. Cochran. The calculation of viscosity of liquid n-decane and n-hexadecane by the Green Kubo method. *Molecular Physics*, 93(1):117–121, 1998.
- [14] S. T. Cui, S. A. Gupta, and P. T. Cummings. Molecular dynamics simulations of the rheology of normal decane, hexadecane, and tetracosane. *The Journal of Chemical Physics*, 105(3):1214–1220, 1996.

- [15] T. Chen, B. Smit, and A. T. Bell. Are pressure fluctuation-based equilibrium methods really worse than nonequilibrium methods for calculating viscosities? *The Journal of Chemical Physics*, 131:246101, 2009.
- [16] C. Hoheisel. Bulk viscosity of model fluids. a comparison of equilibrium and nonequilibrium molecular dynamics results. *The Journal of Chemical Physics*, 86:2328–2333, 1987.
- [17] R. E. Jones and K. K. Mandadapu. Adaptive Green-Kubo estimates of transport coefficients from molecular dynamics based on robust error analysis. *The Journal of Chemical Physics*, 136:154102, 2012.
- [18] C. McCabe, S. Cui, P. T. Cummings, P. A. Gordon, and R. B. Saeger. Examining the rheology of 9-octylheptadecane to giga-pascal pressures. *The Journal of Chemical Physics*, 114(4):1887–1891, 2001.
- [19] D. K. Dysthe, A. H. Fuchs, and B. Rousseau. Fluid transport properties by equilibrium molecular dynamics. I. Methodology at extreme fluid states. *The Journal of Chemical Physics*, 110:4047–4059, 1999.
- [20] C. Barus. Isothermals, Isopiestic and Isometrics relative to Viscosity. *American Journal of Science - Third Series*, XLV(266):87–96, 1893.
- [21] S. Bair, Y. Liu, and Q. J. Wang. The Pressure-Viscosity Coefficient for Newtonian EHL Film Thickness With General Piezoviscous Response. *Transactions of the ASME*, 128:624–631, 2006.
- [22] H. Eyring. Viscosity, Plasticity, and Diffusion as Examples of Absolute Reaction Rates. *The Journal of Chemical Physics*, 4:283–291, 1936.
- [23] S. E. Babb and G. J. Scott. Rough viscosities to 10 000 bars. *The Journal of Chemical Physics*, 40:3666–3668, 1964.
- [24] C. J. A. Roelands. *Correlational Aspects of the Viscosity-Temperature-Pressure Relationship of Lubricating Oils*. Doctoral thesis, Technische Universiteit Delft, 1966.
- [25] C. H. Venner and A. A. Lubrecht. *Multilevel Methods in Lubrication, Tribology Series*, volume 37. Elsevier, 2000.
- [26] S. Bair. Roelands' missing data. *Proceedings of the Institution of Mechanical Engineers, Part J: Journal of Engineering Tribology*, (218):57–60, 2004.
- [27] M. H. Cohen and D. Turnbull. Molecular Transport in Liquids and Glasses. *The Journal of Chemical Physics*, 31(5):1164–1169, 1959.
- [28] A. K. Doolittle. Studies in Newtonian Flow. II. The Dependence of the Viscosity of Liquids on FreeSpace. *The Journal of Applied Physics*, 22(12):1471–1475, 1959.
- [29] S. Bair, J. Jarzynski, and W. O. Winer. The temperature, pressure and time dependence of lubricant viscosity. *Tribology International*, 34:461–468, 2001.
- [30] S. Yasutomi, S. Bair, and W. O. Winer. An application of a free volume model to lubricant rheology. *ASME Journal of Tribology*, 106(2):291–303, 1984.
- [31] R. R. Nelson, W. Webb, and J. A. Dixon. First-Order Phase Transitions of Six Normal Paraffins at Elevated Pressures. *The Journal of Chemical Physics*, 33(6):1756–1764, 1960.

- [32] U. Domańska and P. Morawski. Solid + liquid equilibria of (n-alkane + cyclohexane) mixtures at high pressures. *Fluid Phase Equilibria*, 218:57–68, 2004.
- [33] I. Yeh and G. Hummer. System-Size Dependence of Diffusion Coefficients and Viscosities from Molecular Dynamics Simulations with Periodic Boundary Conditions. *The Journal of Chemical Physics*, 108:15873–15879, 2004.
- [34] V. A. Levashov, J. R. Morris, and T. Egami. Viscosity, Shear Waves, and Atomic-Level Stress-Stress Correlations. *Physical Review Letters*, 106:115703, 2011.
- [35] M. Mondello and G. S. Grest. Viscosity calculations of n -alkanes by equilibrium molecular dynamics. *The Journal of Chemical Physics*, 106:9327–9335, 1997.
- [36] G. Pan and C. McCabe. Prediction of viscosity for molecular fluids at experimentally accessible shear rates using the transient time correlation function formalism. *The Journal of Chemical Physics*, 125:194527, 2006.
- [37] H. Tseng, J. Wu, and R. Chang. Shear thinning and shear dilatancy of liquid n-hexadecane via equilibrium and nonequilibrium molecular dynamics simulations: Temperature, pressure, and density effects. *The Journal of Chemical Physics*, 129:014502, 2008.
- [38] W. J. Jorgensen and J. Tirado-Rives. The OPLS Potential Functions for Proteins. Energy Minimizations for Crystals of Cyclic Peptides and Crambin. *Journal of the American Chemical Society*, 110(6):1657–1666, 1988.
- [39] W. J. Jorgensen, D. S. Maxwell, and J. Tirado-Rives. Development and Testing of the OPLS All-Atom Force Field on Conformational Energetics and Properties of Organic Liquids. *Journal of the American Chemical Society*, 118(45):11225–11236, 1996.
- [40] M. Mondello, G. S. Grest, A. R. Garcia, and B. G. Silbernagel. Molecular dynamics of linear and branched alkanes: Simulations and nuclear magnetic resonance results. *The Journal of Chemical Physics*, 105:5208–5215, 1996.
- [41] S. W. I. Siu, K. Pluhackova, and R. A. Böckmann. Optimization of the OPLS-AA Force Field for Long Hydrocarbons. *Journal of Chemical Theory and Computation*, 8:1459–1470, 2012.
- [42] H. Sun. COMPASS: An ab Initio Force-Field Optimized for Condensed-Phase Applications - Overview with Details on Alkane and Benzene Compounds. *The Journal of Physical Chemistry B*, 102:7338–7364, 1998.
- [43] R. W. Hockney and J. W. Eastwood. *Computer Simulation using Particles*. Taylor and Francis, 1989.
- [44] J. E. Basconi and M. R. Shirts. Effects of Temperature Control Algorithms on Transport Properties and Kinetics in Molecular Dynamics Simulations. *Journal of Chemical Theory and Computation*, 9:2887–2899, 2013.
- [45] E. Cancès, F. Legoll, and G. Stoltz. Theoretical and numerical comparison of some sampling methods for molecular dynamics. *ESAIM: Mathematical Modelling and Numerical Analysis*, 41(2):351–389, 2007.
- [46] S. T. Cui, P. T. Cummings, and H. D. Cochran. The calculation of the viscosity from the autocorrelation function using molecular and atomic stress tensors. *Molecular Physics*, 88(6):1657–1664, 1996.

- [47] J. H. Dymond, J. Robertson, and J. D. Isdale. Transport Properties of Nonelectrolyte Liquid Mixtures III. Viscosity Coefficients for n-Octane, n-Dodecane, and Equimolar Mixtures of n-Octane + n-Dodecane and n-Hexane + n-Dodecane from 25 to 100 C at Pressures up to 500 MPa or to the Freezing Pressure. *International Journal of Thermophysics*, 2(2):133–154, 1981.
- [48] J. H. Dymond, N. F. Glen, and J. D. Isdale. Transport Properties of Nonelectrolyte Liquid Mixtures VII. Viscosity Coefficients for Isooctane and for Equimolar Mixtures of Isooctane + n-Octane and Isooctane + n-Dodecane from 25 to 100 C at Pressures up to 500 MPa or to the Freezing Pressure. *International Journal of Thermophysics*, 6(3):233–250, 1985.
- [49] F. D. Rossini, K. S. Pitzer, R. L. Arnett, R. M. Braun, and G. C. Pimentel. Selected values of physical and thermodynamic properties of hydrocarbons and related compounds. *Carnegie Press, Pittsburgh*, 1953.
- [50] F. D. Rossini, K. S. Pitzer, W. J. Taylor, J. P. Ebert, J. E. Kilpatrick, C. W. Beckett, M. G. Williams, and H. G. Werner. Selected values of properties of hydrocarbons. *NBS Circular*, 461, 1947.
- [51] G. W. Nederbragt and J. W. Boelhouwer. Viscosity data and relations of normal and iso-paraffins. *Physica*, 13:305–318, 1947.
- [52] U. G. Krahn and G. Luft. Viscosity of Several Liquid Hydrocarbons in the Temperature Range 298–453 K at Pressures up to 200 MPa. *Journal of Chemical Engineering Data*, 39:670–672, 1994.